

Carnegie Mellon University
MELLON COLLEGE OF SCIENCE

THESIS

SUBMITTED IN PARTIAL FULFILLMENT OF THE REQUIREMENTS
FOR THE DEGREE OF

DOCTOR OF PHILOSOPHY IN THE FIELD OF PHYSICS

TITLE: "Fully-Relativistic Full-Potential Multiple Scattering Theory: Method and Applications"

PRESENTED BY: Xianglin Liu

ACCEPTED BY THE DEPARTMENT OF PHYSICS

| | |
|-------------------------------|---------|
| <u>Yang Wang</u> | 9/14/17 |
| YANG WANG, CO CHAIR PROFESSOR | DATE |

| | |
|-----------------------------------|---------|
| <u>Michael Widom</u> | 9/13/17 |
| MICHAEL WIDOM, CO CHAIR PROFESSOR | DATE |

| | |
|---------------------------|---------|
| <u>Scott Dodelson</u> | 9/25/17 |
| SCOTT DODELSON, DEPT HEAD | DATE |

APPROVED BY THE COLLEGE COUNCIL

| | |
|-----------------------|---------|
| <u>Rebecca Doerge</u> | 9/27/17 |
| REBECCA DOERGE, DEAN | DATE |

Fully-Relativistic Full-Potential Multiple Scattering Theory: Method and Applications

by

Xianglin Liu

Submitted in partial fulfillment of the
requirements for the degree of
Doctor of Philosophy

at

Carnegie Mellon University
Department of Physics
Pittsburgh, Pennsylvania

Advised by Professor Yang Wang and Michael Widom

September 20, 2017

Abstract

Relativistic effects (spin-orbit coupling in particular), are the origin of a rich diversity of phenomena of great interest to technological applications, such as spin-Hall effect, chiral spin texture, Rashba effect, and magnetocrystalline anisotropy. Multiple scattering theory (MST), on the other hand, is a powerful first principles method that is particularly useful for the investigation of complex condensed matter systems, such as impurities, alloys, and nanostructures. In this thesis, combination of the two is achieved with a state of the art single-site solver that directly solves the full-potential Dirac equation, in which the relativistic effects and full potential effects are treated on an equal footing. Compared to previous implementations of the full-potential relativistic MST, the generalized variable phase (sine and cosine scattering matrices) approach used here has the feature that all couplings of the solutions are retained and the solutions are expressed in terms of the free-space solutions, with no matching procedure required.

A persistent problem in previous implementation of the full-potential MST is that the charge density calculated within a sizable fraction of the muffin-tin radius are numerically unstable. In this thesis we present a new scheme to carry out the energy integration of the Green function. By using an efficient pole-searching technique to identify zeros of the well-behaved Jost matrices, we demonstrated that this scheme is numerically stable and computationally efficient, with speed comparable to the conventional contour energy integration method, while free of the pathology problem of the charge density. As an application, this method is utilized to self-consistently calculate the bulk properties of polonium, which is challenging for a conventional real-energy scheme.

The last chapter of this thesis is devoted to the application of our method to study magnetic anisotropy. This is in light of the rapid progress in recent years on the technology of perpendicular magnetic anisotropy for magnetic tunnel junctions (MTJ). As a preliminary study, the magnetic anisotropy energy of a free-standing Fe monolayer is calculated and good agreement with other methods is obtained. This study lays foundation for future research on large scale simulation of magnetic multilayer systems.

Acknowledgments

First, I wish to thank my advisor Yang Wang, without whom this work would not have been possible. He is always patient with my questions, encouraging to my research endeavors, and happy to share his expertise on multiple scattering theory and high performance computing with me. I would like to thank my co-advisor Michael Widom for always being available to help me. Many thanks to Bob Swendsen for all the encouragement during the last five years. Thank you to Di Xiao for helping me to improve my presentation skills. I am thankful to Manfred Paulini for all the helps and for making my stay in the physics department a happy and fulfilling experience.

I would also like to thank my collaborators at Oak Ridge National Laboratory (ORNL). In particular, thank you to G. Malcolm Stocks for the two rewarding summers in ORNL, and for proofreading this thesis. Thank you to Markus Eisenbach for all the helpful discussions on relativistic MST.

I am grateful for the support from my friends, including Rulin Chen, Will McGinley, Jun Li, Mao-Sheng Liu, Menglei Sun, Sanxi Yao, and many more. Special thanks to my girlfriend Fanli Zhou for being supportive and sweet. Finally, to my mom and dad, thank you so much for supporting me, guiding me, encouraging me, and for everything.

This work was sponsored in part by the U.S. Department of Energy, Office of Science, Basic Energy Sciences, Materials Science and Technology Division. This research used the Extreme Science and Engineering Discovery Environment (XSEDE), which is supported by National Science Foundation grant number OCI-1053575. Specifically, it used the Bridges system, which is supported by NSF award number ACI-1445606, at the Pittsburgh Supercomputing Center (PSC). This research also used the resources of the Oak Ridge Leadership Computing Facility at the Oak Ridge National Laboratory, which is supported by the Office of Science of the U.S. Department of Energy.

To my parents and grandparents

Contents

| | | |
|----------|---|-----------|
| 1 | Introduction | 9 |
| 1.1 | First Principles Calculations | 9 |
| 1.2 | “More is Different” | 9 |
| 1.3 | Fully-Relativistic Full-Potential MST | 11 |
| 2 | Density Functional Theory | 13 |
| 2.1 | Introduction | 13 |
| 2.2 | Electrons in Solids | 14 |
| 2.3 | Kohn-Sham Equation | 16 |
| 2.4 | Relativistic DFT | 16 |
| 2.5 | LDA, GGA, and Beyond | 18 |
| 3 | Multiple Scattering Theory | 20 |
| 3.1 | Overview | 20 |
| 3.2 | Green Functions | 21 |
| 3.3 | Single-Site Scattering | 22 |
| 3.4 | Multiple-Site Scattering | 25 |
| 3.5 | KKR Method | 26 |
| 3.6 | LSMS Method | 27 |
| 4 | Relativistic Single-Site Green Function | 29 |
| 4.1 | Introduction | 29 |
| 4.2 | Theory | 30 |
| 4.3 | Krein’s Theorem | 35 |
| 4.4 | Single-Site DOS | 37 |
| 4.5 | Single-Site Charge Density | 39 |

| | | |
|----------|---|-----------|
| 4.6 | Conclusions | 40 |
| 5 | Relativistic MST: A Pathology-Free Scheme | 48 |
| 5.1 | Introduction | 48 |
| 5.2 | Methods | 50 |
| 5.3 | Pole-Searching Technique | 53 |
| 5.4 | Polonium | 57 |
| 5.5 | Noble Metals | 60 |
| 5.6 | Conclusions | 63 |
| 6 | Spin-Polarized Calculations and Magnetic Anisotropy | 66 |
| 6.1 | Application of MST in Magnetism | 66 |
| 6.2 | BCC Iron | 68 |
| 6.3 | Magnetic Anisotropy | 68 |
| 6.4 | First Principles Calculation of the MAE | 71 |
| 6.5 | Iron Monolayer | 72 |
| 6.6 | Conclusion and Outlook | 73 |
| A | Conventions and Units | 75 |
| B | Derivation of the Regular Solution $\psi(\mathbf{r})$ | 77 |
| C | Derivation of the Green Function | 80 |
| D | Solving the Dirac Equation in Muffin-Tin Potential | 84 |

List of Figures

| | | |
|-----|--|----|
| 4.1 | (Color online) Comparison of the DOS from Green's function method and the Krein's theorem method. The blue solid lines show the Krein DOS n_K . The dashed lines show $n_K^{\text{in}} + n_K^{\text{out}}$ calculated using the Green's function. Because of the good agreement the two lines actually overlap. | 37 |
| 4.2 | (Color online) Comparison of the relativistic and nonrelativistic single-site DOS of noble metals. The blue solid lines are the DOS calculated from the relativistic full potential Green's function method. The red dashed lines are the DOS calculated from the non-relativistic full potential Green's function method, which solves the Schrödinger's equation. Note that the first peak of Au is not completely shown because it's too sharp. | 42 |
| 4.3 | The partial Krein IDOS of d electrons of copper corresponding to non-relativistic muffin-tin (NRMT), non-relativistic full potential (NRFP), relativistic muffin-tin (RMT) and relativistic full potential (RFP) calculations. There are 10 d channels in total and the number of degeneracy is shown for each curve. | 43 |
| 4.4 | The partial IDOS of d electrons of silver and gold in relativistic full potential calculation. There are 10 d channels in total and the number of degeneracy is shown for each curve. | 44 |
| 4.5 | The Krein IDOS components of the d electrons of group V elements. There are 10 d channels in total and the number of degeneracy is shown for each curve. | 45 |

| | | |
|-----|--|----|
| 4.6 | (Color online) The $l, m = (0, 0)$ component of the valence-band charge density of tantalum calculated with relativistic (R) method, non-relativistic (NR) Green's function method that solves Schrödinger's equation, and relativistic method at non-relativistic limit (RNR). | 46 |
| 4.7 | (Color online) The $l, m = (4, 0)$ component of the valence-band charge density of copper. Comparison of $\rho_{4,0}$ and $\sqrt{14/5} \rho_{4,4}$ is made to test the cubic symmetry in our results. | 46 |
| 4.8 | (Color online) Comparison of the relativistic (R) and nonrelativistic (NR) charge density around the origin. The non-relativistic limit of our relativistic method (RNR) is also shown. | 47 |
| 5.1 | Energy integration of the Green function. The multiple scattering part G_m is integrated along the upper semi-circle contour, while the single-site part G_s is integrated on real axis. The shallow bound states are integrated with a tiny circle and the resonance states are integrated using weighted sampling technique. | 54 |
| 5.2 | (Color online) The relative error of the number of electrons calculated from the single-site Green function $G_s(E, \mathbf{r}, \mathbf{r}')$ for both Cu and Au. Energy points are either obtained using weighted sampling or uniform grid. 16, 32, 64, 128 and 256 energy points are used for each curve and the trapezoidal rule is adopted in energy integration. | 54 |
| 5.3 | (Color online) The spherical component of the charge density of polonium corresponding to the shallow bound states. Note that a $4\pi r^2$ factor has been included. The <i>red dashed</i> line corresponds to $6p_{1/2}$ electron and the <i>blue solid</i> line corresponds to $6s_{1/2}$ electron. | 60 |
| 5.4 | Comparison of the total DOS and the single-site DOS of polonium. To show the DOS, the energy is shifted a little up on the real axis, with imaginary part $\text{Im}(E)=0.001$ Ry. The <i>dashed</i> line is the single-site DOS and the <i>solid</i> line is the total DOS. The vertical line is the Fermi energy. The shallow bound states are not shown on the single-site DOS because they are essentially a set of Dirac δ functions. 125000 k-points are used to calculate the DOS. | 61 |

- 5.5 (Color online) The volume dependence of total energy plot of polonium. The *solid*, *dashed*, *dot-dashed* lines correspond to the fitted equation of state of simple cubic, BCC, and FCC structures and the shift of total energy $E_0 = -41342$ (Ry/atom). When solving the Dirac equations a total of 1,500 radial mesh points are used within the muffin-tin radius to ensure convergence of the single-site solutions. 62
- 5.6 (Color online) The total energy of Au calculated using different methods. Different energy shifts are made for each curve so that the lowest point of each line is always zero. In the *solid* line, the core, semicore, and valence electrons are calculated by solving the Dirac equations. In the *dashed* line, the nonrelativistic Schrödinger equations are used for all the electrons. In the *dot-dashed* line the Dirac equations are solved for valence electrons while the Schrödinger equations are solved for core and semi-core electrons. 63
- 5.7 (Color online) Comparison of the relativistic and nonrelativistic DOS of Cu, Ag, and Au. The *red dashed* lines are the nonrelativistic results and *blue solid* lines are the relativistic results. Note that shift of the energy by E_f has been applied, so zero on the x-axis corresponds to the Fermi energy. 65
- 6.1 The single-site DOS and total DOS of BCC Fe. Imaginary part of the energies in the Green function are taken as 0.001 Ry to show the DOS. The Fermi energy is marked by a vertical line. 69
- 6.2 The $l, m = (0, 0)$ and $l, m = (2, 0)$ components of the charge density and magnetization of BCC Fe. Calculations are made with relativistic MST. 70
- 6.3 Calculated MAE vs $\sin^2(\theta)$ for an Fe monolayer with $a=4.83$ a.u.. The dots are the calculated values and the straight line is the fitted $-0.005 + 0.282x$ curve. 73
- D.1 *nonzero matrix elements of $f_{\Lambda'\Lambda'}$ and $g_{\Lambda'\Lambda'}$ for $l \leq 2$. The blue ones are the diagonal elements, including contributions from $l'' = l'$, $l'' = l' \pm 1$ and $l'' = l' \pm 2$. The green ones only have contribution from $l'' = l' + 1$ and the yellow ones only have $l'' = l' + 2$ element* 88

List of Tables

| | | |
|-----|--|----|
| 5.1 | The poles of the single-site Green function of Po | 59 |
| 5.2 | Comparison of the lattice constant (a) and bulk modulus (B_0) calculated with the experimental and theoretical data in the literature. | 60 |
| 5.3 | Comparison of calculated lattice constants and bulk moduli of noble metals with the experimental values. The LDA is employed in all calculations. Fully relativistic schemes are used except for the last two columns. In column Au _{NR} all electrons are calculated with nonrelativistic schemes, and relativistic schemes are utilized only for valence electrons in column Au _{R-Core} | 61 |
| 6.1 | The MAE (meV/atom) of Fe monolayer calculated with different methods. Lattice constant $a=4.83$ in all cases. | 72 |

Chapter 1

Introduction

1.1 First Principles Calculations

Materials are of fundamental importance to human beings, as vividly demonstrated by the naming of the stages of human civilization, from the stone, bronze, to iron ages. Nowadays we are in the digital age, and most electronic devices work by the storage, manipulation, and transport of electron charges in semiconductors, mostly silicon. For the development of next generation electronics, particularly the so called “spintronics” [1], it is inevitable to work with materials at the nano-scale. Such small systems are inherently governed by quantum mechanics and involve interactions of many particles. To understand them from a theoretical point of view, simple models are usually not enough, and calculations from first principles are necessary. The basic idea of first principles methods is to calculate the physical properties of materials with no input of empirical parameters. This is achieved by studying the underlying quantum physics of the system. Since all materials are made up of atoms, applications of first principles calculations are very general compared to model methods built with empirical parameters.

1.2 “More is Different”

From the point of view of elementary particles, among the four fundamental interactions of nature, the electromagnetic force is essentially the only one responsible for the physical and chemical properties of a material. In some sense, this is lucky for

condensed matter physicists because the coupling constant for electromagnetic force is small, approximately $1/137$, which means a perturbation technique can be applied to calculate the properties of a single electron to very high accuracy. For example, by employing quantum electrodynamics (QED), the magnetic moment of electron calculated agrees with experimental value to more than 10 significant digits [2]. For first principles calculations, there is no need for such a high accuracy and most of the time solving the Schrödinger or Dirac equation is good enough.

Although the underlying physics of electron interaction is well understood, direct use of this knowledge to carry out calculations is still a formidable task. Most of the difficulties originate from the large number of electrons in a material. To get around this problem, some reasonable approximations must be used to make first principles calculations practical while still free of empirical parameters. The first one is the Born-Oppenheimer approximation, which decouples the degree of freedom of electrons from that of the nuclei because the masses of electron and nucleus are different by a few orders of magnitude. The second approximation is in solving the many-body problem. In the Hartree-Fock method the many-body wave function is approximated by a determinant of one-particle orbitals. In density functional theory the exact exchange-correlation functional is replaced by approximations such as the local-density approximation (LDA) [3, 4] or generalized gradient approximation (GGA) [5].

Giving up part of the fundamentality of the theory is disturbing at first sight, especially for a method named with “first principles”, but this compromise turns out to be worthwhile, as demonstrated by the success and popularity of first principle calculations. As pointed out by P. W. Anderson in the 1970s, the idea of reducing everything to the fundamental laws is simply impractical as the system size increases, therefore “more is different” [6], and the important thing is to make good approximations that retain the physics of interest. For particle physics, the Standard Model is complete with the discovery of Higgs boson, but in the field of condensed matter physics, there are still a rich diversity of phenomena to explore. It is interesting to note that, elementary excitations with names originated from particle physics, such Majorana fermion [7], Wyle fermion [8], and skyrmion [9], are in the forefront of today’s condensed matter physics research.

1.3 Fully-Relativistic Full-Potential MST

A central step to determine the electronic structure of materials is to solve the Schrödinger equations. Various methods exist, such as plane-waves, tight-binding, and augmented plane waves. Most of these methods make use of the Bloch theorem and are mainly used for crystals. For multiple scattering theory (MST), however, the Bloch theorem is not necessary, therefore other than crystals, it can also be used to treat non-periodic systems. Another feature of MST is that, instead of solving the eigenvalue problems, it directly calculates the Green function of the system. With the Green function available, a lot of numerical techniques can then be devised. For example, energy integration of the Green function can be carried out on the complex plane, which greatly enhances the numerical efficiency.

The originally formulated MST solves the Schrödinger equation with the muffin-tin (MT) potential approximation, where the potential is assumed to be spherically symmetric within the muffin-tin spheres and constant in the interstitial region [10,11]. While the muffin-tin approximation generally works well for systems dominated by metallic bonding, it cannot properly describe a wide range of systems where the asymmetries of the effective potential [12] play an important role, such as surfaces, two-dimensional materials, and systems with directional covalent bonding. In addition, because the Schrödinger equation is nonrelativistic, it cannot properly describe systems where relativistic effects are important. In particular, it doesn't account for the spin-orbit coupling (SOC), a subject currently of great interest due to its role in many technologically important phenomena, such as magnetocrystalline anisotropy [13], Rashba effect [14], and magnetic Skyrmions [9]. To take into account the relativistic effects, a common practice is to treat the relativistic kinematic effects with the scalar-relativistic approximation [15], and include the SOC in a perturbative second-variational way. However, this strategy is problematic for heavy elements where SOC is not small compared to full-potential effects. To take into account both relativity and the full shape dependence of the crystal potential on an equal footing, the original MST formulation must be extended to a full-potential, Dirac equation, based theory, and indeed there are previous works in this regard by a number of groups [16–21]. A persistent problem in previous implementations of the full-potential MST is that the charge density calculated within a sizable fraction of the muffin-tin radius has pathological behavior that originates from the coupling of the matrix elements by full potential and the use of irregular solutions.

Because of the difficulties associated with the full-potential implementation, the MST method is primarily applied to close-packed metals [22].

In this work, we derived and implemented a different scheme, i.e., the sine and cosine scattering matrices formalism, to directly solve the full-potential Dirac equation. The solutions obtained are then used to construct the Green function of the whole system, from which physical observables are calculated. Rigorous test of this method is made by comparing the single-site density of states calculated from integration of the Green function with the one obtained from Krein's theorem. Using the code developed, we also carried out self-consistent calculations to investigate the crystal structure of Polonium and the relativistic effects in noble metal. The pathology around the origin is completely eliminated by carrying out the energy integration of the single-site Green function on real axis. By using an efficient pole-searching technique to identify zeros of the well-behaved Jost matrices, we demonstrated that this scheme is numerically stable and computationally efficient, with speed comparable to the conventional contour energy integration method, while free of the pathology problem of the charge density. Finally, as a further application of our method, we calculated the DOS of bulk Fe and the magnetocrystalline anisotropy of a single layer of iron atoms, both as a test of our code for magnetic system and a preliminary study of the multilayered system widely used in memory devices.

This thesis is structured as follows. In chapter 2 and chapter 3, the density functional theory and the multiple scattering method are introduced respectively. Chapter 4 is based on reference [23], in which details of our approach to solve the full-potential Dirac equation are presented. Comparison of the DOS calculated from two different methods are made, with excellent agreement demonstrated. Chapter 5 is based on reference [24], and is devoted to the self-consistent implementation of the MST method, in which the pole-searching algorithm and the pathology-free energy integration scheme is explained. Applications of our method to magnetic materials and the calculation of the magnetic anisotropy energy, are presented in the last chapter.

Chapter 2

Density Functional Theory

2.1 Introduction

Density functional theory (DFT) is a first principles calculation method widely used in a broad range of condensed matter systems [25]. The central idea of DFT is to use the electron density as the basic variable instead of the electron wave functions, and convert the complicated problem of interacting electrons into a much simpler problem of free electrons moving in an auxiliary effective potential. In principle, DFT is an exact theory for ground state, in practice, however, approximations are needed for the exchange-correlation functionals because the exact expressions are unknown for most systems. By adopting simple approximations such as local density approximation (LDA), DFT methods can reach satisfactory accuracy with high efficiency for systems ranging from metals, semiconductors, to insulators. Nowadays DFT has developed into an indispensable tool in both academic and industrial research of materials, and its fundamental role in condensed matter physics is compared to the standard model in particle physics [26].

DFT was formulated by Hohenberg, Kohn and Sham in the 1960s [3, 27]. Because of the importance of this method in the field of quantum chemistry, Walter Kohn was awarded the Noble Prize in chemistry in 1998, along with John Pople, who is famous for the development of the computational chemistry package Gaussian. Actually both Walter Kohn and John Pople worked in Carnegie Mellon University, with Professor Kohn in the Department of Physics from 1950 to 1960, and Professor Pople in the Department of Chemistry from 1964 to 1993.

In this chapter I will first give a brief description of the density functional method

in the framework of non-relativistic theory. The Kohn-Sham theorem and Kohn-Sham equations will be presented without detailed derivations and proofs, which can be found in the book by Paul Strange [28] and an introductory overview by U. von Barth [29]. After that the relativistic DFT will be presented and topics such as 4-current DFT and spin-polarized DFT will be discussed. Finally, limitations of LDA will be discussed and beyond-LDA methods will be surveyed to give a general picture of DFT methods.

2.2 Electrons in Solids

One major obstacle for the *ab-initio* study of solid system is the huge numbers of particles (electrons and nuclei) to be considered. For a practical electronic structure calculation, some reasonable approximations must be made. The first one is the Born-Oppenheimer approximation, which separates the motion of the nuclei from that of the electrons, with the observation that in a solid, electrons move much faster than the atomic nuclei. For non-relativistic calculations, the Hamiltonian of the electrons can then be written as

$$H = \sum_i^n \frac{\hat{\mathbf{p}}_i^2}{2m} - \sum_i^n \sum_j^N \frac{1}{4\pi\epsilon_0} \frac{Z_j e^2}{|\mathbf{r}_i - \mathbf{R}_j|} + \sum_{i<j}^n \frac{1}{4\pi\epsilon_0} \frac{e^2}{|\mathbf{r}_i - \mathbf{r}_j|}, \quad (2.1)$$

where n refers to the number of electrons and N to the number of atomic nuclei; \mathbf{R} indicates the position of the nucleus; Z is the atomic number; ϵ_0 signifies vacuum permittivity; \mathbf{r} , \mathbf{p} , m and e are the electron's position, momentum, mass, and electric charge, respectively. The first term in Eq. (2.1) represents the kinetic energy of the electrons; the second one represents the Coulomb attraction between the electrons and the nuclei; The third term represents the Coulomb repulsion between the electrons.

Even with the use of the Born-Oppenheimer approximation, it is still impractical to solve for the electron wave functions of the Hamiltonian in Eq. (2.1) because of the large number of degrees of freedom coupled together by the electron-electron interaction term. One method to simplify the problem is to replace this electron-electron interaction with a mean field interaction due to all the other electrons. This term is known as the Hartree energy and can be written out explicitly as

$$\frac{e^2}{2} \int \frac{1}{4\pi\epsilon_0} \frac{n(\mathbf{r})n(\mathbf{r}')}{|\mathbf{r} - \mathbf{r}'|} d\mathbf{r}d\mathbf{r}', \quad (2.2)$$

where $n(\mathbf{r})$ is the electron density. This approximation alone, however, turns out to be too crude for most applications because it ignores the exchange and correlation effects. As a further step to include the exchange energy, in the Hartree-Fock method, a single Slater determinant of one-electron orbitals is used to approximate the many-electron wave function, while retaining the antisymmetry of the electron wave function. As a result, other than the Hartree term in equation (2.2), an exchange term is also introduced. The Hartree-Fock method is widely used in the calculation of atoms and small molecules. However, because evaluation of the exchange term involves overlap integrals, the Hartree-Fock method does not have a good computational scalability and is less popular for large systems and solids. One major advantage of the Hartree-Fock method is that electron exchange is fully incorporated, while a major limitation is that correlation effects are completely ignored for electrons with opposite spin.

Compared to the Hartree-Fock method, DFT method incorporates both electron exchange and correlation (although both two effects are treated approximately in practice). By adopting simple schemes of exchange-correlation functional, such as LDA and GGA, DFT is already reliable and cost effective to calculate the ground state properties of a wide range of solid state systems. The central idea of DFT is the two Hohenberg-Kohn theorems [27]. The first one states that for a system of interacting electrons, the external potential (hence the total ground state energy) is a unique functional of the electron density. The second one states that the ground state correspond to a given external potential can be obtained by finding the density minimizing the total energy functional. Based on the two theorems, the Kohn-Sham equation can be derived, and I will write it down without giving proof in the next section.

Another important tool to study electrons in a solid is quantum field theory (QFT). In QFT the Hamiltonian is constructed with field operators that act on Fock space. QFT is a powerful theoretical framework to treat many-electron systems, but seldom used to directly calculate real materials because the corresponding Fock space (or the many-body wave function) is generally unknown. However, QFT can be used to treat simple model systems, such as homogeneous electron gas (HEG). This is particularly important for DFT since many successful exchange-correlation functionals in LDA are derived from HEG. Another application of QFT in condensed matter is the so called “effective field theory”, which studies the effective Lagrangian of the quasiparticles at the energy scale of interest. QFT is beyond the scope of this thesis, and for an interesting introduction to QFT, one is referred to the book by A. Zee [30].

2.3 Kohn-Sham Equation

By applying the Hohenberg–Kohn theorems, it can be shown (for example, see [28]) that the complicated problem of solving the Schrödinger equation of N -interacting electrons can be reduced to solving an auxiliary system of independent electrons moving in an effective potential $V_{\text{eff}}(\mathbf{r})$. The wave functions $\psi(E, \mathbf{r})$ obey the celebrated Kohn-Sham equation

$$\left(-\frac{\hbar^2}{2m}\nabla^2 + V_{\text{eff}}(\mathbf{r})\right)\psi(E, \mathbf{r}) = E\psi(E, \mathbf{r}), \quad (2.3)$$

where

$$V_{\text{eff}}(\mathbf{r}) = V_{\text{ext}}(\mathbf{r}) + \frac{e^2}{4\pi\epsilon_0} \int d\mathbf{r}' \frac{n(\mathbf{r}')}{|\mathbf{r} - \mathbf{r}'|} + \frac{\delta E_{xc}}{\delta n(\mathbf{r})}. \quad (2.4)$$

The first term above, $V_{\text{ext}}(\mathbf{r})$, corresponds to external electric potential. The second term arises from the Hartree energy in equation (2.2), which describes the mean-field contribution of the Coulomb repulsion between the electrons. The last term contains the many-body effects, which are not included by the first two terms, and E_{xc} is defined as the exchange-correlation functional. To initiate the calculation, a starting potential is put into the Kohn-Sham equation, from which the charge density and the new effective potential can then be obtained. The calculation continues self-consistently until convergence is reached. With the converged charge density available, the total energy of the ground state E_g can be obtained with [28]

$$E_g = \sum_{i=1}^N E_i - \frac{1}{2} \frac{e^2}{4\pi\epsilon_0} \int \int d\mathbf{r} d\mathbf{r}' \frac{n(\mathbf{r})n(\mathbf{r}')}{|\mathbf{r} - \mathbf{r}'|} - \int d\mathbf{r} \frac{\delta E_{xc}}{\delta n(\mathbf{r})} n(\mathbf{r}) + E_{xc}, \quad (2.5)$$

and other physical observables can be extracted.

2.4 Relativistic DFT

The above formalism can be generalized to relativistic system straightforwardly. Instead of the Schrödinger equation, the Dirac Kohn-Sham equations need to be solved

$$\{c\boldsymbol{\alpha}(\hat{\mathbf{p}} - e\mathbf{A}_{\text{eff}}(\mathbf{r})) + \beta mc^2 + V_{\text{eff}}(\mathbf{r})\}\psi(E, \mathbf{r}) = W\psi(E, \mathbf{r}), \quad (2.6)$$

where c is the speed of light, $\psi(E, \mathbf{r})$ are four component Dirac spinors and $\boldsymbol{\alpha}$, β are the Dirac matrices defined as

$$\alpha_i = \begin{pmatrix} 0 & \sigma_i \\ \sigma_i & 0 \end{pmatrix}, \quad \beta = \begin{pmatrix} I_2 & 0 \\ 0 & -I_2 \end{pmatrix}, \quad (2.7)$$

with $i = x, y, z$, σ_i are the usual Pauli matrices, and I_2 is the two dimensional identity matrix. W and E are the relativistic energy and relativistic kinetic energy, respectively. W and E are related to momentum p by

$$W = \sqrt{m^2c^4 + p^2c^2}, \quad (2.8)$$

$$E = W - mc^2. \quad (2.9)$$

Comparing equation 2.6 with equation 2.3, a major difference is that other than the effective electric potential, there is another term that corresponds to the effective vector potential, which is given by

$$\mathbf{A}_{\text{eff}}(\mathbf{r}) = \mathbf{A}_{\text{ext}}(\mathbf{r}) + \frac{e^2}{4\pi\epsilon_0c^2} \int d\mathbf{r}' \frac{\mathbf{J}(\mathbf{r}')}{|\mathbf{r} - \mathbf{r}'|} + \frac{\delta E_{\text{xc}}}{\delta \mathbf{J}(\mathbf{r})}. \quad (2.10)$$

The above formalism is called four current DFT. While the four current DFT provides an excellent framework to describe both spin and orbital magnetic moments, it is rarely used in practice because it is difficult to express the exchange-correlation functionals in terms of the local four currents $[n(\mathbf{r}), \mathbf{J}(\mathbf{r})]$. One widely used approximation to the four current theory is to replace the vector potential $\mathbf{A}(\mathbf{r})$ with the magnetization density $\mathbf{m}(\mathbf{r})$. This is achieved by applying the Gordon decomposition to the currents and discarding the terms corresponding to the diamagnetic effects [28], which are usually very small due to quenching of orbital moments by the crystal field. The resulting Dirac Kohn-Sham equations are

$$\{c\boldsymbol{\alpha}\hat{\mathbf{p}} + \beta mc^2 + V_{\text{eff}}(\mathbf{r}) - \mathbf{m}(\mathbf{r}) \cdot \mathbf{B}_{\text{eff}}(\mathbf{r})\}\psi(E, \mathbf{r}) = W\psi(E, \mathbf{r}), \quad (2.11)$$

where

$$\mathbf{B}_{\text{eff}}(\mathbf{r}) = \mathbf{B}_{\text{ext}}(\mathbf{r}) + \frac{\delta E_{\text{xc}}}{\delta \mathbf{m}(\mathbf{r})}. \quad (2.12)$$

2.5 LDA, GGA, and Beyond

The exchange-correlation (XC) functional E_{xc} plays a crucial role in DFT. In the widely used local density approximation (LDA), the XC-functional only depends on the local density of the electrons. Since LDA is derived from homogeneous electron gas, it seems that it should only be valid for systems with slowly varying electron densities, and fail for rapidly changing densities. However, it turns that LDA gives a reasonable description of a wide range of systems, most of which do have rapidly varying densities. One reason for the robustness of LDA is that it satisfies the sum rule of the exchange-correlation hole [4]. Despite the success of LDA, because XC-functional is intrinsically non-local, it comes as no surprise that LDA falls down in some cases. For example, electrons should not interact with themselves, so in principle the self-interactions in equation 2.2 should be completely canceled out by the XC-functional, but this is not true for LDA, where a small portion of the spurious self-interaction still exists. Another problem is that, although LDA is a good description of delocalized electrons, it can not properly describe correlations between the localized electrons. For example, LDA tends to overbind the system, which gives rise to unrealistic metallic ground states for some insulators.

To better describe the spatial variation of the electron density, the generalized gradient approximation (GGA) is widely used. In this approximation the XC-functional not only depends on the local density, but also depends on the gradient. By using GGA, the lattice constants calculated are generally in better agreement with experimental data. Following similar strategy, more complicated form of EX-functionals such as “meta-GGA” and “hyper-GGA” are also developed, as described by the so called “Jacob’s ladder” [31]. These more complicated XC functionals can describe intermolecular forces such as hydrogen and van der Waals bonds, but implementation of such functionals are usually more difficult because of their dependence on electron orbitals. For solid systems, LDA and GGA are still the most popular ones.

A different strategy to improve LDA is to remove the spurious self-interaction. For example, in the self-interaction correction (SIC) [4] scheme, this is done by directly deducting the self-interaction energy of each atomic orbital from the XC-functional. SIC is mainly used for the calculation of strongly correlated systems, such as transition metal oxides and rare earth elements. A less aggressive method to correct the self-interaction is to include part of the exact exchange energy into the so called hybrid

functionals [32], which are widely used in the field of quantum chemistry.

Finally, another way to go beyond LDA is to improve the description of the correlations of the localized electrons. Most of these methods are based on the Hubbard model. For example, in LDA+U, a “Hubbard U” parameter is introduced to describe the Coulomb repulsion between the localized electronic states. In practice, values of the U parameters can be calculated from first principles, input from experimental data, or simply taken as adjustable parameters. In LDA+U only the static electron correlation effects are taken into consideration. As one step further, in dynamical mean field theory (DMFT), the dynamical correlation effects are included as well. This is achieved by converting the many-body lattice problem into a local impurity problem, and then solving this impurity problem with various approximation schemes. LDA+U and DMFT are important tools to treat strongly correlated materials, but are beyond the scope of this work and LDA is used in all our calculations.

Chapter 3

Multiple Scattering Theory

3.1 Overview

Multiple-scattering theory (MST) underpins a number of widely used methods for solving the electronic structure problem in solids, all of which have their origins in the KKR method originally introduced by Korringa [10] in 1947 and independently re-derived by Kohn and Rostoker [11] in 1953. Three features of MST distinguish it from conventional basis set methods. Firstly, it naturally yields a separation between the single-site potential scattering and structural arrangement (positions) of the individual scatterers. Secondly, in the framework of density functional theory (DFT), it provides an explicit expression for the Green function of the system, which can then be used to calculate the charge and spin densities without explicit calculation of the wave functions. Finally, MST does not rely on the Rayleigh–Ritz variational method, which is crucial for other band theory methods.

The availability of the Green function makes MST a versatile tool to investigate more complex systems other than perfect crystals. For example, by applying the Dyson’s series expansion to the Green function, defects and impurities in an otherwise perfect crystal can be investigated [33]. Another example is the KKR-CPA method, which is based on a combination of MST with the coherent potential approximation (CPA) [34–36]. KKR-CPA is widely used to calculate the configurationally averaged properties of disordered systems, such as random alloys [37, 38] and the disordered local moment state of metallic magnets [39]. A more recent development is in studying of strongly correlated systems, where the MST Green function can be readily used in conjunction with the GW approximation [40] or the dynamical mean field theory (DMFT) [41].

Moreover, the real space formulation of MST [42] has demonstrated essentially ideal linear scalability on current supercomputing architecture [43], and, as a result, can be employed to study solid state systems with tens of thousands of atoms.

The first half of this chapter is meant to provide a brief introduction to MST. Important concepts such as Green functions, single-site scattering, and multiple scattering will be explained following a similar manner as in the textbook [28] by Paul Strange. In the second half of this chapter, two different MST methods, the KKR method and LSMS method, will be quickly introduced. For the sake of simplicity, the discussions in this chapter are limited to the nonrelativistic case, so only the Schrödinger equation needs to be solved.

3.2 Green Functions

A central quantity in MST is the Green function, from which all physical quantities needed in self-consistent calculations are obtained. The formal definition of the Green function $G(\mathbf{r}, \mathbf{r}', E)$ is

$$(E - \hat{H}(\mathbf{r}))G(\mathbf{r}, \mathbf{r}', E) = \delta(\mathbf{r} - \mathbf{r}'), \quad (3.1)$$

where $\hat{H}(\mathbf{r})$ is the Hamiltonian in real space, E is the kinetic energy and $\delta(\mathbf{r} - \mathbf{r}')$ is the Dirac delta function. Using the normalization condition of orthonormal basis

$$\sum_n \psi_n^\dagger(\mathbf{r})\psi_n(\mathbf{r}') = \delta(\mathbf{r} - \mathbf{r}'), \quad (3.2)$$

it is easy to obtain the spectral representation of the Green function

$$G(\mathbf{r}, \mathbf{r}', E) = \sum_n \frac{\psi_n(\mathbf{r})\psi_n^\dagger(\mathbf{r}')}{E - E_n}. \quad (3.3)$$

Equation (3.3) provides a method to construct the Green function using eigenvalues and eigenfunctions of the Hamiltonian. In wave function based methods such as linear muffin-tin orbital (LMTO) method, this is indeed how the Green function is calculated. For MST, however, equation (3.3) is not very helpful because the philosophy of MST is to obtain Green functions without directly solving the eigenvalue problem. Instead of equation (3.3), in MST the Green function is obtained from Dyson's equations with free

electrons used as the reference system. The free-electron Green function $G_0(\mathbf{r}, \mathbf{r}', E)$ is given by

$$G_0(\mathbf{r}, \mathbf{r}', E) = -\frac{e^{ip|\mathbf{r}-\mathbf{r}'|}}{4\pi|\mathbf{r}-\mathbf{r}'|}. \quad (3.4)$$

Since in MST the scattering problem will be solved by partial wave expansion, it is convenient to write down the angular momentum expansion of the free particle Green function

$$G_0(\mathbf{r}, \mathbf{r}', E) = -ip \sum_L h_l(pr_>) j_l(pr_<) Y_L(\hat{\mathbf{r}}) Y_L^*(\hat{\mathbf{r}}'), \quad (3.5)$$

where $r_< = \min(r, r')$ and $r_> = \max(r, r')$. L is the angular momentum index representing (l, m) . $j_l(r)$ and $h_l(r)$ are the spherical Bessel functions and spherical Hankel functions of the first kind. $Y_L(\hat{\mathbf{r}})$ are the spherical harmonics. Using the short-hand notation that

$$J_L(\mathbf{r}) = j_l(pr) Y_L(\hat{\mathbf{r}}), \quad (3.6)$$

$$H_L^+(\mathbf{r}) = h_l(pr) Y^*(\hat{\mathbf{r}}), \quad (3.7)$$

the free-space Green function can be written as

$$G_0(\mathbf{r}, \mathbf{r}', E) = -ip \sum_L J_L(\mathbf{r}_<) H_L^+(\mathbf{r}_>). \quad (3.8)$$

Note that the “+” superscript signifies the left-hand solutions. The relation between left-hand and right-hand solutions is simply Hermitian conjugate for real energies, but can be subtle for solutions of a general potential (see appendix C).

3.3 Single-Site Scattering

Before considering the scattering of electrons with the effective potential of the whole system, it is useful to study the single-site scattering problem. In MST the whole space is divided into non-overlapping polyhedrons Ω_i (Wigner–Seitz cell, for example). The single-site potentials $V_i(\mathbf{r})$ are obtained by retaining the potential inside Ω_i while setting

the potential outside as zero, i.e.,

$$V_i(\mathbf{r}) = \begin{cases} V(\mathbf{r}) & \mathbf{r} \in \Omega_i, \\ 0 & \mathbf{r} \notin \Omega_i, \end{cases} \quad (3.9)$$

therefore the total potential $V(\mathbf{r})$ can be written as sum of the space filling potentials $V_i(\mathbf{r})$ as

$$V(\mathbf{r}) = \sum_i V_i(\mathbf{r}). \quad (3.10)$$

Now let's focus on the scattering of the electron with a single potential $V_i(\mathbf{r})$. Using Dyson equations, the single-site Green function $G_s(\mathbf{r}, \mathbf{r}', E)$ described by the Hamiltonian $\hat{H}_0(\mathbf{r}) + V_i(\mathbf{r})$ can be written in terms of the free-space Green function as

$$G_s(\mathbf{r}, \mathbf{r}', E) = G_0(\mathbf{r}, \mathbf{r}', E) + \int G_0(\mathbf{r}, \mathbf{r}'', E) V_i(\mathbf{r}'') G_s(\mathbf{r}'', \mathbf{r}', E) d\mathbf{r}''. \quad (3.11)$$

To solve the above integral equation, it is convenient to introduce the t -operator, as defined by

$$V_i(\mathbf{r}) G_s(\mathbf{r}, \mathbf{r}', E) = \int t(\mathbf{r}, \mathbf{r}'', E) G_0(\mathbf{r}'', \mathbf{r}', E) d\mathbf{r}''. \quad (3.12)$$

Substituting it into equation (3.11), we have

$$G_s(\mathbf{r}, \mathbf{r}', E) = G_0(\mathbf{r}, \mathbf{r}', E) + \iint G_0(\mathbf{r}, \mathbf{r}'', E) t(\mathbf{r}'', \mathbf{r}''', E) G_0(\mathbf{r}''', \mathbf{r}', E) d\mathbf{r}'' d\mathbf{r}'''. \quad (3.13)$$

Note that now all the scattering information from $V_i(\mathbf{r})$ has been absorbed into the t -operator. Plugging equation (3.8) into equation (3.13), for $\mathbf{r} < \mathbf{r}'$, we have

$$G_s(\mathbf{r}, \mathbf{r}', E) = -ip \sum_L J_L(\mathbf{r}) H_L^+(\mathbf{r}') - p^2 \sum_L \sum_{L'} H_L(\mathbf{r}) t_{LL'}(E) H_{L'}^+(\mathbf{r}'), \quad (3.14)$$

where $t_{LL'}(E)$ is the single-site t -matrix defined as

$$t_{LL'}(E) = \iint J_L^+(\mathbf{r}'') t(\mathbf{r}'', \mathbf{r}''', E) J_{L'}(\mathbf{r}''') d\mathbf{r}'' d\mathbf{r}'''. \quad (3.15)$$

The definition of the t -operator in equation (3.12) involves $G_s(\mathbf{r}, \mathbf{r}', E)$, which is to be determined, so we still do not know how to calculate $t_{LL'}(E)$. However, it can be shown [28] that $t_{LL'}(E)$ is related to the phase shift and S -matrix in scattering theory, which can be extracted from the regular solutions of the time-independent Schrödinger equation

$$[-\nabla^2 + V_i(\mathbf{r})] \psi(E, \mathbf{r}) = E\psi(E, \mathbf{r}). \quad (3.16)$$

Note that the solutions $\psi(E, \mathbf{r})$ do not need to be eigenfunction of the Schrödinger equation and E can take arbitrary values. This is quite different from other DFT methods. Another important thing to note is that, strictly speaking, equation (3.14) only holds true for $r, r' > r_{cs}$, where r_{cs} is radius of the circumscribed sphere. Inside the circumscribed sphere, the free-space solutions $J_L(\mathbf{r})$ and $H_L(\mathbf{r})$ should be matched smoothly by solutions of equation (3.16). Combining the above discussions, we see that in MST the single-site Green function can be calculated from solutions of the single-site Schrödinger equation. Note that these smoothly-matched solutions are all irregular solutions because they do not have a well-defined boundary conditions at the origin. For the benefit of numerical stability, the regular solutions are preferred in the expression of the Green function. The regular solutions can be introduced by using a different expression of the single-site Green function [44],

$$G_s(\mathbf{r}, \mathbf{r}', E) = \sum_L \sum_{L'} Z_L(\mathbf{r}) t_{LL'}(E) Z_{L'}^+(\mathbf{r}') - \sum_L Z_L(\mathbf{r}) \mathcal{J}_L^+(\mathbf{r}'), \quad (3.17)$$

where $Z_L(\mathbf{r})$ are the regular solutions given by

$$Z_L(\mathbf{r}) = \sum_{L'} (t_{LL'}(E))^{-1} \mathcal{J}_{L'}(\mathbf{r}) - ip\mathcal{H}_L(\mathbf{r}), \quad (3.18)$$

and $\mathcal{J}_L(\mathbf{r})$ and $\mathcal{H}_L(\mathbf{r})$ are the irregular solutions smoothly matched to $J_L(\mathbf{r})$ outside the potential. To see that $Z_L(\mathbf{r})$ are indeed regular solutions, one can follow the derivations for the relativistic case in appendix C.

3.4 Multiple-Site Scattering

In analogy to the single-site t -operator, the multiple scattering T -operator can also be defined. Using Dyson equation, it is easy to show that the T -operator can be formally written as

$$T(E) = V + VG_0T(E). \quad (3.19)$$

The single-site t -operator also follows similar relation:

$$t^i(E) = V_i + V_iG_0t^i(E), \quad (3.20)$$

where the i index is used to signify different atomic sites. Combing the above two expressions with the fact that $V = \sum_i V_i$, it can be shown [28] that we have

$$T(E) = \sum_{ij} \tau^{ij}(E), \quad (3.21)$$

where

$$\tau^{ij}(E) = t^i(E)\delta^{ij} + \sum_{k \neq i} t^i(E)G_0(E)\tau^{kj}(E) \quad (3.22)$$

are the well-known scattering path operators that describe the propagation of the electron from site i to site j , along all possible paths in the system. The above discussions are made in a simple operator form, eventually all the operators need to be projected into the basis of spherical Bessel functions and spherical harmonics. Equation (3.22) can then be written out explicitly as

$$\tau_{LL'}^{ij}(E) = t_{LL'}^i(E)\delta^{ij} + \sum_{k \neq i} \sum_{L''L'''} t_{LL''}^i(E)G_{L''L'''}^0(\mathbf{R}_i - \mathbf{R}_j)\tau_{L''L'''}^{kj}(E), \quad (3.23)$$

where \mathbf{R}_i are position vectors of atomic nuclei and $G_{L''L'''}^0(\mathbf{R}_i - \mathbf{R}_j)$ are the so called structure constants. Note that the structure constants only have dependence on the crystal structure, and is a two-site free-space Green function that can be written out

explicitly as

$$G_{L''L'''}^0(\mathbf{R}_i - \mathbf{R}_j) = - (1 - \delta_{\mathbf{R}_i, \mathbf{R}_j}) 4i\pi p \sum_{L''} i^{l-l'-l''} C_{LL'}^{L''} h_{l''}(p|\mathbf{R}_i - \mathbf{R}_j| Y_{L''}(\hat{\mathbf{R}}_i - \hat{\mathbf{R}}_j)). \quad (3.24)$$

From equation (3.23), the τ -matrix can then be solved as

$$\tau_{LL'}^{ij}(E) = \left[[t_{LL'}^i(E) \delta^{ij}]^{-1} - G_{L''L'''}^0(\mathbf{R}_i - \mathbf{R}_j) \right]^{-1}. \quad (3.25)$$

The τ -matrix calculated above can then be used to construct the Green function of the whole system by using equation (3.21) and the multiple-scattering analogy of equation (3.13). It can be shown [44] that the following expression can be obtained

$$G(\mathbf{r}, \mathbf{r}', E) = \sum_L \sum_{L'} Z_L^i(\mathbf{r}_i) \tau_{LL'}^{ij}(E) Z_{L'}^{j+}(\mathbf{r}'_j) - \sum_L Z_L^i(\mathbf{r}_i) \mathcal{J}_L^{j+}(\mathbf{r}'_j) \delta^{ij}, \quad (3.26)$$

where $\mathbf{r}_i = \mathbf{r} - \mathbf{R}_i$. Note that in the above expression we imply that \mathbf{r} and \mathbf{r}' can be expanded at different cells, i.e., $i \neq j$, which is less common but actually valid as explained in reference [44]. Equation (3.26) is in close resemblance to the single-site Green function in equation (3.17), with the only major difference to be the replacement of the t -matrix by the τ -matrix.

3.5 KKR Method

For solid systems, the above scheme of solving the the Schrödinger equation at each atom is impractical because of the huge amounts of atoms involved. For crystals, however, periodicity of the effective potentials can be used to simplify the problem into solving the k -dependent Schrödinger equations within a representative unit cell, in which case working on k -space is usually more efficient. For MST, this method of calculating crystals is referred as the KKR method in our context, to distinguish it from the real space implementation of MST.

In the KKR method, to obtain the k -space expression of the τ -matrix and structure constants, the lattice Fourier transformations [28] are performed, and equation (3.25)

is converted into

$$\tau_{LL'}(\mathbf{q}, E) = [t_{LL'}^{-1}(E) - G_{LL'}(\mathbf{q}, E)]^{-1}. \quad (3.27)$$

Integrating $\tau_{LL'}(\mathbf{q}, E)$ in the first Brillouin zone, we obtain $\tau_{LL'}(E)$. The Green function in equation (3.26) becomes

$$G(\mathbf{r}, \mathbf{r}', E) = \sum_L \sum_{L'} Z_L^m(\mathbf{r}_m) \tau_{LL'}^{mn}(E) Z_{L'}^{n+}(\mathbf{r}'_n) - \sum_L Z_L^{m+}(\mathbf{r}_m) \mathcal{J}_L^n(\mathbf{r}'_n) \delta^{mn}. \quad (3.28)$$

The above expression looks almost identical to equation (3.26), but note that m, n here are the atom indices within the unit cell, instead of the atom indices of the whole system, which are signified by i, j . Another thing to note is that, the scattering path operator will be singular if

$$\det [t_{LL'}^{-1}(E) - G_{LL'}(\mathbf{q}, E)] = 0, \quad (3.29)$$

for some given values of \mathbf{q} and E . Because poles of the Green function correspond to the eigenvalues of the Schrödinger equation, the above scheme provides an approach to determine the band structure of crystals, as implemented in the linearized KKR [45] method.

3.6 LSMS Method

The KKR method is efficient to calculate crystals, but to treat non-periodic systems such as alloys, surfaces, and nanostructures, a large “supercell” is generally required, which introduces unreal effects due to the artificial periodic boundary conditions. Another disadvantage of KKR method (like most other band theory methods), is that even by using independent-particle approximation, the computational efforts will be proportional to N^3 as the number of atoms N increases, due to the need for matrix manipulations (equation (3.27), for example). As a result, the KKR method is typically only used to calculate systems with less than a few hundred atoms. To treat larger systems, Wang *et al.* [42] devised a real space implementation of MST called locally self-consistent multiple scattering (LSMS) method that scales linearly with N . As in most “order-N” method, this linear scaling is achieved by taking advantage of

the “nearsightedness” [46] of the system resulting from the destructive interference of the wave functions.

Implementation of the LSMS method is very similar to the common real space MST method, except that instead of considering scattering of electrons at all atomic sites, the scattering effects are restricted within the local interaction zone (LIZ) surrounding each atom (usually restricted to several neighboring shells). For each LIZ, the computational efforts scale as N_{LIZ}^3 , but since N_{LIZ} is a fixed number, the overall scaling is linear with respect to the total number of atoms N . One important consideration in LSMS is to determine the appropriate size of LIZ. Although “nearsightedness” is a very general principle, there is no universal guidance on choosing the size of LIZ, which depends on the element and the physical quantities of interest. For example, charge density generally converges faster than the density of states, and the total energy of elemental iron converges much more rapidly than that of molybdenum. Therefore in practice, convergence of the result with respect to N_{LIZ} has to be ensured before comparing it with experiment.

In most other DFT methods, the calculation is carried out in k -space. For quantities of local origin, k -space integration may not be the optimal approach and a real-space method could be more advantageous. One good example is the calculation of magnetocrystalline anisotropy energy (MAE) of BCC Fe. Because of the cubic symmetry, the MAE in BCC Fe is very small, with experimental value of $-1.4 \mu eV/\text{atom}$. In k -space methods, determining the energy with such a high accuracy requires special numerical methods such as the state tracking approach or the torque approach, and relatively large number of k -points [47]. By using the LSMS method, however, the MAE can be obtained quite easily [48, 49], with about 59 atoms in the LIZ.

Chapter 4

Relativistic Single-Site Green Function

4.1 Introduction

The multiple-scattering theory (MST) is a DFT based *ab-initio* method that is widely applied to the calculation of the electronic structure of metals, alloys and impurities. As demonstrated in the last chapter, a crucial step in MST calculation is to solve the single-site scattering problem. Combined with the position information of the atoms, solutions of the single-site scattering problem can be used to construct the Green's function of the whole system, from which most physical quantities can be extracted. Because of the essential role played by the single-site scattering in MST, there have been a constant effort to improve it in the last few decades [50]. The earliest MST solves the Schrödinger's equation and employs the muffin-tin potential approximation, i.e. the potential is spherically symmetric within a bounding sphere and is constant outside. Then the generalization to full potential (FP) [51] and relativistic cases [52–55], and eventually combination of the two, i.e. relativistic full potential (RFP), were proposed and implemented using various schemes [16–18, 56]. Among them one widely used RFP MST code is developed by Huhne *et al.* [19] to either solve the coupled integral equations iteratively using Born's series expansion or to directly solve the coupled differential equations. In a recent paper [20], the coupled differential equations are also solved by matching the regular solutions at the boundary of the Wigner–Seitz cell.

In this chapter we present an alternative formalism to tackle the RFP single-site

scattering problem by directly solving the Dirac differential equation. This method is a relativistic generalization of the non-relativistic FP MST method [57]. Compared to other RFP methods, this new formalism has the feature that the differential equation, the t matrix and the single-site Green's function are all expressed in terms of the r dependent sine and cosine matrices. We would like to point out that the sine and cosine scattering matrices technique to obtain the solutions for relativistic scattering theory was first proposed by X. D. Wang *et al.* [18], based on the variable phase technique [58,59], and later implemented by S. B. Kellen and A. J. Freeman [56]. The major difference between our method and the Kellen & Freeman's approach is in the calculation of observables. They find the observables by searching for energy eigenvalues and eigenfunctions of the KKR secular equation, while in our case all physical quantities are expressed in terms of the Green's functions, without the compute-intensive eigenvalue searching and the wave function orthonormalization procedures.

As a test of our code, the single-site DOS are calculated using both the Green's function method and Krein's theorem and the two results are compared. To investigate the relativistic effects and the full potential effects, we study the density of states of noble metals and group V elements. Finally, the charge density of tantalum is calculated and some interesting relativistic features are discussed.

4.2 Theory

Within the framework of spin polarized relativistic density functional theory [60], the effective potential is written as

$$V(\mathbf{r}) = \begin{pmatrix} v(\mathbf{r}) + \boldsymbol{\sigma} \cdot \mathbf{B}(\mathbf{r}) & 0 \\ 0 & v(\mathbf{r}) - \boldsymbol{\sigma} \cdot \mathbf{B}(\mathbf{r}) \end{pmatrix}, \quad (4.1)$$

where $\boldsymbol{\sigma}$ are the Pauli matrices and \mathbf{B} are effective magnetic fields. In the following discussion we will focus on nonmagnetic systems and discard the \mathbf{B} terms (see Appendix D for an example with magnetic field included). For $r > R_c$, where R_c is the radius of the circumscribed sphere of the Wigner-Seitz cell, the effective potential $V(\mathbf{r})$ vanishes, and the solutions of the corresponding free-space Dirac equation are well known. The

right-hand solutions are

$$J_{\Lambda}(E, \mathbf{r}) = \left(W/c^2 + \frac{1}{2} \right)^{1/2} \begin{pmatrix} j_l(pr) \chi_{\Lambda}(\hat{\mathbf{r}}) \\ \frac{ipcS_{\kappa}}{W+c^2/2} j_{\bar{l}}(pr) \chi_{\bar{\Lambda}}(\hat{\mathbf{r}}) \end{pmatrix}, \quad (4.2)$$

$$N_{\Lambda}(E, \mathbf{r}) = \left(W/c^2 + \frac{1}{2} \right)^{1/2} \begin{pmatrix} n_l(pr) \chi_{\Lambda}(\hat{\mathbf{r}}) \\ \frac{ipcS_{\kappa}}{W+c^2/2} n_{\bar{l}}(pr) \chi_{\bar{\Lambda}}(\hat{\mathbf{r}}) \end{pmatrix}, \quad (4.3)$$

where $j_l(pr)$ and $n_l(pr)$ are the usual spherical Bessel functions of the first kind and the second kind, with angular momentum index l . Λ stands for the pair of relativistic angular-momentum indices (κ, μ) and S_{κ} is the sign of κ index. $\bar{\Lambda} = (-\kappa, \mu)$ and

$$\bar{l} = \begin{cases} l+1 & \text{if } \kappa < 0 \\ l-1 & \text{if } \kappa > 0 \end{cases}. \quad (4.4)$$

χ_{Λ} and $\chi_{\bar{\Lambda}}$ are the spin-angular functions

$$\chi_{\Lambda}(\hat{\mathbf{r}}) = \sum_{m_s=\pm 1} C(l, j, \frac{1}{2}|\mu - m_s, m_s) Y_{l, \mu - m_s}(\hat{\mathbf{r}}) \phi_{m_s}, \quad (4.5)$$

$$\chi_{\bar{\Lambda}}(\hat{\mathbf{r}}) = \sum_{m_s=\pm 1} C(\bar{l}, j, \frac{1}{2}|\mu - m_s, m_s) Y_{\bar{l}, \mu - m_s}(\hat{\mathbf{r}}) \phi_{m_s}, \quad (4.6)$$

where $C(l, j, \frac{1}{2}|\mu - m_s, m_s)$ are the Clebsch-Gordan coefficients, $Y_{l, \mu - m_s}$ are complex spherical harmonics and ϕ_{m_s} are Pauli spinors

$$\phi_{1/2} = \begin{pmatrix} 1 \\ 0 \end{pmatrix}, \quad \phi_{-1/2} = \begin{pmatrix} 0 \\ 1 \end{pmatrix}. \quad (4.7)$$

In addition to the right-side solutions, we also need the left-hand solutions to construct the Green's function (see Appendix B and C). In free-space, the left-hand solutions are given by

$$J_{\Lambda}^{+}(E, \mathbf{r}) = \left(W/c^2 + \frac{1}{2} \right)^{1/2} \begin{pmatrix} j_l(pr) \chi_{\Lambda}^{\dagger}(\hat{\mathbf{r}}) \\ \frac{-ipcS_{\kappa}}{W+c^2/2} j_l(pr) \chi_{\bar{\Lambda}}^{\dagger}(\hat{\mathbf{r}}) \end{pmatrix}, \quad (4.8)$$

$$N_{\Lambda}^{+}(E, \mathbf{r}) = \left(W/c^2 + \frac{1}{2} \right)^{1/2} \begin{pmatrix} n_l(pr) \chi_{\Lambda}^{\dagger}(\hat{\mathbf{r}}) \\ \frac{-ipcS_{\kappa}}{W+c^2/2} n_{\bar{l}}(pr) \chi_{\bar{\Lambda}}^{\dagger}(\hat{\mathbf{r}}) \end{pmatrix}. \quad (4.9)$$

For $r < R_c$, the Dirac equation solutions can only be obtained numerically. By using the phase integral technique [59], the solutions are written in terms of the free-space solutions as (see Appendix B)

$$\psi_\Lambda(E, \mathbf{r}) = \sum_{\Lambda'} \{S_{\Lambda'\Lambda}(E, r)N_{\Lambda'}(E, \mathbf{r}) - C_{\Lambda'\Lambda}(E, r)J_{\Lambda'}(E, \mathbf{r})\}, \quad (4.10)$$

where the r dependent cosine matrix $C_{\Lambda'\Lambda}(E, r)$ and sine matrix $S_{\Lambda'\Lambda}(E, r)$ are defined as

$$C_{\Lambda'\Lambda}(E, r) = p \int_{0 < r' < r} d^3\mathbf{r}' N_{\Lambda'}^+(E, \mathbf{r}') V(\mathbf{r}') \psi_\Lambda(E, \mathbf{r}') - \delta_{\Lambda\Lambda'}, \quad (4.11)$$

$$S_{\Lambda'\Lambda}(E, r) = p \int_{0 < r' < r} d^3\mathbf{r}' J_{\Lambda'}^+(E, \mathbf{r}') V(\mathbf{r}') \psi_\Lambda(E, \mathbf{r}'). \quad (4.12)$$

Note that this expression is also valid for $r > R_c$, because $S_{\Lambda'\Lambda}(E, r)$ and $C_{\Lambda'\Lambda}(E, r)$ will become constants outside the circumscribed sphere. To distinguish these constants from $S_{\Lambda'\Lambda}(E, r)$ and $C_{\Lambda'\Lambda}(E, r)$ we denote them as $S_{\Lambda'\Lambda}(E)$ and $C_{\Lambda'\Lambda}(E)$. Equations (4.10), (4.11) and (4.12) form a set of coupled integral equations. $C_{\Lambda\Lambda'}(E, r)$ and $S_{\Lambda\Lambda'}(E, r)$ can be obtained by solving the corresponding differential equations

$$\frac{d}{dr} S_{\Lambda'\Lambda}(E, r) = r^2 \int d\hat{\mathbf{r}} p J_{\Lambda'}^+(E, \mathbf{r}) V(\mathbf{r}) \psi_\Lambda(E, \mathbf{r}), \quad (4.13)$$

$$\frac{d}{dr} C_{\Lambda'\Lambda}(E, r) = r^2 \int d\hat{\mathbf{r}} p N_{\Lambda'}^+(E, \mathbf{r}) V(\mathbf{r}) \psi_\Lambda(E, \mathbf{r}). \quad (4.14)$$

Note that the integral is only upon the angular part. For regular solutions, the boundary conditions are

$$\psi_\Lambda(E, \mathbf{r})_{\mathbf{r} \rightarrow 0} = J_\Lambda(E, \mathbf{r}). \quad (4.15)$$

or equivalently

$$S_{\Lambda'\Lambda}(E, 0) = 0, \quad (4.16)$$

$$C_{\Lambda'\Lambda}(E, 0) = -\delta_{\Lambda\Lambda'}. \quad (4.17)$$

To see the boundary conditions are well defined, we note the effective electric potential has a spherically symmetric $1/r$ behavior at the origin. As a result the integrals on the

right side of equation (4.11) and (4.12) vanish at the origin because spherical Bessel functions with different l indices can not be coupled by spherical potential.

Next, we proceed to the discussion of technical details on solving the coupled differential equations. The explicit expressions of the differential equations (4.13) and (4.14) are given by

$$\frac{d}{dr} S_{\Lambda'\Lambda}(E, r) = \sum_{\Lambda''} a_{\Lambda''\Lambda'}(E, r) S_{\Lambda''\Lambda}(E, r) - \sum_{\Lambda''} b_{\Lambda''\Lambda'}(E, r) C_{\Lambda''\Lambda}(E, r), \quad (4.18)$$

where

$$a_{\Lambda''\Lambda'}(E, r) = r^2 \int d\hat{\mathbf{r}} p J_{\Lambda'}^+(E, \mathbf{r}) V(\mathbf{r}) N_{\Lambda''}(E, \mathbf{r}), \quad (4.19)$$

$$b_{\Lambda''\Lambda'}(E, r) = r^2 \int d\hat{\mathbf{r}} p J_{\Lambda'}^+(E, \mathbf{r}) V(\mathbf{r}) J_{\Lambda''}(E, \mathbf{r}), \quad (4.20)$$

and

$$\frac{d}{dr} C_{\Lambda'\Lambda}(E, r) = \sum_{\Lambda''} c_{\Lambda''\Lambda'}(E, r) S_{\Lambda''\Lambda}(E, r) - \sum_{\Lambda''} d_{\Lambda''\Lambda'}(E, r) C_{\Lambda''\Lambda}(E, r), \quad (4.21)$$

where

$$c_{\Lambda''\Lambda'}(E, r) = r^2 \int d\hat{\mathbf{r}} p N_{\Lambda'}^+(E, \mathbf{r}) V(\mathbf{r}) N_{\Lambda''}(E, \mathbf{r}), \quad (4.22)$$

$$d_{\Lambda''\Lambda'}(E, r) = r^2 \int d\hat{\mathbf{r}} p N_{\Lambda'}^+(E, \mathbf{r}) V(\mathbf{r}) J_{\Lambda''}(E, \mathbf{r}). \quad (4.23)$$

For full potential calculations, the effective potential $V(\mathbf{r})$ is expanded in terms of the complex spherical harmonics

$$V(\mathbf{r}) = \sum_{L_v} V_{L_v}(r) Y_{L_v}(\hat{\mathbf{r}}). \quad (4.24)$$

The angular integral in equation (4.19), (4.20), (4.22) and (4.23) can be done analytically and written in terms of the Gaunt coefficients

$$C_{L', L''}^{L''} = \int d\hat{\mathbf{r}} Y_L(\hat{\mathbf{r}}) Y_{L'}^*(\hat{\mathbf{r}}) Y_{L''}(\hat{\mathbf{r}}). \quad (4.25)$$

In practice, the differential equations are solved on exponential radial grid $r = r_0 \exp(x)$,

using the fourth-order Bashforth-Adams-Moulton predictor-corrector method. More details on the numerical implementation is shown in Appendix D, with muffin-tin potential as an example.

After we obtain the solutions of the Dirac equation, we can use them to construct the single-site Green's function, which has the following expression (see Appendix C) for $r' > r$

$$G(E, \mathbf{r}, \mathbf{r}') = \sum_{\Lambda\Lambda'} Z_{\Lambda}(E, \mathbf{r}) t_{\Lambda\Lambda'}(E) Z_{\Lambda'}^+(E, \mathbf{r}') - \sum_{\Lambda} Z_{\Lambda}(E, \mathbf{r}) \mathcal{J}_{\Lambda}^+(E, \mathbf{r}'). \quad (4.26)$$

where $\mathcal{J}_{\Lambda'}^+(E, \mathbf{r})$ are the irregular solutions of equation (2.6) with the boundary condition that $\mathcal{J}_{\Lambda'}^+(E, \mathbf{r}) = J_{\Lambda'}^+(E, \mathbf{r})$ outside the Wigner-Seitz cell. $Z_{\Lambda}(E, \mathbf{r})$ is another set of regular solutions defined as

$$Z_{\Lambda}(E, \mathbf{r}) = p \sum_{\Lambda'} \psi_{\Lambda'}(E, \mathbf{r}) S_{\Lambda'\Lambda}^{-1}(E). \quad (4.27)$$

The t matrix is given by equation (C.14) in Appendix C and the explicit expression is

$$t_{\Lambda\Lambda'}(E) = -\frac{1}{p} \sum_{\Lambda''} S_{\Lambda\Lambda''}(E) (C_{\Lambda''\Lambda'}(E) - i S_{\Lambda''\Lambda'}(E))^{-1}. \quad (4.28)$$

From the Green's function, it's straightforward to calculate physical quantities of the system. Here we focus on the charge density and the density of states. The first one is necessary to calculate the new potential in a SCF cycle and the latter one is needed to determine the Fermi energy of the system. The charge density is given by

$$\rho(\mathbf{r}) = -\frac{1}{\pi} \text{Im} \text{Tr} \int_0^{E_F} G(E, \mathbf{r}, \mathbf{r}) dE, \quad (4.29)$$

where the Fermi energy E_F is chosen to give the correct number of total electrons. The density of states is given by

$$n(E) = -\frac{1}{\pi} \text{Im} \text{Tr} \int_{\Omega} G(E, \mathbf{r}, \mathbf{r}) d\mathbf{r}, \quad (4.30)$$

where Ω denotes the wigner seitz cell. For real energy, the imaginary part of the $Z\mathcal{J}^+$ term in equation (4.26) vanishes, so we can instead write the density of states $n(E)$ and

the charge density $\rho(\mathbf{r})$ as

$$n(E) = -\frac{1}{\pi} \text{Im} \text{Tr} \int_{\Omega} \sum_{\Lambda\Lambda'} Z_{\Lambda}(E, \mathbf{r}) t_{\Lambda\Lambda'}(E) Z_{\Lambda'}^+(E, \mathbf{r}) d\mathbf{r}, \quad (4.31)$$

$$\rho(\mathbf{r}) = -\frac{1}{\pi} \text{Im} \text{Tr} \int_0^{E_F} \sum_{\Lambda\Lambda'} Z_{\Lambda}(E, \mathbf{r}) t_{\Lambda\Lambda'}(E) Z_{\Lambda'}^+(E, \mathbf{r}) dE. \quad (4.32)$$

The benefit of this expression is that it does not contain the irregular solutions $\mathcal{J}_{\Lambda}(\mathbf{r})$, which are difficult to evaluate precisely near the origin.

4.3 Krein's Theorem

For single-site scattering, the density of states can be calculated from either the Green's function or the Krein's theorem [61, 62]. A comparison of the two results will be a good test of our code. First we focus on the Krein's theorem method. Details of the relation between the Krein's theorem and the Green's function in the non-relativistic case has been derived in a previous paper [63] and most of them can also be applied to the relativistic case. Therefore, in this section we will just establish notation and quote known results. By applying the Krein's theorem to the scattering theory, it has been proved that the integrated density of states (IDOS) is given by

$$N_{\text{K}}(E) = -2\xi(E) = N(E) - N_0(E) + n_c, \quad (4.33)$$

where $N(E)$ is the integrated single-site density of states, $N_0(E)$ is the free electron integrated density of states, n_c is the total number of core states, which is irrelevant here since we are only interested in valence electrons. $\xi(E)$ is the Krein's spectral shift function [61] related to the standard unitary S-matrix $\mathbf{S}(E)$ by [64]

$$e^{-i2\pi\xi(E)} = \det\mathbf{S}(E). \quad (4.34)$$

The S-matrix is obtained from the t matrix using the relation

$$\mathbf{S}_{\Lambda\Lambda'}(E) = \delta_{\Lambda\Lambda'}(E) - 2ipt_{\Lambda\Lambda'}(E). \quad (4.35)$$

The Krein DOS $n_K(E)$ is obtained by taking the derivative of N_K ,

$$n_K(E) = \frac{dN_K(E)}{dE}. \quad (4.36)$$

Note that $n_K(E)$ is the Krein DOS for the entire space. To compare with the DOS obtained from the Green's function, we express $n_K(E)$ inside and outside the region bounded by a sphere of radius R_c in terms of Green's function as

$$n_K^{\text{in}}(E) = -\frac{1}{\pi} \text{Im} \int_{0 < r < R_c} \text{Tr}(G(E, \mathbf{r}, \mathbf{r}) - G_0(E, \mathbf{r}, \mathbf{r})) d\mathbf{r}, \quad (4.37)$$

$$n_K^{\text{out}}(E) = -\frac{1}{\pi} \text{Im} \int_{r > R_c} \text{Tr}(G(E, \mathbf{r}, \mathbf{r}) - G_0(E, \mathbf{r}, \mathbf{r})) d\mathbf{r}, \quad (4.38)$$

and we should have $n_K(E) = n_K^{\text{in}}(E) + n_K^{\text{out}}(E)$. The $G(E, \mathbf{r}, \mathbf{r})$ term in equation (4.37) is evaluated numerically while the $G_0(E, \mathbf{r}, \mathbf{r})$ term is evaluated analytically using the following expression of the free space Green's function

$$\text{Tr} G_0(E, \mathbf{r}, \mathbf{r}) = \lim_{\mathbf{r}' \rightarrow \mathbf{r}} -\frac{1}{c^2} \text{Tr} (\alpha \cdot \mathbf{p} + \beta c^2/2 + W) \frac{e^{ip(\mathbf{r}-\mathbf{r}')}}{4\pi(\mathbf{r}-\mathbf{r}')} \quad (4.39)$$

$$= -\frac{ipW}{\pi c^2}. \quad (4.40)$$

Therefore, the contribution to the DOS from the inside integral is

$$n_K^{\text{in}}(E) = -\frac{1}{\pi} \text{Im} \int_0^{R_c} \text{Tr} \sum_{\Lambda\Lambda'} Z_\Lambda(E, \mathbf{r}) t_{\Lambda\Lambda'}(E) Z_{\Lambda'}^+(E, \mathbf{r}) d\mathbf{r} - \frac{4pW}{3c^2\pi} R_c^3. \quad (4.41)$$

For $r > R_c$, using another expression of the Green's function

$$G(E, \mathbf{r}, \mathbf{r}) = G_0(E, \mathbf{r}, \mathbf{r}) - p^2 \sum_{\Lambda\Lambda'} H_\Lambda(E, \mathbf{r}) t_{\Lambda\Lambda'}(E) H_{\Lambda'}^+(E, \mathbf{r}), \quad (4.42)$$

where $H_\Lambda(E, \mathbf{r}) = J_\Lambda(E, \mathbf{r}) + iN_\Lambda(E, \mathbf{r})$, the outside contribution to the DOS is

$$n_K^{\text{out}}(E) = \text{Im} \frac{2p^2W}{\pi c^2} \int_{R_c}^{\infty} \sum_l h_l(pr) t_l h_l(pr) r^2 dr. \quad (4.43)$$

This double Hankel function integral also occurs in the non-relativistic case [63] and can be done analytically using [65]

$$\int_R^\infty h_l(pr)^2 r^2 dr = \frac{R^3}{2} (h_{l-1}(pr)h_{l+1}(pr) - h_l(pr)^2). \quad (4.44)$$

To compare the Krein's theorem method and the Green's function method, the DOS of copper and vanadium are calculated and shown in figure 4.1. The input potentials are obtained from non-relativistic self-consistent full-potential KKR calculations. In both calculations angular momentum cut-off $l_{max} = 4$ and 256 energy points are used. In general the relative error is within the order of 10^{-4} , which indicates an excellent agreement between the two methods. Most of the errors are from the small number of energy points and the relative primitive way to calculate n_K from the numerical derivative of N_K . If $l_{max} = 2$ is used, we find the relative error is at the order of 10^{-2} .

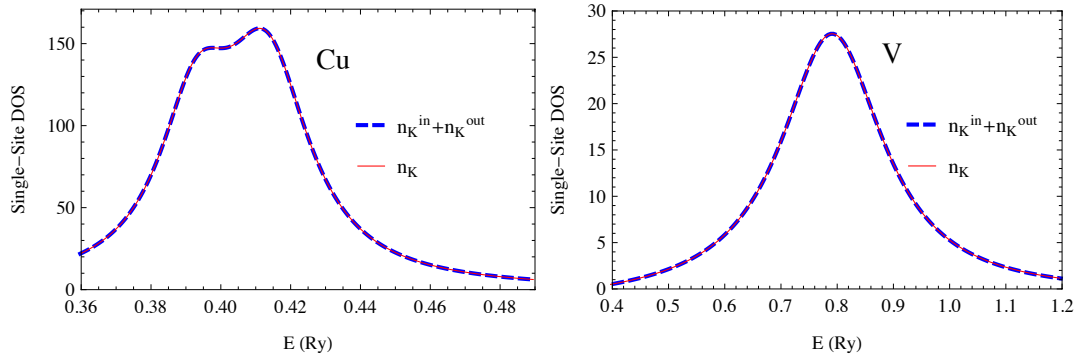


Figure 4.1: (Color online) Comparison of the DOS from Green's function method and the Krein's theorem method. The blue solid lines show the Krein DOS n_K . The dashed lines show $n_K^{in} + n_K^{out}$ calculated using the Green's function. Because of the good agreement the two lines actually overlap.

4.4 Single-Site DOS

The full potential effects and the relativistic effects can be directly observed in the single-site DOS. As the first example, the DOS of noble metals, i.e., copper, silver and gold are calculated using both relativistic and nonrelativistic Green's function methods. The results are shown in figure 4.2. In all calculations the angular momentum expansion cut-offs l_{max} are set to be 4 and the expansion cut-offs for potentials are set to be

$2 \times l_{max}$ to satisfy the angular momentum triangular relation. Both the relativistic effects and the full potential effects are well demonstrated by the three peaks in the relativistic DOS plots of silver. The large energy differences between the leftmost peak and the right two peaks are due to relativistic effects, mostly spin-orbit coupling. The smaller difference between the right two peaks is due to full potential effect. The full potential effects of copper and gold, however, do not cause any visible splitting of DOS because their peaks on the right are relatively broad and merge into one single peak.

A better demonstration of the full potential effects and the relativistic effects is the splitting of the IDOS components of the d electrons. According to Krein's theorem, the IDOS components are given by the generalized phase shifts divided by 2π , where the generalized phase shifts are obtained by diagonalizing the S-matrix [66]. As an example we calculated the Krein IDOS components of copper in different cases and the results are shown in figure 4.3. For non-relativistic muffin-tin calculation, all the d electrons degenerate. For relativistic muffin-tin calculation, even though the input potential is spherically symmetric, the IDOS still splits into two parts due to spin-orbit coupling. The introduction of asymmetric potential leads to further splitting in the relativistic full potential calculation. Because of the cubic structure symmetry, the splitting is not complete and the degeneracies still exist. Similar calculations are also performed for silver and gold and the Krein IDOS for relativistic full-potential calculation are shown in figure 4.4, where the splittings due to spin-orbit coupling are more significant. The width of the splitting provides an estimate of the strength of the spin-orbit coupling or full potential effect. For example, for copper, silver and gold the splittings caused by spin-orbit coupling are 0.020 Ry, 0.042 Ry and 0.13 Ry, respectively. This agrees with our expectation that the magnitude of spin-orbit coupling tend to increase for heavier elements.

All the noble elements have face centered cubic structure, therefore the FP effects are comparatively small. To better investigate the FP effects we also calculated the group V elements, where the FP effects should be larger because of they are body centered cubic crystals and are less closely packed. The Krein IDOS components of vanadium, niobium and tantalum are shown in figure 4.5. For Ta the relativistic effect is almost always dominant over the FP effect because of its large nuclear charge. For V and Nb, however, it is easy to observe the competition between FP effects and relativistic effects. At small energies, the FP effects are dominant over the relativistic effects. As a result, the 10 d components evolve into two major branches. The upper branch has

approximately 6 fold degeneracy, with angular momentum index $l, m = 2, 0$ or $2, \pm 2$ and the lower branch has 4 fold degeneracy, with $l, m = 2, \pm 1$. At high energies, however, the relativistic effects will be dominant. Although there are still two branches, due to spin orbit coupling, the good quantum number is the total angular momentum j . The upper branch now is 4 fold degenerate, with $j = 3/2$ and the lower branch is 6 fold degenerate, with $j = 5/2$. This is why in the intermediate region the two components in the middle move from the lower branch to the upper branch as the energy increase.

At the end of this section we would like to discuss some general features in the plots: The first one is that the resonance peak tends to be sharper when the center of the peak is located at lower energy. This can be best understood by imagining the energy of the d-resonance moves to negative, at that point, the resonance peak will become a delta function and this corresponds to a bound state of the system. The second one is that the resonance peak in the relativistic case tends to move toward lower energies compared to the non-relativistic one. Taken to the extreme it means a resonance state can become a bound state due to relativistic effects. This can be seen as a result of relativistic contraction: the electrons move closer to the nucleus, which effectively expands the size of the potential, therefore more bound states can be accommodated.

4.5 Single-Site Charge Density

In addition to the density of states, the electron charge density distribution is another quantity that is essential for a self-consistent electronic structure calculation. Again we focus our attention to single-site scattering and hence only show the single-site charge densities here. Also by “charge density” we actually mean the valence electron charge density. Using equation (4.29), the single-site charge density can be found by integrating the Green’s function over energy. It’s convenient to expand the charge density in terms of the spherical harmonics

$$\rho(\mathbf{r}) = \sum_{l=0}^{2 \times l_{\max}} \sum_{m=-l}^l \rho_{l,m}(r) Y_{l,m}(\theta, \phi). \quad (4.45)$$

Because of the cubic symmetry in the elements we calculated, for $2 \times l_{\max} = 8$ the only non-vanishing components are $\rho_{0,0}, \rho_{4,0}, \rho_{4,\pm 4}, \rho_{6,0}, \rho_{6,\pm 4}, \rho_{8,0}, \rho_{8,\pm 4}$ and $\rho_{8,\pm 8}$. Moreover, not all of the charge density components are independent [57]. For example, we should

have $\rho_{4,4} = \rho_{4,-4} = \sqrt{5/14} \rho_{4,0}$ for all cubic crystal systems. Checking the symmetry structure of the charge density also serves as a verification of our results.

As an example, we calculated the charge density components of tantalum, and the proportional relationship of $\rho_{4,0}$ and $\rho_{4,4}$ is shown in figure 4.7, with relative error of the ratio found to be within 10^{-7} . We also studied the relativistic effects by comparing the relativistic and nonrelativistic charge density components $\rho_{0,0}$ as shown in figure 4.6. The non-relativistic limit of our method is also taken by setting $1/c = 0$ and compared with the non-relativistic Green's function method to verify our results. From figure 4.6 we see the relativistic charge density contracts towards the origin compared to the non-relativistic one,¹ which is a typical relativistic phenomenon [67]. Taking a closer look, the relativistic contraction is best demonstrated by the asymptotic behavior of the charge density near the origin, as shown in figure 4.8. The non-relativistic $\rho_{0,0} \approx A(1 - \alpha r)$ [57] near the origin, with $\alpha = 2Z$; The relativistic $\rho_{0,0}$, however, demonstrates a weak singular behavior. This is no surprise since it's well known that when the nucleus is considered as a point charge, the relativistic $S_{1/2}$ and $P_{1/2}$ partial waves will behave as $r\sqrt{\kappa^2 - \zeta^2 - 1}$ around the origin [18], where $\zeta = 2Z/c$. Note that this divergence is not pathological because when integrated around origin, $\rho_{0,0}$ will be multiplied by r^2 , which leads to a finite value. As a final check of our results, we compared the magnitude of the charge density components and find the total charge density is indeed positive everywhere.

4.6 Conclusions

We have demonstrated the construction of the RFP single-site Green's function using the scattering matrices and solutions obtained from directly solving the Dirac equations. Compared to other approaches, our method employs the sine and cosine scattering matrices formalism. As a result, no matching on the boundary is needed for solving the Dirac equation.

This RFP method is successfully implemented to calculate the Green's functions. To test the code, the single-site DOS of noble metals and group V elements are calculated using both the Krein's theorem method and the Green's function method and

¹This is not necessarily true for self-consistent calculation, in which the relativistic contraction applies first to inner electrons and the outer shell d-states can be shifted outwards as the nuclear potential gets more screened

an excellent agreement between the two is found. By studying the single-site DOS and the scattering phase shifts, we thoroughly investigated the relativistic effects and the full-potential effects in single-site scattering. Finally, using tantalum as an example, we investigated the relativistic contraction of the charge density and the asymptotic behavior of charge density near the origin.

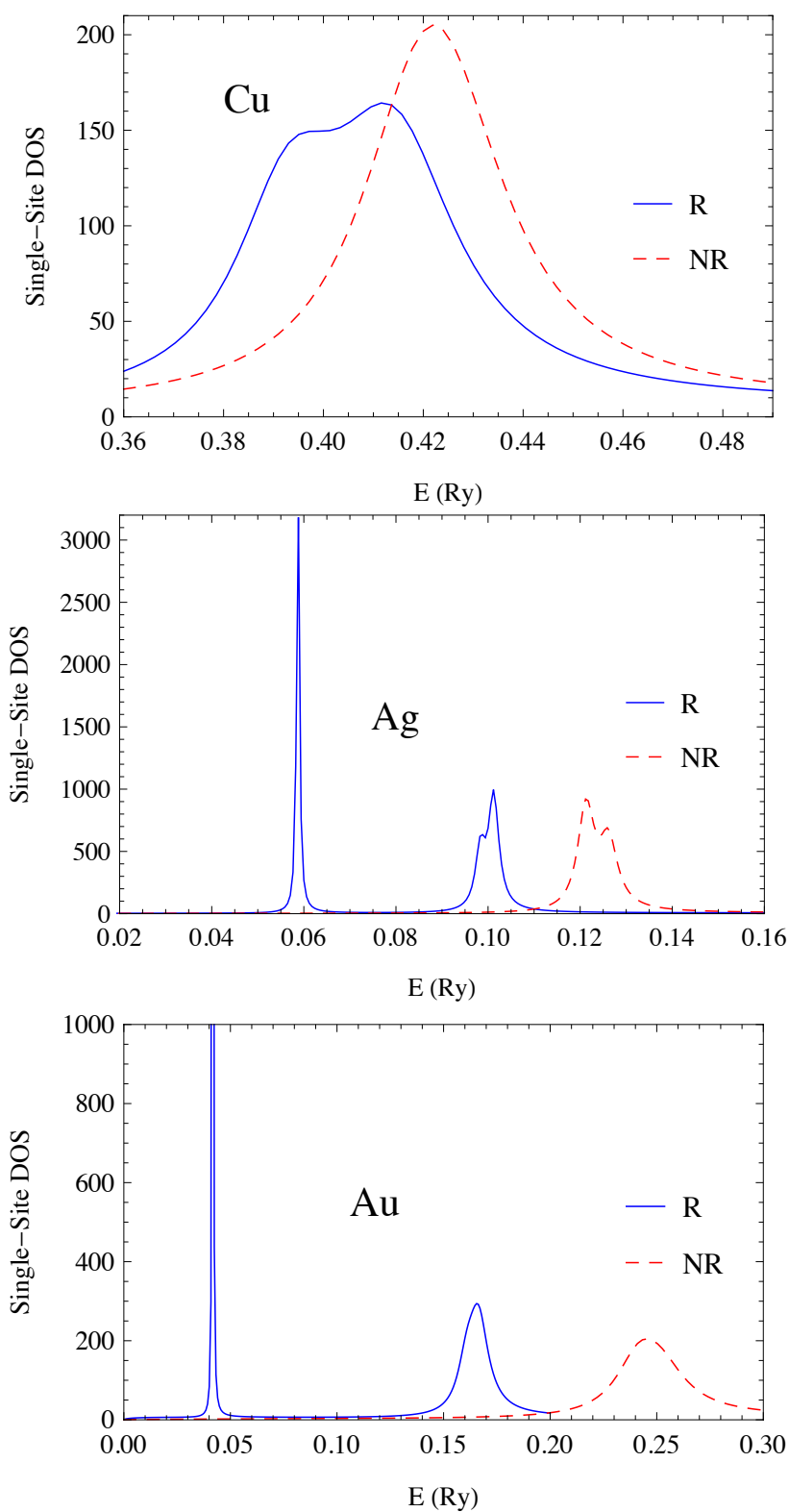


Figure 4.2: (Color online) Comparison of the relativistic and nonrelativistic single-site DOS of noble metals. The blue solid lines are the DOS calculated from the relativistic full potential Green's function method. The red dashed lines are the DOS calculated from the non-relativistic full potential Green's function method, which solves the Schrödinger's equation. Note that the first peak of Au is not completely shown because it's too sharp.

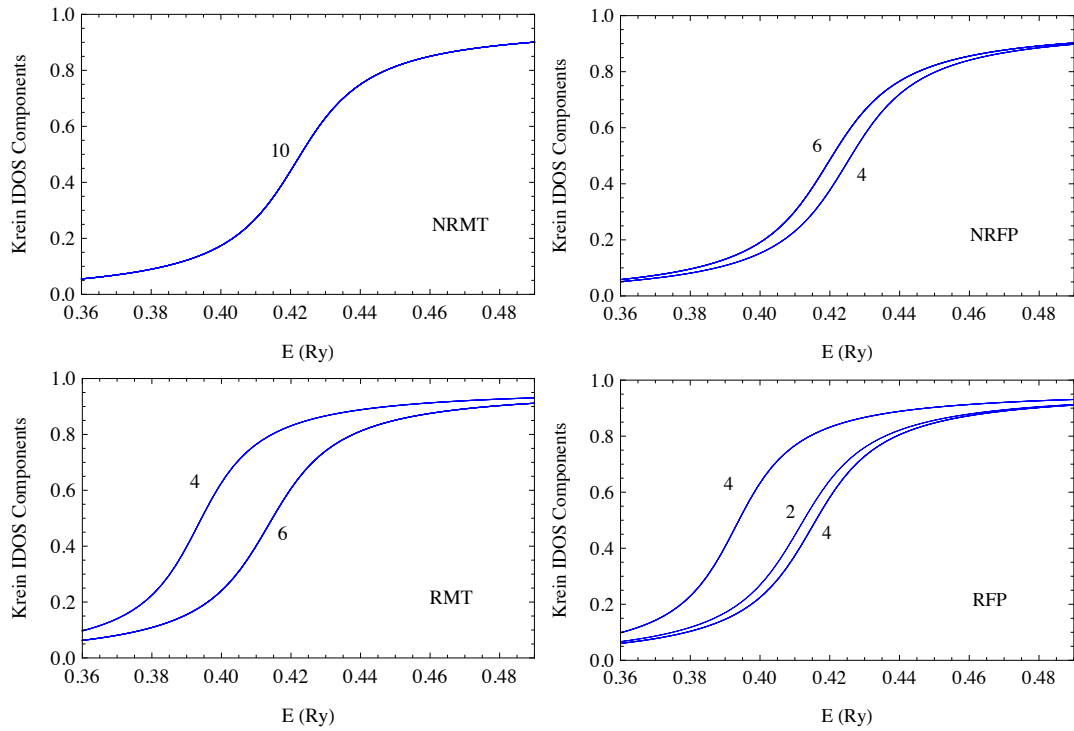


Figure 4.3: The partial Krein IDOS of d electrons of copper corresponding to non-relativistic muffin-tin (NRMT), non-relativistic full potential (NRFP), relativistic muffin-tin (RMT) and relativistic full potential (RFP) calculations. There are 10 d channels in total and the number of degeneracy is shown for each curve.

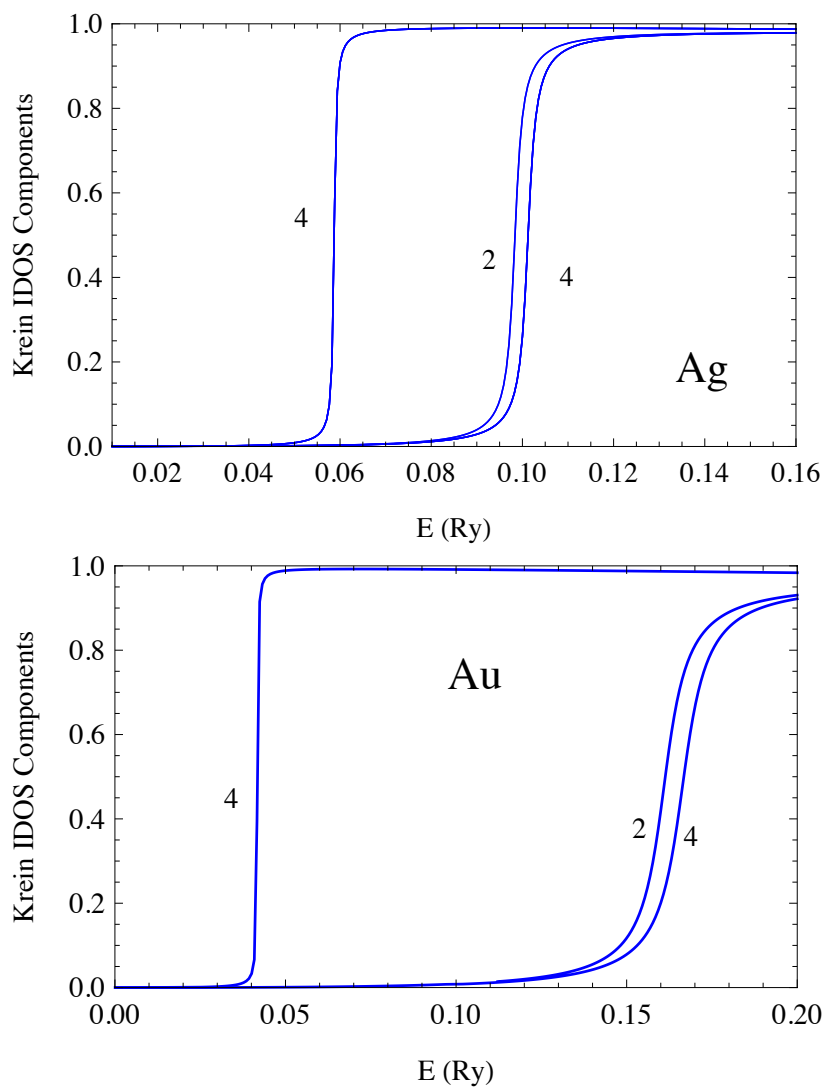


Figure 4.4: The partial IDOS of d electrons of silver and gold in relativistic full potential calculation. There are 10 d channels in total and the number of degeneracy is shown for each curve.

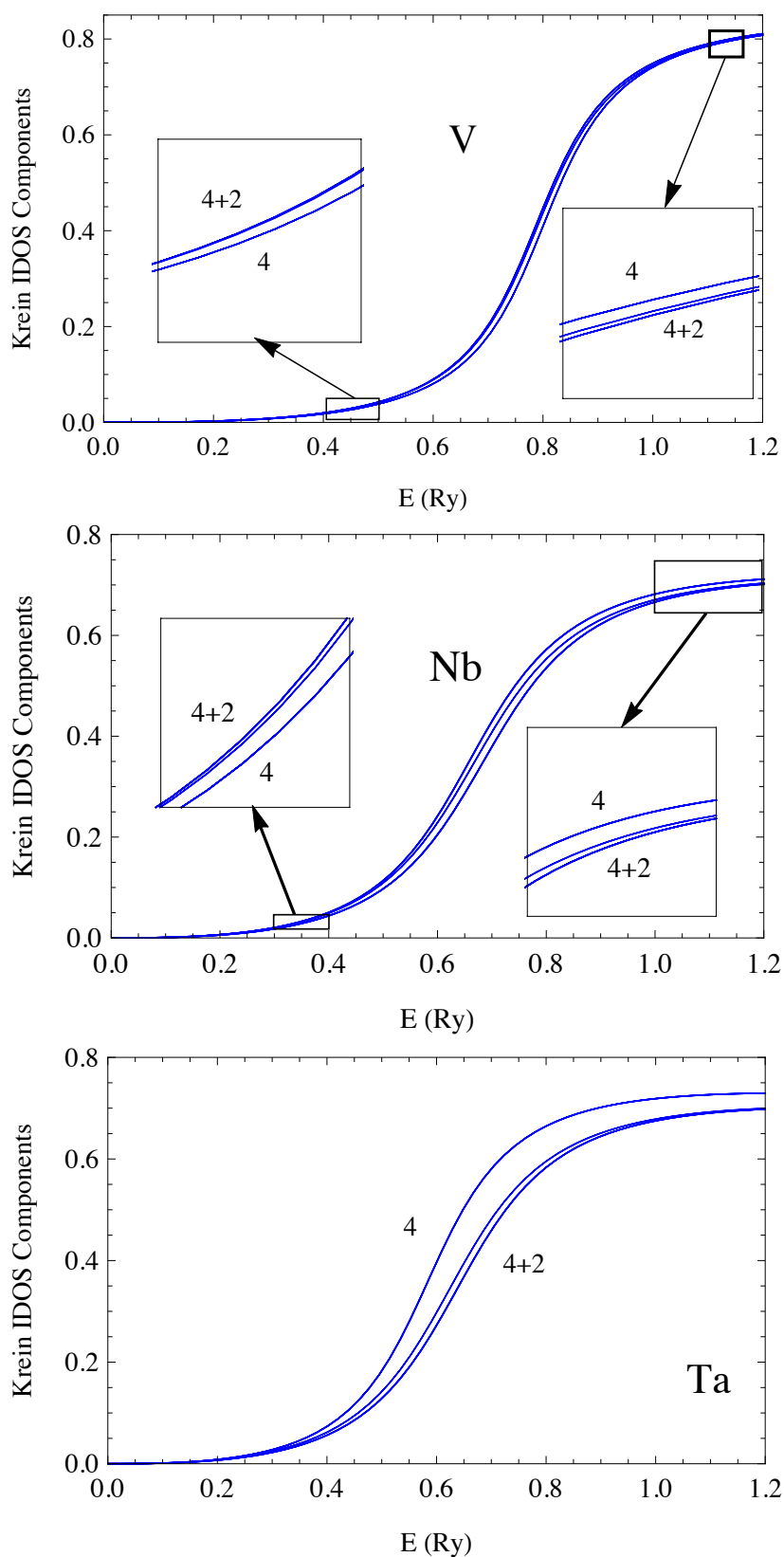


Figure 4.5: The Krein IDOS components of the d electrons of group V elements. There are 10 d channels in total and the number of degeneracy is shown for each curve.

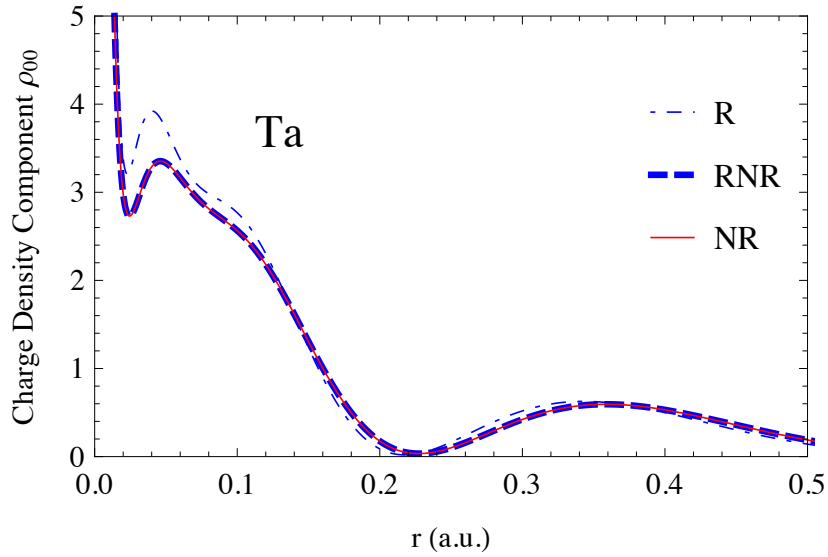


Figure 4.6: (Color online) The $l, m = (0, 0)$ component of the valence-band charge density of tantalum calculated with relativistic (R) method, non-relativistic (NR) Green's function method that solves Schrödinger's equation, and relativistic method at non-relativistic limit (RNR).

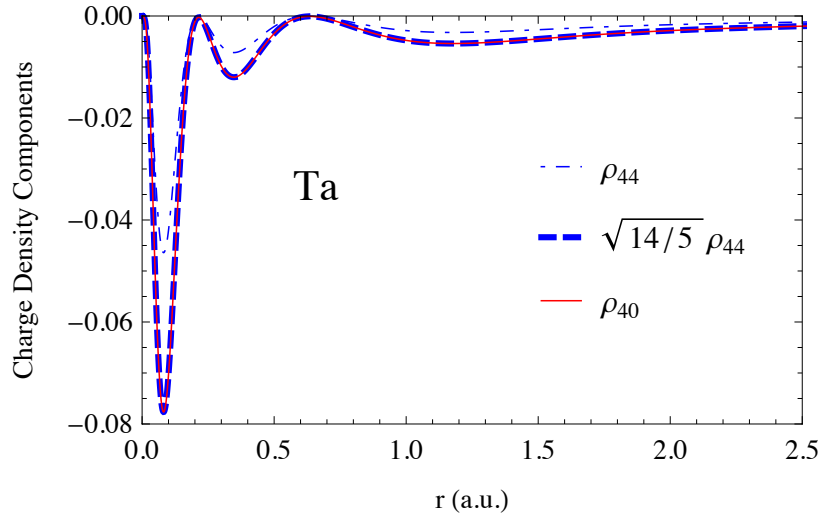


Figure 4.7: (Color online) The $l, m = (4, 0)$ component of the valence-band charge density of copper. Comparison of $\rho_{4,0}$ and $\sqrt{14/5} \rho_{4,4}$ is made to test the cubic symmetry in our results.

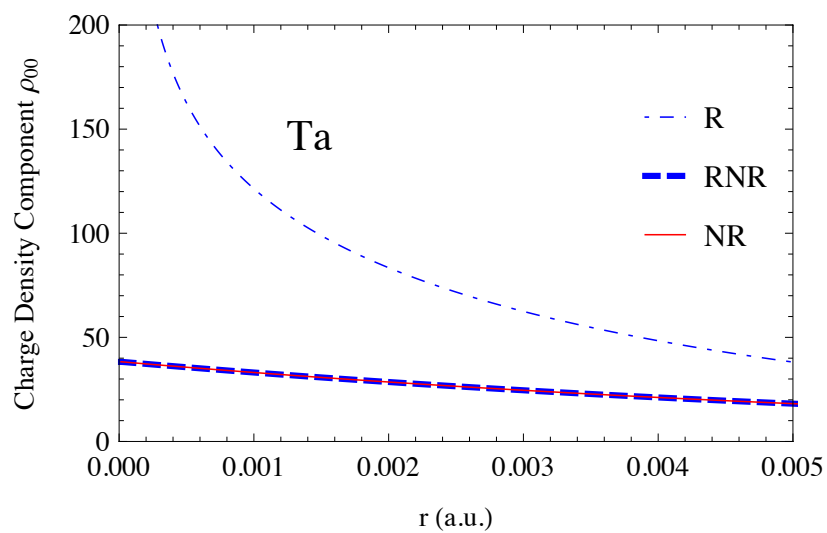


Figure 4.8: (Color online) Comparison of the relativistic (R) and nonrelativistic (NR) charge density around the origin. The non-relativistic limit of our relativistic method (RNR) is also shown.

Chapter 5

Relativistic MST: A Pathology-Free Scheme

5.1 Introduction

In MST the Green function is constructed from the regular and irregular solutions of the Kohn-Sham equations. In contrast to the MT scheme, a persistent problem in standard implementation of full-potential MST is that numerical errors in the irregular solutions are very difficult to control near the origin [57]. As a result, the charge density calculated from the Green function exhibits pathologies which can extend to a sizable fraction of the muffin-tin radius. The practice employed by Huhne *et al.* [19] is to drop the non-spherical components of the potential within a cutoff radius r_{ns} . While this is a good approximation in general, unfortunately it also requires extrapolations of the solutions and charge densities within r_{ns} . Therefore, near the nucleus, the charge density of the valence electrons no longer has the correct undulations, which hinders the accurate determination of the Hellmann-Feynman forces. As an improvement, a sub-interval technique is proposed in Ref. [51] to systematically reduce the numerical error by decreasing the step size when approaching the origin. This method still requires spherical potential approximation within a small radius, and is less effective as l_{max} (angular momentum cutoff of the solutions) increases. In Ref. [68], a modified single-site Green function is proposed to avoid directly using the irregular solutions. However, the volume integral of the irregular solutions are still needed to construct the modified Green function.

In all the above methods, the energy integration of the Green function is carried out on the complex plane. A different strategy to overcome the pathology problem is to split the Green function into the single-site part and the multiple scattering part, and perform integration of the single-site Green function along the real axis, while integrating the irregular solution free multiple scattering part on complex energy plane, as demonstrated by Rusanu *et al.* [57]. The key observation is that on the real energy axis, the irregular solutions make no contribution to the charge and spin densities, therefore can simply be ignored when real energy integration is taken. Although this method completely eliminates the pathology of charge density, it is not popular because the real energy integration was considered to be computationally expensive in the presence of sharp d -resonances, and completely fails when shallow bound states exist. However, by making use of an efficient pole-searching algorithm proposed by Yang Wang, we find the real axis energy integration can actually be accomplished reliably and efficiently, with speed similar to the contour integration methods. Furthermore, unlike the unphysical poles due to inverse of the sine matrix [57], the poles obtained in our method directly correspond to the resonance and bound states of the single-atom potential, therefore are essentially unaffected by other atoms and are numerically stable. Finally, because our method explicitly identifies both bound and virtual bound electron states, it provides an excellent framework for implementing schemes, such as LDA+U [69] and self-interaction correction (SIC) [4, 70], aimed at correcting local approximations to the DFT for the effects of strong correlation.

In the following section we explain in detail how the poles of the single-site Green function can be used to facilitate the energy integration of the shallow bound states and the resonance states, with efficiency of this scheme demonstrated at the end. Details of our pole-searching technique are presented in section 5.3. In section 5.4, polonium is used as an example to demonstrate our method. The lattice constants, bulk modulus and crystal structures of Po are calculated from *ab initio* and compared with results from other methods. In section 5.5, the density of states and bulk properties of copper, silver, and gold are calculated as a further test of our method and to quantify the increasing impact of relativistic effects.

5.2 Methods

The two physical quantities of most interest in the present context are the integrated density of states $N(E)$ and the charge density $\rho(\mathbf{r})$. In a typical *ab initio* DFT calculation, these quantities need to be evaluated at each self-consistent loop to determine the new Fermi energy and effective potential. Note that both $N(E)$ and $\rho(\mathbf{r})$ involve the energy integral of the Green function. Unfortunately, for bulk materials a simple energy integration on the real axis turns out to be infeasible due to the dense set of poles in the multiple scattering Green function. One resolution of this problem is to carry out the integration along a contour in the complex energy plane [71], with the observation that the Green function is holomorphic except for poles at the bound states and a cut on the real axis starting at E_b . Because the DOS becomes increasingly smooth the further the contour is distorted into the complex plane, this method has been found to be very efficient. Indeed, deploying Gaussian quadrature integration method, only a few dozen energy points are needed to reach a high accuracy. In practice, however, implementation is hindered by the presence of the irregular solutions in the expression of the Green function, which is commonly written as [23]

$$G(E, \mathbf{r}, \mathbf{r}') = \sum_{\Lambda\Lambda'} Z_{\Lambda}(E, \mathbf{r}) \tau_{\Lambda\Lambda'}(E) Z_{\Lambda'}^+(E, \mathbf{r}') - \sum_{\Lambda} Z_{\Lambda}(E, \mathbf{r}) \mathcal{J}_{\Lambda}^+(E, \mathbf{r}'). \quad (5.1)$$

Remember that Λ stands for the pair of relativistic angular-momentum indices (κ, μ) , $Z_{\Lambda}(E, \mathbf{r})$ and $Z_{\Lambda}^+(E, \mathbf{r})$ are the right-hand and left-hand regular solutions, respectively, $\mathcal{J}_{\Lambda}^+(E, \mathbf{r}')$ are the left-hand irregular solutions, and $\tau_{\Lambda\Lambda'}(E)$ are the scattering-path matrices. The irregular solutions are singular at the origin and are obtained by integrating inward from outside of the bounding sphere. Unfortunately, using standard numerical integration algorithms, the irregular solutions typically have unacceptable numerical errors near the origin, which then results in the aforementioned pathology in the charge density. The reason for this instability is as follows: In the full-potential scheme, the non-spherical potential components couple solutions of the differential equation having different l indices. Near the origin, the irregular solutions diverge as r^{-l-1} , and the coupling of this divergence to that of channels of higher l amplifies the numerical round-off error in the irregular solutions; an effect that is further amplified as the l_{max} use in the differential equation solver is increased.

In our approach, the elimination of this pathological behavior of the Green function

is accomplished by splitting the Green function into the single-site scattering part G_s and the remaining multiple scattering part G_m ,

$$G(E, \mathbf{r}, \mathbf{r}') = G_s(E, \mathbf{r}, \mathbf{r}') + G_m(E, \mathbf{r}, \mathbf{r}'). \quad (5.2)$$

The explicit expression of the $G_s(E, \mathbf{r}, \mathbf{r}')$ is

$$G_s(E, \mathbf{r}, \mathbf{r}') = \sum_{\Lambda\Lambda'} Z_\Lambda(E, \mathbf{r}) t_{\Lambda\Lambda'}(E) Z_{\Lambda'}^+(E, \mathbf{r}') - \sum_{\Lambda} Z_\Lambda(E, \mathbf{r}) \mathcal{J}_\Lambda^+(E, \mathbf{r}'), \quad (5.3)$$

where $t_{\Lambda\Lambda'}(E)$ is the single-site t matrix. For simplicity of the discussion, we only consider the case of one atom per unit cell. The explicit expression of $G_m(E, \mathbf{r}, \mathbf{r}')$ is

$$G_m(E, \mathbf{r}, \mathbf{r}') = \sum_{\Lambda\Lambda'} Z_\Lambda(E, \mathbf{r}) (\tau_{\Lambda\Lambda'}(E) - t_{\Lambda\Lambda'}) Z_{\Lambda'}^+(E, \mathbf{r}'). \quad (5.4)$$

Note that the $Z\mathcal{J}$ term in $G_s(E, \mathbf{r}, \mathbf{r}')$ is real for real energies. Because the single-site DOS and charge density involve only the imaginary part of $G_s(E, \mathbf{r}, \mathbf{r}')$ this term can be ignored. As a result, carrying out the required integration over real energy axis obviates the need to evaluate irregular solutions. As for the multiple scattering contribution, because it is holomorphic on the upper half-plane and doesn't have irregular solutions, the integration then can be carried out along a semi-circle contour, as shown in Fig. 5.1. Note that other than a numerical technique, dividing of the Green function into single-site part and multiple scattering part also provides a natural separation of local and non-local physics. In particular, the single-site Green function obtained could be of interest if one wish to study local physical quantities.

The above technique of avoiding using the irregular solutions is long known, but to efficiently evaluate the energy integral of $G_s(E, \mathbf{r}, \mathbf{r}')$, two obstacles must be overcome. The first one is to properly account for the contribution from sharp resonance states, examples of which are the d -state resonances in noble metals [23] and the p -state resonances of polonium, as shown in Fig. 5.4. In relativistic full potential schemes, these resonance peaks usually get sharper and split into multiple peaks due to spin-orbit coupling and crystal field splitting, and make a straightforward energy integration even more prohibitive. The second difficulty is to carry out the energy integration of the shallow bound states, which have poles right on real axis and make a direct numerical integration unfeasible. These shallow bound states show up, for example, in our

calculation of polonium, as listed in Table 5.1.

The resonance peaks originate from the poles located at the fourth quadrant in the complex plane. As will be explained in the following, these peaks are well approximated by Lorentzians, and the energy integration on the positive axis can be carried out efficiently with a weighted sampling technique. To accomplish this, the single-site Green function in the neighborhood of a scattering resonance is first approximated as

$$G_s(E, \mathbf{r}, \mathbf{r})|_{E \approx E_n} \approx \frac{\psi_n(E, \mathbf{r})\psi_n^\dagger(E, \mathbf{r})}{E - (E_n - i\lambda_n)}, \quad (5.5)$$

where the complex resonance energy has been written in terms of the real and imaginary part as $E_n - i\lambda_n$. By substitution of equation (5.5) into equation (4.30) and using the normalization condition of the wave functions

$$\int_{\Omega} \psi_n(\mathbf{r})\psi_n^\dagger(\mathbf{r})d\mathbf{r} = 1, \quad (5.6)$$

then the density of states around E_n becomes

$$n(E)|_{E \approx E_n} \approx -\frac{1}{\pi} \text{Im} \left(\frac{1}{E - E_n + i\lambda_n} \right) = \frac{1}{\pi} \frac{\lambda_n}{(E - E_n)^2 + \lambda_n^2}, \quad (5.7)$$

which is exactly a Lorentzian function. The values of E_n and λ_n are determined using the pole-searching technique detailed in section 5.3. Now that the approximate behavior of the resonance peaks are known, we can construct a weighted energy mesh to carry out the integration, i.e., an energy mesh that is densest at the resonance peaks. To use this method, we need to find an appropriate cumulative distribution function $F(E)$. Here it is chosen to be

$$F(E) = \sum_n \left(\frac{1}{\pi} \arctan \left(\frac{E - E_n}{\lambda_n} \right) + \frac{1}{2} \right) + \frac{V}{3\pi^2} E^{3/2}, \quad (5.8)$$

where the first part is the integral of the Lorentzian function and the second part is to account for the non-resonance (free-electron) states, with V being the volume of the unit cell. The weighted energy mesh is obtained by uniformly choosing points F_i between $F(0)$ and $F(E_F)$, then solving the inverse of $F(E)$ with, for example, bisection method. In practice, a uniform grid is more convenient to integrate, so a change of variable from E to F is made and the integration is actually carried out on F_i points.

For shallow bound states, the above weighted sampling technique no longer works because what was a Lorentzian function at positive energy evolves into a Dirac delta function at negative energies. We instead carry out the energy integration on small contours that encircle the negative energy poles (see Fig. 5.1). The reason that radius of the contour must be small is to reduce the error caused by not carrying out the integration strictly on real axis. In our experience, this method yields accurate results when the radius of contour chosen to be 10^{-4} Ry.

At the end of this section we would like to discuss the computational efficiency of the weighted sampling scheme. First we compare it with a simple uniform grid integration. This is done by studying the number of energy points needed for the relative error of the number of electrons to be less than 0.001. As shown in Fig. 5.2, for the uniform grid integration, about 60 energy points are needed in copper and approximately 100 energy points are needed for gold. When the weighted sampling technique is used, the numbers of energy points needed decrease to about 30 for both elements, despite the fact that gold has much sharper peaks [23] than copper in the single-site DOS. This demonstrates that the weighted sampling scheme is computationally more efficient and reliable than the uniform grid scheme. Next we compare the weighted sampling scheme with the conventional contour energy integration scheme. In the contour integration method, although Gaussian quadrature method is generally efficient, about 30 energy points are still routinely used due to structures of the Green function close to the real energy axis. Therefore, the numbers of energy points are similar in the two methods. Other than the number of energy points, another fact need to be considered is that, in the conventional method only one energy integration of the Green function is required at each self-consistent loop, while in the weighted sampling scheme both $G_s(E, \mathbf{r}, \mathbf{r}')$ and $G_m(E, \mathbf{r}, \mathbf{r}')$ need to be integrated. However, in the weighted sampling scheme only the regular solutions need to be evaluated, as a result, the overall computational efficiency of the two methods are actually very similar.

5.3 Pole-Searching Technique

The pole-searching technique used here is similar to the one used in the quadratic KKR (QKKR) method [72] to calculate the electronic band structure. In scattering theory, the bound states and resonance states correspond to the poles of the S-matrix $\underline{\mathbf{S}}(E)$ in

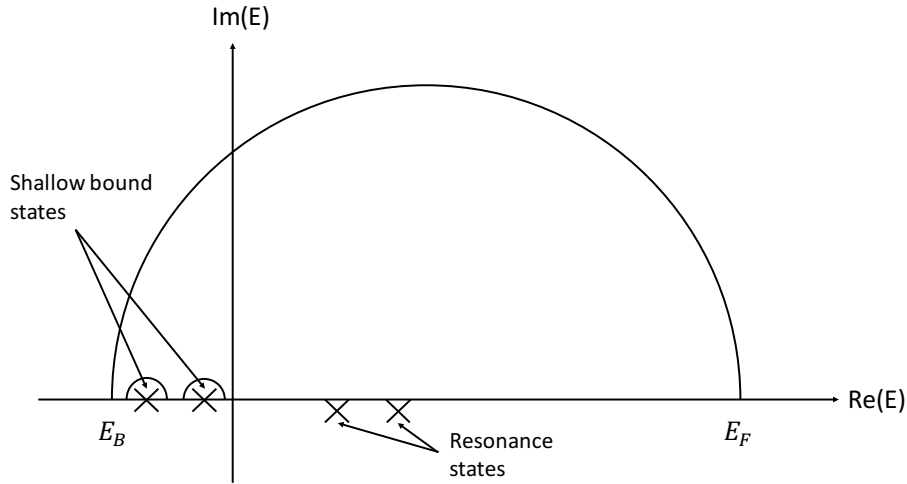


Figure 5.1: Energy integration of the Green function. The multiple scattering part G_m is integrated along the upper semi-circle contour, while the single-site part G_s is integrated on real axis. The shallow bound states are integrated with a tiny circle and the resonance states are integrated using weighted sampling technique.

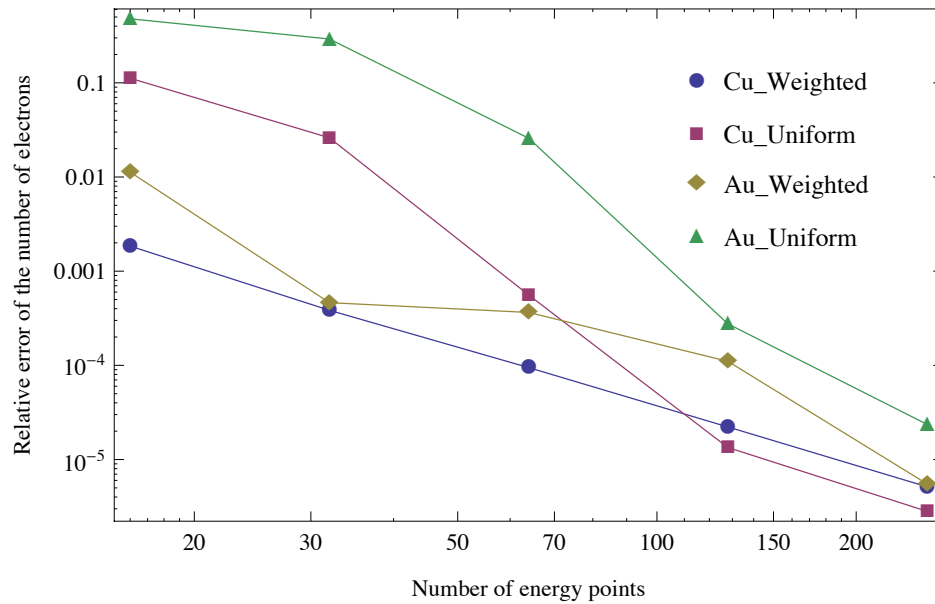


Figure 5.2: (Color online) The relative error of the number of electrons calculated from the single-site Green function $G_s(E, \mathbf{r}, \mathbf{r}')$ for both Cu and Au. Energy points are either obtained using weighted sampling or uniform grid. 16, 32, 64, 128 and 256 energy points are used for each curve and the trapezoidal rule is adopted in energy integration.

the complex energy plane, which can be written as

$$\underline{\mathbf{S}}(E) = [-i\underline{\mathbf{S}}(E) - \underline{\mathbf{C}}(E)] [i\underline{\mathbf{S}}(E) - \underline{\mathbf{C}}(E)]^{-1}, \quad (5.9)$$

where $\underline{\mathbf{S}}(E)$ and $\underline{\mathbf{C}}(E)$ are the sine and cosine scattering matrices [23]. To find the poles of S-matrix we only need to identify the zeros of the Jost matrix $\underline{\mathbf{J}}(E)$, which is given by

$$\underline{\mathbf{J}}(E) = i\underline{\mathbf{S}}(E) - \underline{\mathbf{C}}(E). \quad (5.10)$$

In scattering theory, the Jost matrix is actually a more fundamental quantity than the S matrix because it has no redundant zeros [73], therefore our pole-searching method is numerically more stable than the one used by Rusanu *et al.* [57]. To efficiently determine the zeros of the Jost matrix, a linear algebra method is used. Let us consider a square matrix $\underline{\mathbf{J}}(z)$ of size $L \times L$ (in relativistic case, $L = 2(l_{max} + 1)^2$), and we need to find its zeros, z_p , such that

$$\det [\underline{\mathbf{J}}(z_p)] = 0. \quad (5.11)$$

For the present purposes we are only interested in the poles, ϵ_p , that are close to the real energy axis corresponding to either resonance states ($\epsilon_p > 0$) in the valence band or the shallow bound states ($\epsilon_p < 0$). Accordingly, we choose an energy, in the neighborhood of a pole and perform a quadratic expansion of the matrix around ϵ_0 as follows,

$$\underline{\mathbf{J}}(z) = \underline{\mathbf{J}}(\epsilon_0 + \lambda) = \underline{\mathbf{J}}^{(0)}(\epsilon_0) + \underline{\mathbf{J}}^{(1)}(\epsilon_0)\lambda + \underline{\mathbf{J}}^{(2)}(\epsilon_0)\lambda^2, \quad (5.12)$$

where $\lambda = z - \epsilon_0$. In analogy with the terminology used in the quadratic KKR method, we refer to ϵ_0 as the *pivot energy* for the expansion of $\underline{\mathbf{J}}(z)$. To find the zeros of this quadratic equation, we consider an alternative matrix,

$$\underline{\mathbf{A}}(\lambda) = [\underline{\mathbf{J}}^{(2)}(\epsilon_0)]^{-1} \underline{\mathbf{J}}(\epsilon_0 + \lambda). \quad (5.13)$$

By multiplying $\left[\underline{J}^{(2)}(\epsilon_0)\right]^{-1}$ on both sides of equation (5.12), we get the following expansion,

$$\underline{A}(\lambda) = \lambda^2 - \underline{B}\lambda + \underline{C}, \quad (5.14)$$

where

$$\underline{B} = -\left[\underline{J}^{(2)}(\epsilon_0)\right]^{-1} \underline{J}^{(1)}(\epsilon); \quad \underline{C} = \left[\underline{J}^{(2)}(\epsilon_0)\right]^{-1} \underline{J}^{(0)}(\epsilon), \quad (5.15)$$

Obviously, $\underline{A}(\lambda)$ has zeros at the same energies, $\lambda_p = \epsilon_p - \epsilon_0$, as does $\underline{J}(\epsilon_0 + \lambda)$. We now rewrite equation (5.14) as follows

$$\underline{A}(\lambda) = \lambda^2 - \underline{B}(\lambda - \underline{D}), \quad (5.16)$$

where

$$\underline{D} = \underline{B}^{-1}\underline{C} = -\left[\underline{J}^{(1)}(\epsilon_0)\right]^{-1} \underline{J}^{(0)}(\epsilon). \quad (5.17)$$

The zeros of $\underline{A}(\lambda)$ can now be found using the determinantal equation

$$\det[\underline{A}(\lambda)] = \det[\lambda^2 - \underline{B}(\lambda - \underline{D})] = 0, \quad (5.18)$$

or, equivalently,

$$\det \begin{bmatrix} \lambda - \underline{D} & -\underline{I} \\ \underline{D}^2 & \lambda - \underline{B} + \underline{D} \end{bmatrix} = 0. \quad (5.19)$$

The eigenvalues λ_p ($p = 1, 2, \dots, 2L$) that satisfy this secular equation can be quickly found by diagonalizing the following matrix:

$$\begin{bmatrix} \underline{D} & \underline{I} \\ -\underline{D}^2 & \underline{B} - \underline{D} \end{bmatrix}. \quad (5.20)$$

The zeros of matrix $S(z)$ are thus at $z_p = \lambda_p + \epsilon_0$.

In practice, a simple way of computing the quadratic expansion coefficient matrices in equation (5.12) is to calculate $\underline{J}(z)$ at three energy values: $\epsilon_0 - \lambda$, ϵ_0 , $\epsilon_0 + \lambda$, with λ a small value, then solve the quadratic expansion equations. To search the poles over the

full interval E_b and E_F , a set of panels on the real energy axis is set up and ϵ_0 is chosen at the center of each panel to obtain a first approximation to ϵ_p . In our experience, a few panels are sufficient to determine the position of the resonance poles with an accuracy of 10^{-3} , which is generally much smaller than the width of the resonances. In the presence of shallow bound states, more panels are needed since the radius of the small contour is about 10^{-4} , but then only 5 to 10 Gaussian energy points are needed on the contour since the analytic behavior close to a pole is simple. If desired, the accuracy of the pole location can also be systematically improved through iteration by progressively decreasing the energy window around the pivot energy used to set up the pole location eigenvalue equation.

Finally, We would like to point out that our pole-searching scheme can also be applied to the core electrons, on an equal footing with the valence electrons, i.e., with both bonding and non-spherical potential considered. In normal cases this is unnecessary because the non-bonding of core electrons is generally a very good approximation. For very high pressure, however, it is possible for core electrons to also form bonds [74], and our method should provide a good tool to investigate such problem.

5.4 Polonium

Polonium is an element that is extremely toxic and highly radioactive, and experimental data on its physical properties is scarce. One distinctive property of Po is that it is the only element to crystallize in the simple cubic (sc) structure at ambient conditions. The simple cubic structure has a low atomic packing factor, and is generally considered unstable, both from the point of views of elastic stability [75] and Peierls instability [76]. In addition to the simple cubic phase Po (α -Po), a second, slightly distorted, rhombohedral phase, Po (β -Po), is also found to exist at elevated temperatures. Both the two crystal structures of Po are studied by Beamer and Maxwell [77] using X-ray diffraction, and the lattice constants are reported to be $a = 3.345(2)$ Å for α -Po and $a = 3.359(1)$ Å for β -Po. Later Sando and Lange [78] redetermined the lattice constants using purer Po sample, with $a = 3.359(1)$ Å for α -Po and $a = 3.368(1)$ Å for β -Po.

With the development of electronic structure calculation methods, a number of theoretical studies have been carried out to explain why Po has a stable SC structure. There are still debates on this question, but the general consensus is that relativistic effects play an important role. Using the pseudopotential (PP) method, Kraig *et*

al. [79] showed that SC structure has the lowest total energy among a number of lattice configurations, including face-centered cubic structure (FCC) and body-centered cubic structure (BCC). Min *et al.* [76, 80] utilized the full-potential linearized augmented plane wave (FLAPW) method implemented in the WIEN2K package and found the SC structure is due to SOC. Also using FLAPW, Legut *et al.* [81, 82] investigated the total energy profile of Po and analyzed contributions from different relativistic terms, and concluded instead that it is the relativistic mass-velocity and Darwin terms that stabilize the SC structure. This controversy is mainly due to the tiny total energy difference (especially for all-electron calculation) between the SC structure and trigonal structure of Po, which is at the order of 0.1 mRy, and can be affected by factors such as accuracy of exchange-correlation functional, convergence of the total energy with respect to numerical parameters (for example, we found the convergence with respect to radial grid is important because for different structures the grid generated can be different.), or even which experimental value of the lattice constant to use in the band and phonon dispersion calculations [83]. Compared to the second-variational implementation of SOC in WIEN2K, the fact that our method includes the SOC intrinsically provides some advantage, but in this chapter we do not intend to address the question on which relativistic effects contribute more to the stabilization of sc-Po, mainly because of the aforementioned tiny total energy difference. Instead, we use Po as an example to demonstrate our method, and compare the calculated physical quantities with experiment and other calculation results. The angular momentum cut-off of the wave function is chosen to be $l_{max} = 4$, and $l_{pot} = 8$ for the potential cut-off, in all calculations.

The electron configuration of Po is $[\text{Xe}]4f^{14}5d^{10}6s^26p^4$. The core and semi-core electrons are calculated by solving the Dirac equation for the spherical ($l=0$) component of the potential. The valence electrons, i.e., $6s$ and $6p$ states, are calculated with the FP-MST method. As described in section 5.2, the Green function is split into a single-site part and a multiple scattering part. The poles of the single-site Green function are computed and listed in Table 5.1, and the indices in the first column signify the corresponding predominate angular momentum quantum numbers of each pole. The first two s poles and the following two p poles have negative real part and negligible imaginary part, which are the characteristics of bound states. The other four p poles are in the forth quadrant of the complex plane and correspond to resonance states. The splitting of the six p electrons into a doubly degenerate and weakly bound $p_{1/2}$ core

state and a $p_{3/2}$ fourfold degenerate resonance state just above the energy zero is due to SOC. Note that the cubic symmetry in the potential does not break the degeneracy of either of these spin-orbit split manifolds. The spherical components of the charge densities of the $s_{1/2}$ and $p_{1/2}$ bound states are shown in Fig. 5.3. Clearly, the charge densities demonstrate correct number of nodes. Note that these nodes result from the orthogonality of the valence states to the core states and occur for a radius as small as 0.1 a.u.. As in Ref. [57], this is a further example where the method of simple polynomial extrapolation the charge density, over some significant fraction of the muffin-tin radius, will miss the effects of these undulations.

The single-site DOS and the total DOS of the system are shown in Fig. 5.4; the latter is in good agreement with the scalar relativistic + SO interaction calculation result of Ref. [81]. The total energies and the fitted equation of state Po with SC, BCC and FCC structures are shown in Fig. 5.5. The lattice constant for the SC phase is found to be $a = 3.327 \text{ \AA}$, which, as can be seen in Table 5.2, is in good agreement with the experimental value $a = 3.359 \text{ \AA}$. The bulk modulus is determined to be $B_0 = 55.1 \text{ GPa}$, but unfortunately no reliable experimental value of B_0 is known. In Ref. [84], it is claimed that the experimental bulk modulus of α -Po is 26 GPa, but no reference is given. In Ref. [85] a more complete list of the theoretical results of α -Po is given, from which we see all bulk moduli calculated theoretically are in the range of 40 – 60 GPa, which is much larger than the 26 GPa quotation. We therefore conclude that the bulk modulus found here is reasonable and consistent with the values in the literature.

Table 5.1: The poles of the single-site Green function of Po

| | real part | imaginary part |
|-----------|-----------------|-----------------|
| $s_{1/2}$ | -0.68202472D+00 | 0.16325374D-15 |
| | -0.68202472D+00 | -0.21372993D-15 |
| $p_{1/2}$ | -0.35205135D-01 | -0.12391130D-13 |
| | -0.35205135D-01 | 0.11887440D-13 |
| $p_{3/2}$ | 0.66052385D-01 | -0.37929455D-01 |
| | 0.66052385D-01 | -0.37929455D-01 |
| | 0.66052385D-01 | -0.37929455D-01 |
| | 0.66052385D-01 | -0.37929455D-01 |

Table 5.2: Comparison of the lattice constant (a) and bulk modulus (B_0) calculated with the experimental and theoretical data in the literature.

| | $a(\text{\AA})$ | B_0 (GPa) | Ref. |
|----------------|-----------------|-------------|-----------|
| Exp. | 3.345(2) | | [77] |
| | 3.359(1) | | [78] |
| LDA, PP | 3.28 | 56 | [79] |
| GGA+SO, FLAPW | 3.34 | | [76] |
| LDA+SO, FLAPW | 3.334 | 42.3 | [81] |
| LDA+SO, FLAPW | 3.323 | 47.35 | [85] |
| TB+SO | 3.29 | 51 | [84] |
| LDA+Dirac, MST | 3.327 | 55.1 | This work |

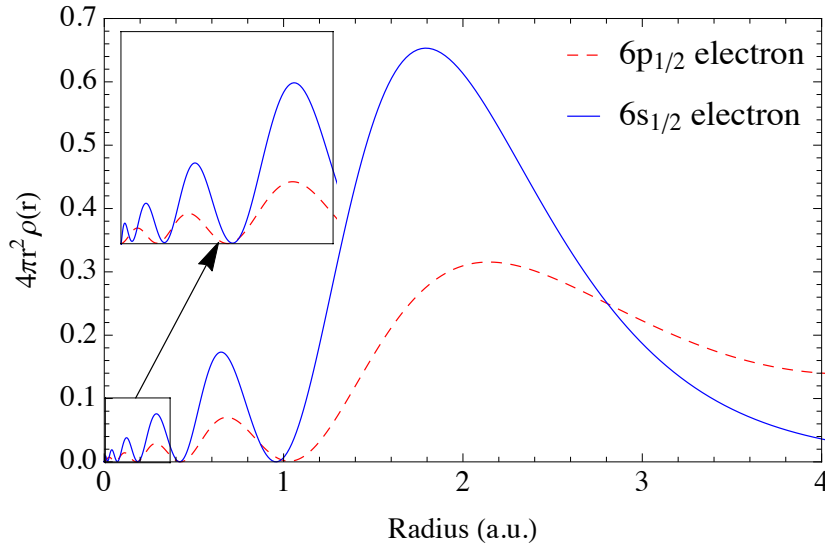


Figure 5.3: (Color online) The spherical component of the charge density of polonium corresponding to the shallow bound states. Note that a $4\pi r^2$ factor has been included. The *red dashed* line corresponds to $6p_{1/2}$ electron and the *blue solid* line corresponds to $6s_{1/2}$ electron.

5.5 Noble Metals

In contrast to polonium, the noble metals have been thoroughly investigated both theoretically and experimentally. In this section, we use them as examples to further test our method. The lattice constants and bulk moduli calculated here are shown in table 5.3 together with experimentally measured values. The results are in excellent agreement with the ones calculated with conventional KKR method [86]. Compared to the experimental data, we underestimate the lattice constants and overestimate the bulk

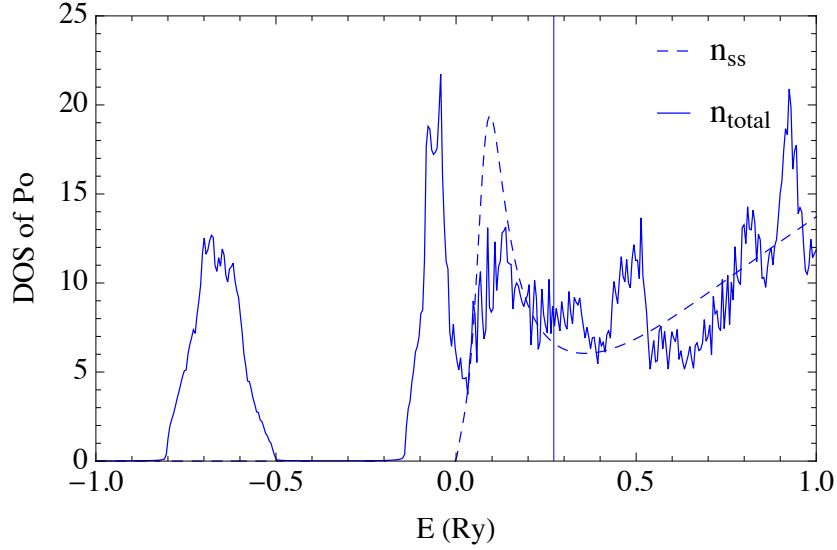


Figure 5.4: Comparison of the total DOS and the single-site DOS of polonium. To show the DOS, the energy is shifted a little up on the real axis, with imaginary part $\text{Im}(E)=0.001$ Ry. The *dashed* line is the single-site DOS and the *solid* line is the total DOS. The vertical line is the Fermi energy. The shallow bound states are not shown on the single-site DOS because they are essentially a set of Dirac δ functions. 125000 k-points are used to calculate the DOS.

Table 5.3: Comparison of calculated lattice constants and bulk moduli of noble metals with the experimental values. The LDA is employed in all calculations. Fully relativistic schemes are used except for the last two columns. In column Au_{NR} all electrons are calculated with nonrelativistic schemes, and relativistic schemes are utilized only for valence electrons in column $\text{Au}_{\text{R-Core}}$.

| | Cu | Ag | Au | Au_{NR} | $\text{Au}_{\text{R-Core}}$ |
|--------------------------|------|------|------|-------------------------|-----------------------------|
| Lattice constants (a.u.) | | | | | |
| This work | 6.65 | 7.55 | 7.60 | 8.03 | 8.17 |
| Experiment | 6.84 | 7.72 | 7.71 | | |
| Bulk Modulus (GPa) | | | | | |
| This work | 191 | 141 | 208 | 112 | 124 |
| Experiment | 137 | 101 | 180 | | |

modulus, which is a well-known characteristic of LDA. As demonstrated in Ref. [86], by employing GGA instead of the LDA functional, much better agreement with the experimental data can be obtained for noble metals.

To demonstrate the impact of relativity, we calculated the bulk properties of Au

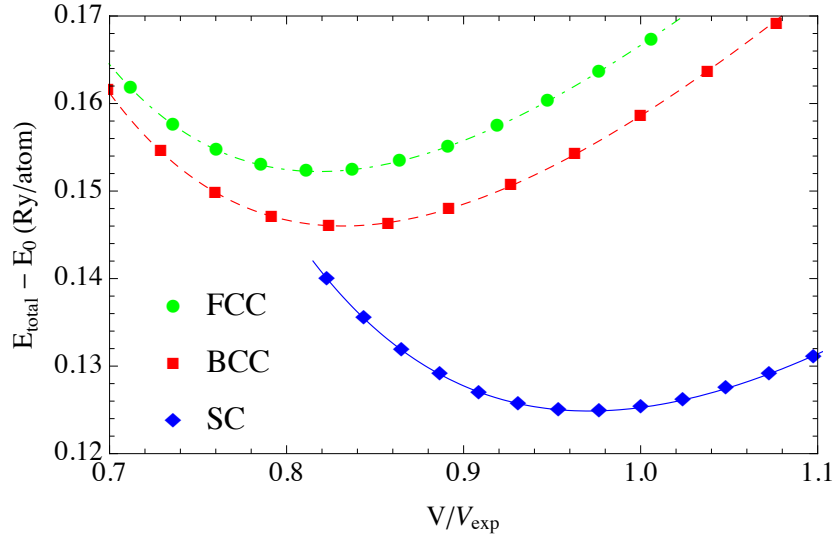


Figure 5.5: (Color online) The volume dependence of total energy plot of polonium. The *solid*, *dashed*, *dot-dashed* lines correspond to the fitted equation of state of simple cubic, BCC, and FCC structures and the shift of total energy $E_0 = -41342$ (Ry/atom). When solving the Dirac equations a total of 1,500 radial mesh points are used within the muffin-tin radius to ensure convergence of the single-site solutions.

with two other schemes. In the nonrelativistic (NR) scheme all relativistic effects are ignored, and in the relativistic core (R-Core) scheme relativistic effects are included only for the core and semi-core electrons. The lattice constants and bulk modulus are shown in the last two columns of Table 5.3 and the total energy vs lattice constants plot is shown in Fig. 5.6. Note that in the R-Core case the lattice constant increases compared to the NR result. This is because when relativity only applies to the core electrons, the nuclear charge of Au is screened better. From these results, it is clear that relativistic effects need to be included for all the electrons, core and valence, when calculating the ground state properties of elements as heavy as Au.

The impact of relativity is also evident in the DOS plots of Fig. 5.7. As a point of reference, the fully relativistic DOS are in good agreement with the results in Ref. [87] for the same set of systems. As can be seen, in all nonrelativistic calculations, the DOS have five main peaks, which is a result of the crystal field symmetry. Under the increasing influence of spin-orbit coupling, these peaks further split into multiple sub-peaks. Overall, the differences between relativistic and nonrelativistic results also grow as the atomic number increase. For silver and gold, the d -bands obtained in the relativistic calculation broaden significantly with the result that the top of the d -band

is much closer to the Fermi energy than in copper. This effect is the result of the relativistic contraction of the inner shell s electrons, whose relativistic effects are more significant than the d -electrons. Actually, this is the well-known explanation of the color of gold; namely, that relativistic effects, decrease the transition energy between $5d$ and $6s$ states which then absorb blue light making the reflected light appear golden to us. The relativistic effects in silver are small compared to gold, therefore Ag still reflects all the visible wavelengths and appears “silver”. Concerning the energy difference between the top of the d -band and the Fermi energy in the relativistic plots, we find they are small compared to those obtained from photoemission measurements [88, 89]. Again, this is a typical feature of DFT calculations, and is shown to be largely corrected [90] by using GW method to account for self-energy effects.

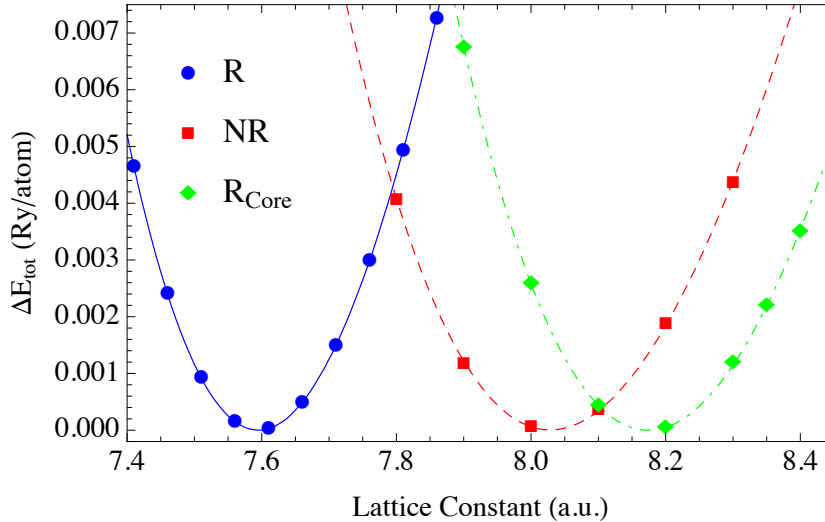


Figure 5.6: (Color online) The total energy of Au calculated using different methods. Different energy shifts are made for each curve so that the lowest point of each line is always zero. In the *solid* line, the core, semicore, and valence electrons are calculated by solving the Dirac equations. In the *dashed* line, the nonrelativistic Schrödinger equations are used for all the electrons. In the *dot-dashed* line the Dirac equations are solved for valence electrons while the Schrödinger equations are solved for core and semi-core electrons.

5.6 Conclusions

We have implemented a new approach to full-potential relativistic MST. By splitting the Green function into two parts and carrying out the energy integration along different

contours, this method requires no evaluation of the irregular solutions and therefore is free of any pathology of the charge density near the origin. By explicitly searching the poles of the single-site Green function, we devised an efficient integration scheme to solve the numerical problems caused by the shallow bound states and the resonance states. The density of states and bulk modulus of polonium are calculated, with the lattice constant found to be $a = 3.327 \text{ \AA}$, and the bulk modulus $B = 55.1 \text{ GPa}$, which yield excellent agreement with experimental data and results from other methods. As a test of our code, we also calculated the DOS and bulk modulus of Cu, Ag, and Au, and discussed the impact of relativistic effects.

The main concern about a real energy integration scheme is that it could be computationally expensive and numerically unstable. As have been demonstrated, this is not the case in our scheme. The weighted sampling technique can also be extended to incorporate finite electronic temperature calculations by including the Matsubara poles, which is important in the Jülich implementations of the KKR method [51,91].

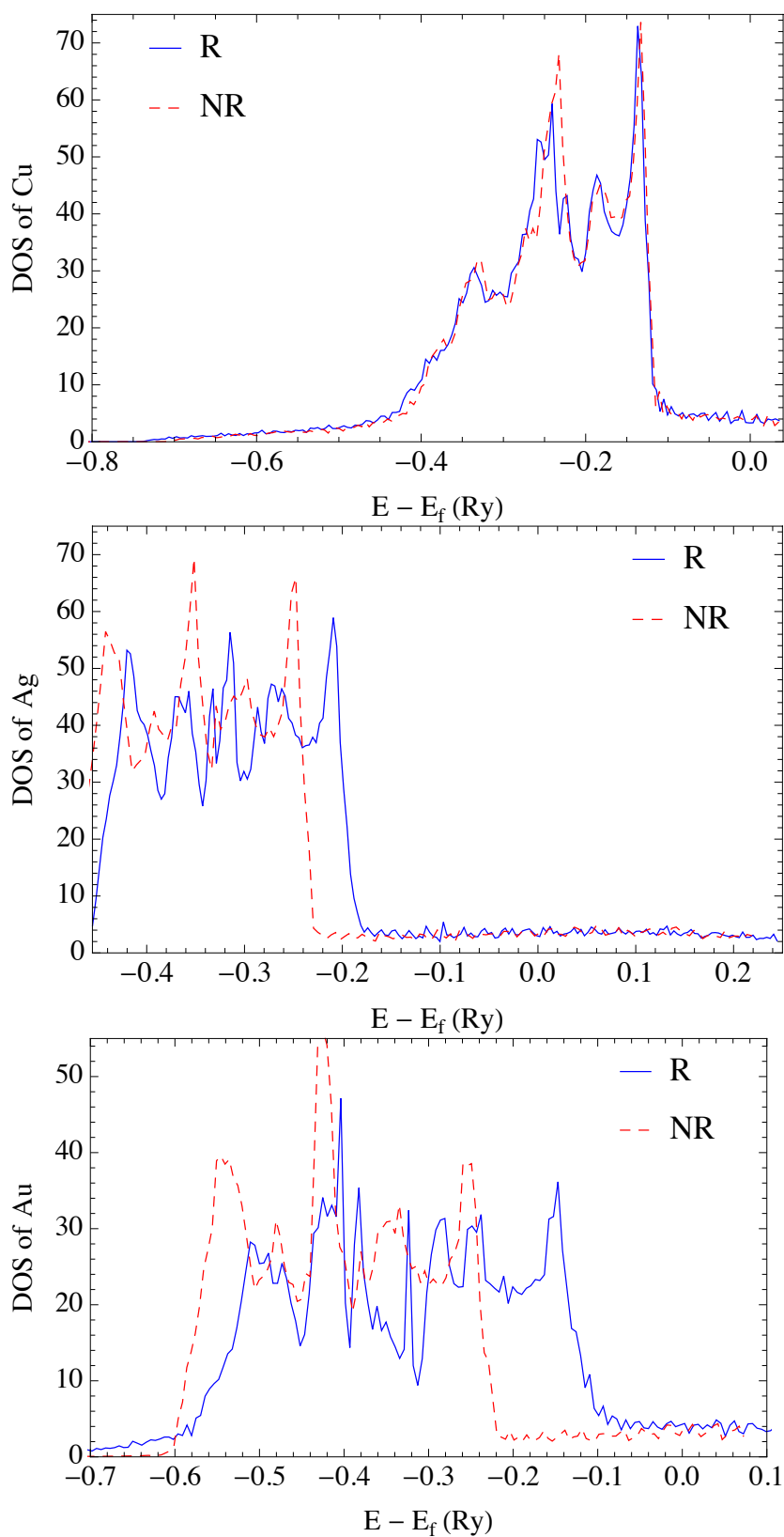


Figure 5.7: (Color online) Comparison of the relativistic and nonrelativistic DOS of Cu, Ag, and Au. The *red dashed* lines are the nonrelativistic results and *blue solid* lines are the relativistic results. Note that shift of the energy by E_f has been applied, so zero on the x-axis corresponds to the Fermi energy.

Chapter 6

Spin-Polarized Calculations and Magnetic Anisotropy

6.1 Application of MST in Magnetism

From the more traditional application of permanent magnets to the more recent spintronics, magnetic materials play an important role in modern day technology. To help us understand the rich diversity of magnetic phenomena, first principles methods must be capable of treating magnetic systems. In the framework of DFT, a simple yet powerful tool to describe magnetism is the spin-polarized approximation, as introduced in chapter 2. Another commonly used approximation to describe magnetic material is the atomic moment approximation, in which the magnetization within each atom is assumed to be fixed along the same direction. This approximation is based on the fact that most atoms have well-localized magnetization, with weak magnetization in the interstitial region. For ferromagnetic (FM) materials, directions of the atomic moments are parallel, and for anti-ferromagnetic (AFM) materials are anti-parallel. Other than FM and AFM, it is also possible for the atomic moments to be noncollinear, with disordered moment directions or magnetic-spin textures. In MST method, direction of the magnetization can be different at any point in the space [92]. However, to simplify the calculation of effective potential in self-consistent loop, the atomic moment approximation is still used in our calculations. Finally, one more approximation is to set the direction of the magnetic field parallel to the spin magnetization. In a recent paper [93], it is shown that this constraint can be lifted by adopting an exchange-correlation func-

tional that has dependence on the transverse gradients of the spin magnetization.

Similar to LDA, the simplest exchange-correlation functional in spin-polarized DFT is the local spin density approximation (LSDA) [94]. The major difference to LDA is that instead of one, there are two effective potentials in LSDA, one corresponds to spin up and the other one spin down. The effective electric and magnetic fields in section 2.4 are given by

$$V_{\text{eff}}(\mathbf{r}) = \frac{1}{2} (V_{\text{up}}(\mathbf{r}) + V_{\text{down}}(\mathbf{r})), \quad (6.1)$$

$$B_{\text{eff}}(\mathbf{r}) = \frac{1}{2} (V_{\text{up}}(\mathbf{r}) - V_{\text{down}}(\mathbf{r})). \quad (6.2)$$

In a self-consistent DFT calculation, starting from initial potentials of $V_{\text{up}}(\mathbf{r})$ and $V_{\text{down}}(\mathbf{r})$, the Kohn-Sham Dirac equation is solved to obtain the charge density using equation (4.29). The magnetization is obtained with

$$\mathbf{m}(\mathbf{r}) = -\frac{\mu_B}{\pi} \text{Im Tr} \int_{E_b}^{E_F} \beta \boldsymbol{\sigma} G(E, \mathbf{r}, \mathbf{r}) dE. \quad (6.3)$$

From the charge density and magnetization, the new effective potentials can then be calculated using LSDA functional. This process repeats until convergence is reached.

Compared to other DFT methods, MST has several advantages in treating magnetic materials. First, the availability of Green function makes it easy to apply the embedding technique. This technique is particularly convenient to treat impurity [95] or nano-structure [49] in an otherwise perfect crystal. Second, by combining coherent potential approximation with MST, systems such as magnetic alloys [39] and dilute magnetic semiconductors [96] can be studied without the cumbersome supercells. Third, in MST the t -matrices and τ -matrices are explicitly calculated. From these matrices, the parameters of the magnetic-exchange interactions can be extracted using the technique of infinitesimal rotation [97]. The mapped parameters can then be fed into the Landau-Lifshitz equation for multiscale simulations. In particular, by extending this technique to the relativistic case, parameters of the Dzyaloshinskii-Moriya interaction can be obtained for the investigation of magnetic skyrmions [98]. Finally, the Green function in MST can be used in the Kubo-Greenwood formalism to calculate transport properties, such as Spin-dependent tunneling conductance [99], spin current density [100], Gilbert damping constant [101], and spin-Hall coefficient [102].

6.2 BCC Iron

As a test of our relativistic spin-polarized MST code, a self-consistent calculation of BCC iron is made and the results are shown in this chapter. The angular momentum cut-offs are $l_{max} = 3$ and $l_{pot} = 6$. The single-site DOS and total DOS are shown in figure 6.1 and the charge density and magnetization components corresponding to $l, m = (0, 0)$ and $l, m = (2, 0)$ are shown in figure (6.2). Note that the $l, m = (2, 0)$ components should vanish for non-relativistic calculations due to the cubic symmetry in BCC Fe. In the relativistic case, the spin-orbit coupling connects the spin space and the real space, and time reversal symmetry breaking in spin space gives rise to breaking of the cubic symmetry in real space, therefore there are nonzero $l, m = (2, 0)$ components in both charge density and magnetization. This effect can be observed experimentally, and the electric field gradients induced by SOC have been calculated [103] by Ebert's group. The spin magnetic moment is found to be $2.18\mu_B$, which is in good agreement with the experimental value of $2.13 \mu_B$.

6.3 Magnetic Anisotropy

Magnetic anisotropy is the dependence of a material's total energy on the orientation of the atomic magnetic moments. The primary cause of magnetic anisotropy is the spin-orbit coupling (SOC). This interaction connects the spin and orbital degrees of freedom, as a result, the non-spherical charge distribution in a material causes the atomic spins have preferred orientations. The second source of magnetic anisotropy is the magnetic dipole-dipole interaction. In bulk crystals this interaction is usually very small, and vanishes for crystals with cubic symmetry. For finite size systems, however, the dipole-dipole interaction can also be important.

The most important application of magnetic anisotropy is on information storage. For example, in hard disk drives, materials with large magnetic anisotropy per volume, K , are used for recording layers. For materials with uniaxial magnetic anisotropy, expression of the magnetic anisotropy energy (MAE) can be approximately written as

$$E_{MA} = KV \sin^2 \theta, \quad (6.4)$$

where V is the grain size and θ is the angle between the magnetization and the normal axis. The two stable states can then be used to represent the "0" and "1" states in

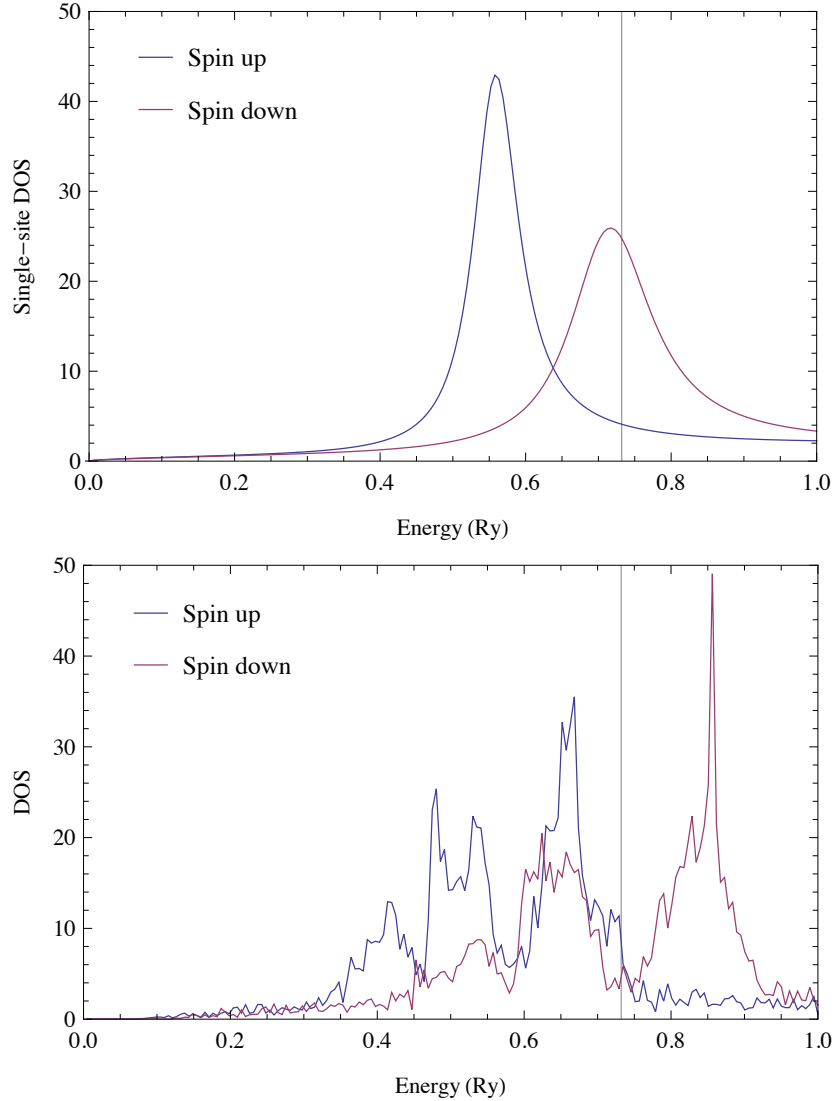


Figure 6.1: The single-site DOS and total DOS of BCC Fe. Imaginary part of the energies in the Green function are taken as 0.001 Ry to show the DOS. The Fermi energy is marked by a vertical line.

hard disks. When writing information into the disk, an energy barrier of KV need to be overcome for each flipping operation. For the stored information to be stable against thermal fluctuation for 10 years, this energy barrier generally need to be larger than $45k_B T$ [13]. Therefore, to increase the storage density of the hard disk, materials with high values of K are preferred.

Other than hard disk drive, another important application of magnetic anisotropy is on magnetoresistive random access memory (MRAM). MRAM is a very promising

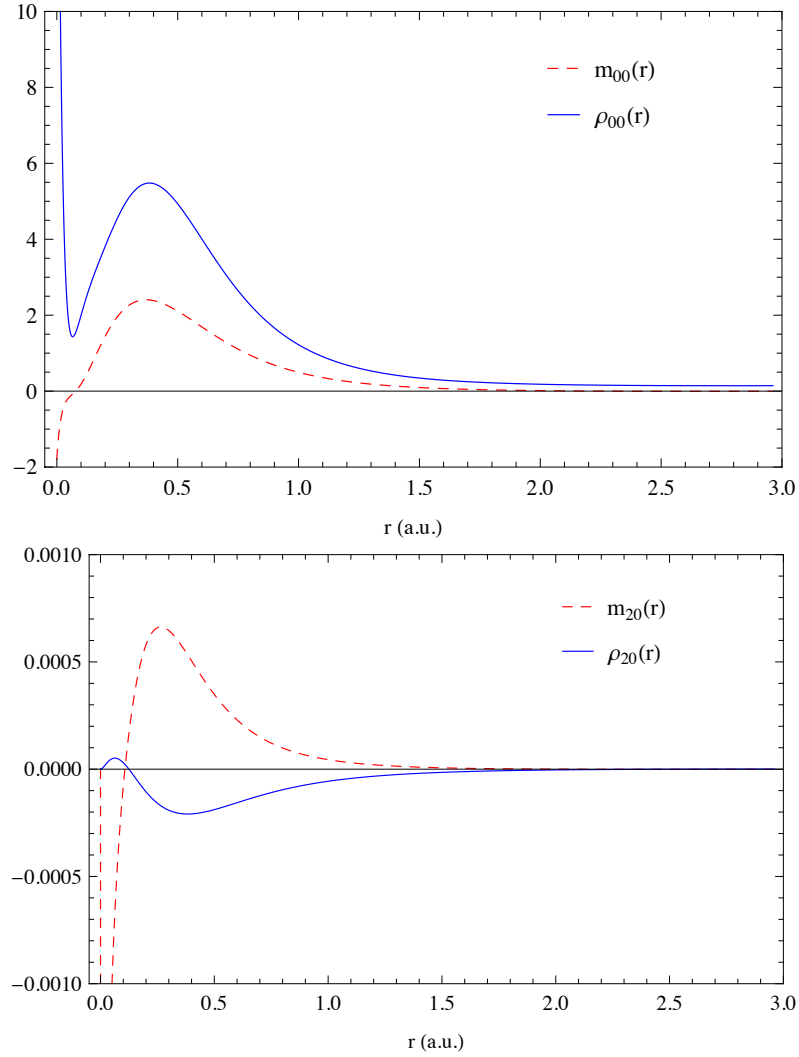


Figure 6.2: The $l, m = (0, 0)$ and $l, m = (2, 0)$ components of the charge density and magnetization of BCC Fe. Calculations are made with relativistic MST.

technology that has the potential of replacing the traditional dynamic random access memory (DRAM). The storage component of MRAM is magnetic tunnel junction (MTJ), which is made of two layers of magnetic metals and a layer of insulator in between. The tunneling current between the two ferromagnetic layers strongly depends on their relative orientation of the magnetization, therefore the parallel and antiparallel configurations can be used to store the two different states of binary data. Similar to a hard disk drive, the MAE of the ferromagnetic layer in MRAM needs to be increased for the size of the storage cell to decrease. By using a more recent technique called spin

transfer torque (STT), flipping orientation of the magnetization will be easier and more energy efficient than the traditional practice of using magnetic field. Together with the high magnetic anisotropy, size of the storage cell in STT-MRAM can be scaled down to less than 16 nm [13].

6.4 First Principles Calculation of the MAE

Because magnetic anisotropy is originated from the weak spin-orbit coupling, its magnitude is usually very small. For bulk materials with cubic symmetry, such as BCC Fe and FCC Ni, the MAE are in the order of μeV . For such a small quantity, the direct method of taking the difference of the total energies with different spin orientations is usually unfeasible. Instead, the difference of the much smaller band energies is almost always taken to obtain the MAE, with the help of the magnetic force theorem. Even so, for k-space methods such as FLAPW, calculating the MAE of BCC Fe [47] still requires a large number of k-points or special numerical techniques, such as the state-tracking method [104] or the torque method [105]. On the other hand, sometimes working in the real space makes the calculation much easier, as demonstrated in reference [106] and [107].

Compared to bulk materials, the ultrathin films exhibit larger MAE (in the order of meV/atom) due to the reduced symmetry of charge distribution, therefore are of greater interest to the development of the next-generation storage devices. Since the SOC generally increases for element with larger atomic number, people first study multilayers with heavy elements, such as Pd, Au and Pt, to obtain materials with large MAE. For example, in 2003, Gambardella *et al.* [108] found that single Co atoms on Pt (111) surface have MAE as large as 9 meV/atom. However, an important problem for the Co/Pt base multilayers is that they have large Gilbert damping constant, therefore require high switching current. This problem is avoided in the CoFeB–MgO magnetic tunnel junction [109], which demonstrates attractive features including low Gilbert damping constant, high tunnel magnetoresistance ratio and relatively large perpendicular MAE. The perpendicular MAE is important because it allows for higher storage densities than in-plane MAE. For the development of STT-MRAM beyond the 16 nm node, the perpendicular MAE CoFeB–MgO still needs to be increased. Possible methods to achieve higher MAE including trying different materials for the capping and buffer layers [13], or doping the Ta buffer layer with nitrogen [110].

Even for ultrathin films, the MAE is still a small quantity and one must be very careful with the approximations used in first principles calculation, such as choice of the exchange-correlation functional, relaxation of the crystal structure, and treatment of the substrate. Detailed assessment of all these factors has been given in reference [111,112].

6.5 Iron Monolayer

In this section, we use a free-standing Fe monolayer as an example to demonstrate the calculation of MAE with relativistic MST. First principles calculations of the MAE of Fe monolayer have been made with various methods in literature, therefore it is easy for us to compare the results. At first sight, Fe monolayer seems not exist in nature because electrons in metals are delocalized and usually can not support free-standing two dimensional structure. However, in a recent study [113], it has been observed to exist across the pores in a graphene sheet.

Table 6.1: The MAE (meV/atom) of Fe monolayer calculated with different methods. Lattice constant $a=4.83$ in all cases.

| Relativistic MST | Torque method (Ref. [105]) | State tracking (Ref. [105]) |
|------------------|----------------------------|-----------------------------|
| 0.28 | 0.21 | 0.24 |

In our calculation, 4096 k-points are used and a unit cell made up of three layers of vacuum and one layer of square lattice Fe atoms is adopted. The lattice constant is 4.83 a.u. and the distance between neighboring Fe layers is 9.66 a.u. (vacuum sites and Fe sites forms BCC structure). To model realistic Fe monolayer, more vacuum layers should be used, but as will be seen, our system is already good enough to reproduce most of the magnetic properties of Fe monolayer. Using the magnetic force theorem, the MAE is calculated by comparing the difference of the band energy

$$\text{MAE} = E_{band}(\theta = \pi/2) - E_{band}(\theta = 0), \quad (6.5)$$

and the band energy E_{band} is given by

$$E_{band} = \int_{E_b}^{E_F} E n(E) dE, \quad (6.6)$$

where $n(E)$ is the DOS of valence electrons. The MAE calculated with our method is

0.28 meV/atom and comparison with the values from other methods are shown in table 6.1 and the agreement is good for such a small value. To demonstrate the θ dependence, the MAE vs $\sin^2(\theta)$ curve is plotted as shown in figure 6.3. The smoothness of the data points indicates that our calculation is reliable.

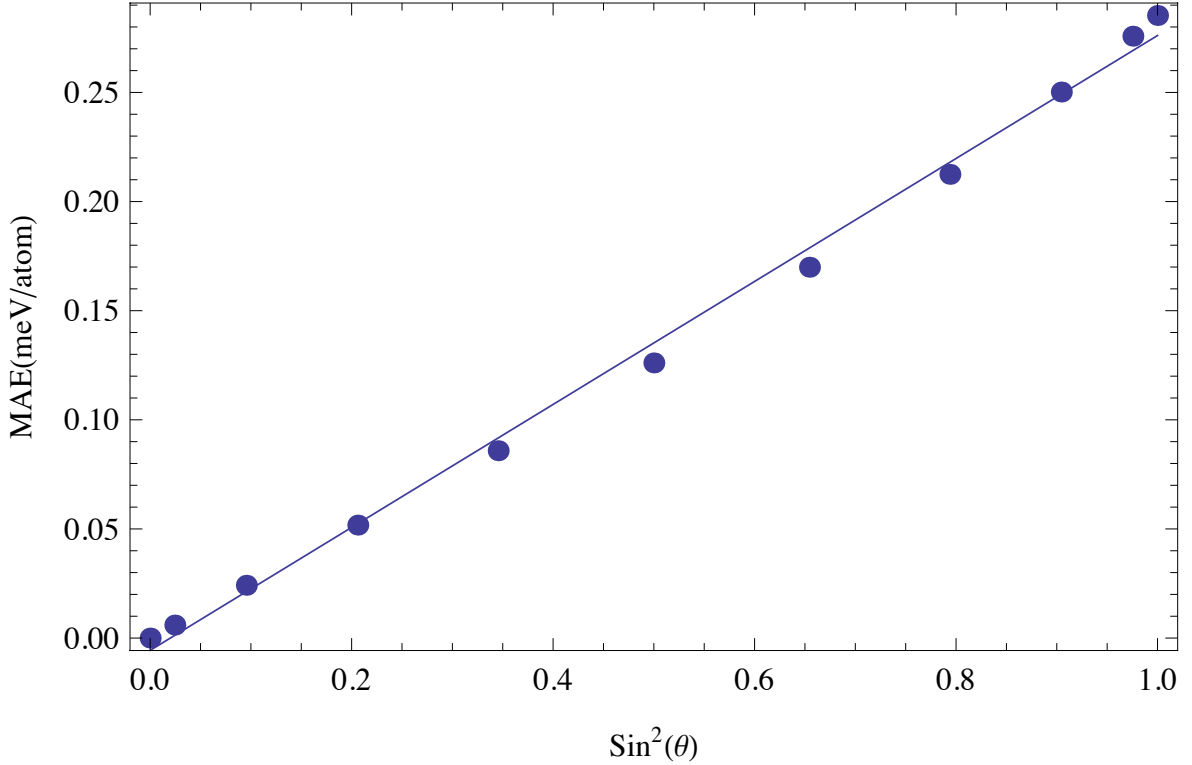


Figure 6.3: Calculated MAE vs $\sin^2(\theta)$ for an Fe monolayer with $a=4.83$ a.u.. The dots are the calculated values and the straight line is the fitted $-0.005 + 0.282x$ curve.

6.6 Conclusion and Outlook

In this chapter, we calculated the DOS, charge density and magnetization of BCC Fe using fully relativistic MST. Compared to the non-relativistic calculation, a major difference of the relativistic result is that the charge density and magnetization have non-vanishing $l, m = (2, 0)$ components. Using the Fe monolayer as an example, we demonstrated the calculation of magnetic anisotropy using fully relativistic MST. The obtained energy vs θ data points fit excellently with a $\sin^2(\theta)$ curve.

Our calculation of the MAE is a preliminary study to investigate the MAE of real MTJ systems. Previous first principles calculations of the MAE mainly focus on the

Fe(Co)|MgO interfaces [114–116] because most commercial DFT packages can only treat relatively small systems, especially for MAE calculations where large amounts of k-points are required. By combining the fully-relativistic MST solver with the LSMS code in our group, we will be able to study MTJ systems that are composed of thin films with thickness of a few nanometers. This will not only give a more realistic description of the multilayer system, but also allow for investigating factors such as concentration, doping, capping and buffer layers, therefore shed light on the optimization of MTJ.

Appendix A

Conventions and Units

Throughout this thesis we use the atomic Rydberg units. This notation starts from the definition that:

$$\hbar = 2m = \frac{1}{2} \frac{e^2}{4\pi\epsilon_0} = 1, \quad (\text{A.1})$$

where m is the mass of electron and e is elementary charge, and

$$\alpha = \frac{e^2}{4\pi\epsilon_0\hbar c} \approx \frac{1}{137}. \quad (\text{A.2})$$

From the above definitions it is easy to see that

$$c = \frac{2}{\alpha} \approx 274. \quad (\text{A.3})$$

In most chapters of this thesis, values of m, e, \hbar are directly used to simplify the expression. For example, in non-relativistic case, momentum is written in terms of kinetic energy as $p = \sqrt{E}$, instead of $p = \sqrt{2mE}$. The only exception is chapter 2, in which the letters are retained for the sake of dimension analysis.

Other units can be derived from the above definitions. The Bohr radius is given by

$$a_0 = \frac{\hbar^2}{me^2} = 1, \quad (\text{A.4})$$

therefore it is used as the unit of length. The Rydberg energy is given by

$$E_{\text{Ry}} = \frac{1}{2} \frac{e^2}{4\pi\epsilon_0 a_0} = 1, \quad (\text{A.5})$$

and is used as the unit of energy.

Appendix B

Derivation of the Regular Solution

$\psi(\mathbf{r})$

In this appendix we show how the expression in equation (4.10) is obtained. The free-space Green's function $G_0(E, \mathbf{r}, \mathbf{r}')$ of the Dirac equation can be expressed in terms of the free-space solutions,

$$\begin{aligned} G_0(E, \mathbf{r}, \mathbf{r}') &= -ip \sum_{\Lambda} J_{\Lambda}(E, \mathbf{r}) H_{\Lambda}^+(E, \mathbf{r}') \Theta(\mathbf{r}' - \mathbf{r}) \\ &\quad - ip \sum_{\Lambda} H_{\Lambda}(E, \mathbf{r}) J_{\Lambda}^+(E, \mathbf{r}') \Theta(\mathbf{r} - \mathbf{r}'). \end{aligned} \quad (\text{B.1})$$

The solutions of the Dirac equation can be written in terms of the free-space Green's function $G_0(E, \mathbf{r}, \mathbf{r}')$ and the free-space solutions $\phi(\mathbf{r})$:

$$\psi(E, \mathbf{r}) = \phi(E, \mathbf{r}) + \int_{\Omega} d^3\mathbf{r}' G_0(E, \mathbf{r}, \mathbf{r}') V(\mathbf{r}') \psi(E, \mathbf{r}'). \quad (\text{B.2})$$

We have the freedom of choosing $\phi(\mathbf{r})$. Here our choice is:

$$\phi(E, \mathbf{r}) = \sum_{\Lambda'} J_{\Lambda'}(E, \mathbf{r}) \{iS_{\Lambda'\Lambda}(E) - C_{\Lambda'\Lambda}(E)\}, \quad (\text{B.3})$$

where

$$C_{\Lambda'\Lambda}(E) = p \int_{\Omega} d^3\mathbf{r}' N_{\Lambda'}^+(E, \mathbf{r}') V(\mathbf{r}') \psi_{\Lambda}(E, \mathbf{r}') - \delta_{\Lambda'\Lambda} \quad (\text{B.4})$$

$$S_{\Lambda'\Lambda}(E) = p \int_{\Omega} d^3\mathbf{r}' J_{\Lambda'}^+(E, \mathbf{r}') V(\mathbf{r}') \psi_{\Lambda}(E, \mathbf{r}'). \quad (\text{B.5})$$

equation (B.2) becomes

$$\begin{aligned} \psi_{\Lambda}(E, \mathbf{r}) = & \sum_{\Lambda'} \{iS_{\Lambda'\Lambda}(E) - C_{\Lambda\Lambda'}(E)\} J_{\Lambda'}(E, \mathbf{r}) + \\ & \int_{\Omega} d^3\mathbf{r}' G_0(E, \mathbf{r}, \mathbf{r}') V(\mathbf{r}') \psi_{\Lambda}(E, \mathbf{r}'). \end{aligned} \quad (\text{B.6})$$

Next we plug the free-space Green's function expression equation (B.1) back into equation (B.6) and split the integral region into two pieces according to $r' > r$ or $r' < r$, we have

$$\begin{aligned} \text{Eq. (B.6)} = & \sum_{\Lambda'} \{iS_{\Lambda'\Lambda}(E) - C_{\Lambda\Lambda'}(E)\} J_{\Lambda'}(E, \mathbf{r}) \\ & - i \sum_{\Lambda'} S_{\Lambda'\Lambda}(E, r) \{J_{\Lambda'}(E, \mathbf{r}) + iN_{\Lambda'}(E, \mathbf{r})\} \\ & - iJ_{\Lambda'}(E, \mathbf{r}) \int_{r < r' \in \Omega} d^3\mathbf{r}' \{J_{\Lambda'}^+(E, \mathbf{r}') + iN_{\Lambda'}^+(E, \mathbf{r}')\} V(\mathbf{r}') \psi_{\Lambda}(E, \mathbf{r}'). \end{aligned} \quad (\text{B.7})$$

Using the short-hand notation that $J = J_{\Lambda'}(E, \mathbf{r})$, $N = N_{\Lambda'}(E, \mathbf{r})$,

$$\begin{aligned} C_{<} = & p \int_{0 < r' < r} d^3\mathbf{r}' N_{\Lambda'}^+(E, \mathbf{r}') V(\mathbf{r}') \psi_{\Lambda}(E, \mathbf{r}'), \\ C_{>} = & p \int_{r < r' \in \Omega} d^3\mathbf{r}' N_{\Lambda'}^+(E, \mathbf{r}') V(\mathbf{r}') \psi_{\Lambda}(E, \mathbf{r}'), \end{aligned} \quad (\text{B.8})$$

and

$$C = C_{<} + C_{>} = C_{\Lambda\Lambda'}(E) + \delta_{\Lambda\Lambda'}, \quad (\text{B.9})$$

and similar notation for the sine matrices, we have

$$\begin{aligned} \text{Eq.(B.7)} &= iJS - (JC - J) - i(J + iN)S_{<} + JC_{>} - iJS_{>} \\ &= NS_{<} - (JC_{<} - J), \end{aligned} \quad (\text{B.10})$$

which is exactly equation (4.10). i.e.

$$\psi_{\Lambda}(E, \mathbf{r}) = \sum_{\Lambda'} \{S_{\Lambda'\Lambda}(E, r)N_{\Lambda'}(E, \mathbf{r}) - C_{\Lambda'\Lambda}(E, r)J_{\Lambda'}(E, \mathbf{r})\}. \quad (\text{B.11})$$

Appendix C

Derivation of the Green Function

In this appendix we show how to derive the expression of Green's function in equation (5.4). The general expression of Green's function can be written in terms of regular solutions $P_\Lambda(E, \mathbf{r})$ and irregular solutions $Q_\Lambda(E, \mathbf{r})$ as

$$G(E, \mathbf{r}, \mathbf{r}') = -ip \sum_{\Lambda} P_\Lambda(E, \mathbf{r}) Q_\Lambda^+(E, \mathbf{r}') \Theta(\mathbf{r}' - \mathbf{r}) - ip \sum_{\Lambda} Q_\Lambda(E, \mathbf{r}) P_\Lambda^+(E, \mathbf{r}') \Theta(\mathbf{r} - \mathbf{r}'). \quad (\text{C.1})$$

We have obtained regular solutions $\psi_\Lambda(E, \mathbf{r})$. To find the appropriate irregular solutions to construct the Green's function, we start with the definition of the Green's function

$$[-c\boldsymbol{\alpha}i\nabla + \beta mc^2 + V(\mathbf{r}) - W] G(E, \mathbf{r}, \mathbf{r}') = -\delta(\mathbf{r} - \mathbf{r}'). \quad (\text{C.2})$$

Simplifying the above expression, we find

$$(-i) \oint_{r=R_2} d\mathbf{s} \cdot \mathbf{W}[P_\Lambda^+(E, \mathbf{r}), Q_{\Lambda'}(E, \mathbf{r})] = \delta_{\Lambda\Lambda'}, \quad (\text{C.3})$$

where $\mathbf{W}[\dots]$ is the relativistic Wronskian

$$\mathbf{W}[\psi_1^+(E, \mathbf{r}), \psi_2(E, \mathbf{r})] = icp\psi_1^+(E, \mathbf{r})\boldsymbol{\alpha}\psi_2(E, \mathbf{r}). \quad (\text{C.4})$$

The following Wronskian relations satisfied by the free-space solutions can be verified by plugging in equation (4.2), (4.3), (4.8) and (4.9),

$$\oint_{r'=r} ds' \mathbf{W}[J_{\Lambda}^{+}(E, \mathbf{r}'), N_{\Lambda'}(E, \mathbf{r}')] = \delta_{\Lambda\Lambda'}, \quad (\text{C.5})$$

$$\oint_{r'=r} ds' \mathbf{W}[J_{\Lambda}^{+}(E, \mathbf{r}'), J_{\Lambda'}(E, \mathbf{r}')] = 0, \quad (\text{C.6})$$

$$\oint_{r'=r} ds' \mathbf{W}[N_{\Lambda}^{+}(E, \mathbf{r}'), N_{\Lambda'}(E, \mathbf{r}')] = 0. \quad (\text{C.7})$$

For a given regular solution, equation (C.3) is the relation the irregular solution needs to satisfy to construct the Green's function in equation (C.1). To obtain an explicit expression of $Q_{\Lambda}(E, \mathbf{r})$, we make use of the integral equation satisfied by the Green's functions

$$G(E, \mathbf{r}, \mathbf{r}') = G_0(E, \mathbf{r}, \mathbf{r}') + \int_{\Omega} d^3\mathbf{r}'' G_0(E, \mathbf{r}, \mathbf{r}'') V(\mathbf{r}'') G(E, \mathbf{r}'', \mathbf{r}'). \quad (\text{C.8})$$

Plugging in equation (C.1) and equation (B.1) and using the Dirac equations, it can be shown that the explicit expression of the irregular solution is given by

$$Q_{\Lambda}^{+}(E, \mathbf{r}) = \sum_{\Lambda'} [A_{\Lambda\Lambda'}^{-1}(E)] \mathcal{H}_{\Lambda'}^{+}(E, \mathbf{r}), \quad (\text{C.9})$$

where $\mathcal{H}_{\Lambda}^{+}(\mathbf{r}')$ have similar definition as $\mathcal{J}_{\Lambda}^{+}(E, \mathbf{r}')$, with the boundary conditions $\mathcal{H}_{\Lambda}^{+}(E, \mathbf{r}) = H_{\Lambda}^{+}(E, \mathbf{r})$ outside the Wigner-Seitz cell, and

$$A_{\Lambda'\Lambda}(E) = -i \oint_{B_{\Omega}} ds'' \cdot \mathbf{W}[\mathcal{H}_{\Lambda}^{+}(E, \mathbf{r}''), P_{\Lambda}(E, \mathbf{r}'')]. \quad (\text{C.10})$$

If we plug in equation (4.10) and the relativistic Wronskian relations satisfied by the free space solutions, we can find the corresponding irregular solution to construct the Green's function to be

$$Q_{\Lambda}^{+}(E, \mathbf{r}) = \sum_{\Lambda'} [iS_{\Lambda'\Lambda}(E) - C_{\Lambda'\Lambda}(E)]^{-1} \mathcal{H}_{\Lambda'}^{+}(E, \mathbf{r}). \quad (\text{C.11})$$

Therefore, for $r' > r$ the Green's function is given by the expression

$$G(E, \mathbf{r}, \mathbf{r}') = -ip \sum_{\Lambda\Lambda'} \psi_{\Lambda}(E, \mathbf{r}) [iS_{\Lambda'\Lambda}(E) - C_{\Lambda'\Lambda}(E)]^{-1} \mathcal{H}_{\Lambda'}^+(E, \mathbf{r}'). \quad (\text{C.12})$$

To obtain a more familiar expression, we use the relation satisfied by the T -operator

$$\langle J_{\Lambda}^+(E, \mathbf{r}) | \hat{V} | \psi_{\Lambda'}(E, \mathbf{r}) \rangle = \langle J_{\Lambda}^+(E, \mathbf{r}) | \hat{T} | \phi_{\Lambda'}(E, \mathbf{r}) \rangle. \quad (\text{C.13})$$

Plugging in equation (B.3) and (4.10), it's easy to show that the t matrix is given by

$$t_{\Lambda\Lambda'}(E)^{-1} = p \left(i\delta_{\Lambda\Lambda'} - \sum_{\Lambda''} C_{\Lambda\Lambda''}(E) S_{\Lambda''\Lambda'}^{-1}(E) \right). \quad (\text{C.14})$$

Using the definition of $Z_{\Lambda}(E, \mathbf{r})$ in equation (4.27), we obtain the useful expression

$$G(E, \mathbf{r}, \mathbf{r}') = -ip \sum_{\Lambda\Lambda'} Z_{\Lambda}(E, \mathbf{r}) t_{\Lambda\Lambda'}(E) \mathcal{H}_{\Lambda'}^+(E, \mathbf{r}') \quad (\text{C.15})$$

$$= \sum_{\Lambda\Lambda'} Z_{\Lambda}(E, \mathbf{r}) t_{\Lambda\Lambda'}(E) Z_{\Lambda'}^+(E, \mathbf{r}') - \sum_{\Lambda} Z_{\Lambda}(E, \mathbf{r}) \mathcal{J}_{\Lambda}^+(E, \mathbf{r}'). \quad (\text{C.16})$$

In the second line, we used the relation

$$Z_{\Lambda'}^+(E, \mathbf{r}) = \sum_{\Lambda''} [t_{\Lambda'\Lambda''}(E)^{-1}]^+ \mathcal{J}_{\Lambda''}^+(E, \mathbf{r}) - ip \mathcal{H}_{\Lambda'}^+(E, \mathbf{r}), \quad (\text{C.17})$$

and the fact that

$$[t_{\Lambda'\Lambda''}(E)]^+ = [t_{\Lambda'\Lambda''}(E)]^T, \quad (\text{C.18})$$

which can be proved using relativistic Wronskians by analogy with the non-relativistic case [57].

Because both the potential and the energies are real, from equation (4.18-4.23), we see that for our calculation $S_{\Lambda'\Lambda}(E, r)$ and $C_{\Lambda'\Lambda}(E, r)$ are also real, from the Dirac equation satisfied by the left-hand solutions, we have

$$\psi_{\Lambda}^+(E, \mathbf{r}) = \sum_{\Lambda'} \{ N_{\Lambda'}^+(E, \mathbf{r}) [S_{\Lambda'\Lambda}(E, r)]^T - J_{\Lambda'}^+(E, \mathbf{r}) [C_{\Lambda'\Lambda}(E, r)]^T \}, \quad (\text{C.19})$$

and

$$Z_{\Lambda}^{+}(E, \mathbf{r}) = p \sum_{\Lambda'} \psi_{\Lambda'}^{+}(E, \mathbf{r}) [S_{\Lambda'\Lambda}^{-1}(E)]^T. \quad (\text{C.20})$$

The “ T ” superscript indicates taking the transpose. Note that in general the left-hand solutions and the right-hand solutions do not have such a simple relation, i.e., we cannot obtain $[S_{\Lambda'\Lambda}(E, r)]^{+}$ by simply taking the transpose of $S_{\Lambda'\Lambda}(E, r)$. Particularly, when a non-Hermitian self-energy $\Sigma(z)$ term, or the y direction Pauli matrix, σ_y , is included in the Hamiltonian, we may need to solve the left-hand and right-hand solutions individually. Details of the distinction between right-hand and left-hand solutions at a general potential have been discussed in a recent paper [21].

Appendix D

Solving the Dirac Equation in Muffin-Tin Potential

As an example to illustrate our approach of solving the Dirac equation, here we present the numerical details in the simplified case of muffin-tin potential, with magnetic field included. The electric potential part of $a_{\Lambda'\Lambda}$ will be reduced into

$$a_{\Lambda'}^v(r) = p \frac{(W + \frac{1}{2}c^2)}{c^2} r^2 j_{\nu'}(pr) n_{\nu'}(pr) v(r) + p(W - \frac{1}{2}c^2) r^2 j_{\bar{\nu}'}(pr) n_{\bar{\nu}'}(pr) v(r). \quad (\text{D.1})$$

The magnetic field part will be a little more complicated. Let's assume that the magnetic field is in the z direction. As will be explained below, for MT potential, $a_{\Lambda''\Lambda'}^B(r)$ are nonzero in three cases. The expression of $a_{\Lambda''\Lambda'}^B(r)$ is given by:

$$a_{\Lambda''\Lambda'}^B(r) = p \frac{(W + \frac{1}{2}c^2)}{c^2} r^2 j_{\nu'}(pr) n_{\nu''}(pr) \sum_{l_B} B_{L_B}(r) \langle \chi_{\Lambda'}^\dagger(\hat{\mathbf{r}}) | \sigma_z Y_{L_B}(\hat{\mathbf{r}}) | \chi_{\Lambda''}(\hat{\mathbf{r}}) \rangle - p \frac{(W - \frac{1}{2}c^2)}{c^2} r^2 j_{\bar{\nu}'}(pr) n_{\bar{\nu}''}(pr) \sum_{l_B} B_{L_B}(r) \langle \chi_{\Lambda'}^\dagger(\hat{\mathbf{r}}) | \sigma_z Y_{L_B}(\hat{\mathbf{r}}) | \chi_{\Lambda''}(\hat{\mathbf{r}}) \rangle. \quad (\text{D.2})$$

Note that for any term to survive, $m_{j'} = m_{j''}$ (or equivalently $\mu' = \mu''$) has to be true, else there are either $m_{\nu'} = m_{\nu''}$ or $m_{s'} = m_{s''}$, both render the inner product above vanishing. The first nonvanishing case is $\kappa'' = \kappa'$. In this case, both the two terms in

Eq.(D.2) remain and we have

$$\begin{aligned}
a_1^B(r) = & p \frac{(W + \frac{1}{2}c^2)}{c^2} r^2 j_{l'}(pr) n_{l'}(pr) \{ C(l', j', \frac{1}{2}|\mu' - \frac{1}{2}, \frac{1}{2}) C(l', j', \frac{1}{2}|\mu' - \frac{1}{2}, \frac{1}{2}) - \\
& C(l', j', \frac{1}{2}|\mu' + \frac{1}{2}, -\frac{1}{2}) C(l', j', \frac{1}{2}|\mu' + \frac{1}{2}, -\frac{1}{2}) \}, \\
& - p \frac{(W - \frac{1}{2}c^2)}{c^2} r^2 j_{\bar{l}'}(pr) n_{\bar{l}'}(pr) \{ C(\bar{l}', j', \frac{1}{2}|\mu' - \frac{1}{2}, \frac{1}{2}) C(\bar{l}', j', \frac{1}{2}|\mu' - \frac{1}{2}, \frac{1}{2}) - \\
& C(\bar{l}', j', \frac{1}{2}|\mu' + \frac{1}{2}, -\frac{1}{2}) C(\bar{l}', j', \frac{1}{2}|\mu' + \frac{1}{2}, -\frac{1}{2}) \}. \tag{D.3}
\end{aligned}$$

The second case is $\kappa'' = -\kappa' - 1$, now the second term in Eq.(D.2) vanishes and only the first term survives,

$$\begin{aligned}
a_2^B(r) = & p \frac{(W + \frac{1}{2}c^2)}{c^2} r^2 j_{l'}(pr) n_{l'}(pr) \{ C(l', j', \frac{1}{2}|\mu' - \frac{1}{2}, \frac{1}{2}) C(l', j'', \frac{1}{2}|\mu' - \frac{1}{2}, \frac{1}{2}) - \\
& C(l', j', \frac{1}{2}|\mu' + \frac{1}{2}, -\frac{1}{2}) C(l', j'', \frac{1}{2}|\mu' + \frac{1}{2}, -\frac{1}{2}) \}. \tag{D.4}
\end{aligned}$$

Note that in the above expression, if $j' = l - 1/2$, then $j'' = l + 1/2$, and vice versa.

The third case is $\kappa'' = -\kappa'$, now the first term in Eq.(D.2) vanishes and only the second one remains,

$$\begin{aligned}
a_3^B(r) = & - p \frac{(W - \frac{1}{2}c^2)}{c^2} r^2 j_{\bar{l}'}(pr) n_{\bar{l}'}(pr) \{ C(\bar{l}', j', \frac{1}{2}|\mu' - \frac{1}{2}, \frac{1}{2}) C(\bar{l}', j'', \frac{1}{2}|\mu' - \frac{1}{2}, \frac{1}{2}) - \\
& C(\bar{l}', j', \frac{1}{2}|\mu' + \frac{1}{2}, -\frac{1}{2}) C(\bar{l}', j'', \frac{1}{2}|\mu' + \frac{1}{2}, -\frac{1}{2}) \}. \tag{D.5}
\end{aligned}$$

As in the second case, when $j' = l - 1/2$, we have $j'' = l + 1/2$, and vice versa. For the more general cases that the magnetic field has x and y components, similar expression can be derived, but note that when the magnetic field has nonzero y component, extra-caution must be paid to the difference of the left and right solutions, as mentioned in Appendix C.

The differential equations are solved on exponential radial grid $r = r_0 \exp(x)$, so

$$\frac{d}{dx} = \frac{d}{dr} r. \tag{D.6}$$

This introduced a r factor into the differential equations, but if we redefine the potential

as

$$V^{new}(\mathbf{r}) = rV(\mathbf{r}), \quad (\text{D.7})$$

then the differential equations with respect to x will be the same as Eq. (4.13,4.14) except for the replacement of $V(\mathbf{r})$ by $V^{new}(\mathbf{r})$. In practice, the first few points of the differential equations are solved with Runge-Kutta method, then the predictor-corrector method will be used. For simplicity, we can write the differential equations (4.13,4.14) as

$$\frac{d}{dx}s_{\Lambda''\Lambda'}(r) = f_{\Lambda''\Lambda'}(r, s_{\Lambda''\Lambda'}, c_{\Lambda''\Lambda'}) \quad (\text{D.8})$$

$$\frac{d}{dx}c_{\Lambda''\Lambda'}(r) = g_{\Lambda''\Lambda'}(r, s_{\Lambda''\Lambda'}, c_{\Lambda''\Lambda'}), \quad (\text{D.9})$$

where r is implicitly a function of x . All the nonzero matrix elements of $f_{\Lambda''\Lambda'}$ or $g_{\Lambda''\Lambda'}$ for $l \leq 2$ are shown in figure(D.1). To use the 4-th order Runge-Kutta method, we need

$$K_1 = f(r^n, s_{\Lambda''\Lambda'}^n, c_{\Lambda''\Lambda'}^n)\Delta x \quad (\text{D.10})$$

$$L_1 = g(r^n, s_{\Lambda''\Lambda'}^n, c_{\Lambda''\Lambda'}^n)\Delta x \quad (\text{D.11})$$

$$K_2 = f(r^n + \Delta x/2, s_{\Lambda''\Lambda'}^n + K_1/2, c_{\Lambda''\Lambda'}^n + L_1/2)\Delta x \quad (\text{D.12})$$

$$L_2 = g(r^n + \Delta x/2, s_{\Lambda''\Lambda'}^n + K_1/2, c_{\Lambda''\Lambda'}^n + L_1/2)\Delta x \quad (\text{D.13})$$

$$K_3 = f(r^n + \Delta x/2, s_{\Lambda''\Lambda'}^n + K_2/2, c_{\Lambda''\Lambda'}^n + L_2/2)\Delta x \quad (\text{D.14})$$

$$L_3 = g(r^n + \Delta x/2, s_{\Lambda''\Lambda'}^n + K_2/2, c_{\Lambda''\Lambda'}^n + L_2/2)\Delta x \quad (\text{D.15})$$

$$K_4 = f(r^n + \Delta x, s_{\Lambda''\Lambda'}^n + K_3, c_{\Lambda''\Lambda'}^n + L_3)\Delta x \quad (\text{D.16})$$

$$L_4 = g(r^n + \Delta x, s_{\Lambda''\Lambda'}^n + K_3, c_{\Lambda''\Lambda'}^n + L_3)\Delta x, \quad (\text{D.17})$$

and

$$s_{\Lambda''\Lambda'}^{n+1} = s_{\Lambda''\Lambda'}^n + \frac{K_1 + 2K_2 + 2K_3 + K_4}{6}, \quad (\text{D.18})$$

$$c_{\Lambda''\Lambda'}^{n+1} = c_{\Lambda''\Lambda'}^n + \frac{L_1 + 2L_2 + 2L_3 + L_4}{6}. \quad (\text{D.19})$$

Once the first few points have been obtained with Runge-Kutta method, the predictor-corrector method is used. For the predictor, the 4-th order Adams-Bashforth formula

is used,

$$s_{\Lambda''\Lambda'}(r_n) = s_{\Lambda''\Lambda'}(r_{n-1}) + \frac{\Delta x}{24} [55f_{\Lambda''\Lambda'}(r_{n-1}) - 59f_{\Lambda''\Lambda'}(r_{n-2}) \\ + 37f_{\Lambda''\Lambda'}(r_{n-3}) - 9f_{\Lambda''\Lambda'}(r_{n-4})], \quad (\text{D.20})$$

$$c_{\Lambda''\Lambda'}(r_n) = c_{\Lambda''\Lambda'}(r_{n-1}) + \frac{\Delta x}{24} [55g_{\Lambda''\Lambda'}(r_{n-1}) - 59g_{\Lambda''\Lambda'}(r_{n-2}) \\ + 37g_{\Lambda''\Lambda'}(r_{n-3}) - 9g_{\Lambda''\Lambda'}(r_{n-4})] \quad (\text{D.21})$$

The 4-th order Adams-Moulton formula is used as corrector,

$$s_{\Lambda''\Lambda'}(r_n) = s_{\Lambda''\Lambda'}(r_{n-1}) + \frac{\Delta x}{24} [9f_{\Lambda''\Lambda'}(r_n) + 19f_{\Lambda''\Lambda'}(r_{n-1}) \\ - 5f_{\Lambda''\Lambda'}(r_{n-2}) + f_{\Lambda''\Lambda'}(r_{n-3})], \quad (\text{D.22})$$

$$c_{\Lambda''\Lambda'}(r_n) = c_{\Lambda''\Lambda'}(r_{n-1}) + \frac{\Delta x}{24} [9g_{\Lambda''\Lambda'}(r_n) + 19g_{\Lambda''\Lambda'}(r_{n-1}) \\ - 5g_{\Lambda''\Lambda'}(r_{n-2}) + g_{\Lambda''\Lambda'}(r_{n-3})]. \quad (\text{D.23})$$

| | $s_{1/2}$ | $p_{1/2}$ | $p_{3/2}$ | $d_{3/2}$ | $d_{5/2}$ |
|-----------|-----------|-----------|-----------|-----------|-----------|
| $s_{1/2}$ | | | | | |
| $p_{1/2}$ | | | | | |
| $p_{3/2}$ | | | | | |
| $d_{3/2}$ | | | | | |
| $d_{5/2}$ | | | | | |

Figure D.1: nonzero matrix elements of $f_{\Lambda'\Lambda}$ and $g_{\Lambda'\Lambda}$ for $l \leq 2$. The blue ones are the diagonal elements, including contributions from $l'' = l'$, $l'' = l' \pm 1$ and $l'' = l' \pm 2$. The green ones only have contribution from $l'' = l' + 1$ and the yellow ones only have $l'' = l' + 2$ element

Bibliography

- [1] S. A. Wolf, D. D. Awschalom, R. A. Buhrman, J. M. Daughton, S. von Molnár, M. L. Roukes, A. Y. Chtchelkanova, and D. M. Treger. Spintronics: A spin-based electronics vision for the future. *Science*, 294(5546):1488–1495, 2001.
- [2] Tatsumi Aoyama, Masashi Hayakawa, Toichiro Kinoshita, and Makiko Nio. Tenth-order electron anomalous magnetic moment: Contribution of diagrams without closed lepton loops. *Phys. Rev. D*, 91:033006, Feb 2015.
- [3] W. Kohn and L. J. Sham. Self-consistent equations including exchange and correlation effects. *Phys. Rev.*, 140:A1133–A1138, 1965.
- [4] J. P. Perdew and Alex Zunger. Self-interaction correction to density-functional approximations for many-electron systems. *Phys. Rev. B*, 23:5048–5079, May 1981.
- [5] John P. Perdew, Kieron Burke, and Matthias Ernzerhof. Generalized gradient approximation made simple. *Phys. Rev. Lett.*, 77:3865–3868, Oct 1996.
- [6] P. W. Anderson. More is different. *Science*, 177(4047):393–396, 1972.
- [7] Steven R. Elliott and Marcel Franz. Colloquium: Majorana fermions in nuclear, particle, and solid-state physics. *Rev. Mod. Phys.*, 87:137–163, Feb 2015.
- [8] B. Q. Lv, H. M. Weng, B. B. Fu, X. P. Wang, H. Miao, J. Ma, P. Richard, X. C. Huang, L. X. Zhao, G. F. Chen, Z. Fang, X. Dai, T. Qian, and H. Ding. Experimental discovery of weyl semimetal taas. *Phys. Rev. X*, 5:031013, Jul 2015.
- [9] S. Mühlbauer, B. Binz, F. Jonietz, C. Pfleiderer, A. Rosch, A. Neubauer, R. Georgii, and P. Böni. Skyrmion lattice in a chiral magnet. *Science*, 323(5916):915–919, 2009.

-
- [10] J Korringa. On the calculation of the energy of a Bloch wave in a metal. *Physica*, 13(6):392 – 400, 1947.
- [11] W. Kohn and N. Rostoker. Solution of the Schrödinger equation in periodic lattices with an application to metallic lithium. *Phys. Rev.*, 94:1111–1120, Jun 1954.
- [12] W. Kohn and L. J. Sham. Self-consistent equations including exchange and correlation effects. *Phys. Rev.*, 140:A1133–A1138, Nov 1965.
- [13] B. Dieny and M. Chshiev. Perpendicular magnetic anisotropy at transition metal/oxide interfaces and applications. *Rev. Mod. Phys.*, 89:025008, Jun 2017.
- [14] A. Manchon, H. C. Koo, J. Nitta, S. M. Frolov, and R. A. Duine. New perspectives for Rashba spin-orbit coupling. *Nature Materials*, 14(9):871–882, Sep 2015.
- [15] D D Koelling and B N Harmon. A technique for relativistic spin-polarised calculations. *Journal of Physics C: Solid State Physics*, 10(16):3107, 1977.
- [16] E. Tamura. Relativistic single-site Green function for general potentials. *Phys. Rev. B*, 45:3271–3278, Feb 1992.
- [17] S C Lovatt, B L Gyorffy, and G Y Guo. Relativistic spin-polarized scattering theory for space-filling potentials. *Journal of Physics: Condensed Matter*, 5(43):8005, 1993.
- [18] Xindong Wang, X.-G. Zhang, W. H. Butler, G. M. Stocks, and B. N. Harmon. Relativistic-multiple-scattering theory for space-filling potentials. *Phys. Rev. B*, 46:9352–9358, Oct 1992.
- [19] T. Huhne, C. Zecha, H. Ebert, P. H. Dederichs, and R. Zeller. Full-potential spin-polarized relativistic Korringa-Kohn-Rostoker method implemented and applied to bcc Fe, fcc Co, and fcc Ni. *Phys. Rev. B*, 58:10236–10247, Oct 1998.
- [20] Matthias Geilhufe, Steven Achilles, Markus Arthur Köbis, Martin Arnold, Ingrid Mertig, Wolfram Hergert, and Arthur Ernst. Numerical solution of the relativistic single-site scattering problem for the Coulomb and the Mathieu potential. *Journal of Physics: Condensed Matter*, 27(43):435202, 2015.

-
- [21] H. Ebert, J. Braun, D. Ködderitzsch, and S. Mankovsky. Fully relativistic multiple scattering calculations for general potentials. *Phys. Rev. B*, 93:075145, Feb 2016.
- [22] R. M. Martin. *Electronic structure: basic theory and practical methods*. Cambridge University Press, 2004.
- [23] Xianglin Liu, Yang Wang, Markus Eisenbach, and G Malcolm Stocks. A full-potential approach to the relativistic single-site Green’s function. *Journal of Physics: Condensed Matter*, 28(35):355501, 2016.
- [24] Xianglin Liu, Yang Wang, Markus Eisenbach, and G Malcolm Stocks. Relativistic full-potential multiple scattering theory: A pathology-free scheme. *Computer Physics Communications*, 2017. Accepted.
- [25] R. O. Jones. Density functional theory: Its origins, rise to prominence, and future. *Rev. Mod. Phys.*, 87:897–923, Aug 2015.
- [26] Marvin L. Cohen. Looking back and ahead at condensed matter physics. *Physics Today*, 59(6):48, 2006.
- [27] P. Hohenberg and W. Kohn. Inhomogeneous electron gas. *Phys. Rev.*, 136:B864–B871, 1964.
- [28] P. Strange. *Relativistic quantum mechanics: with applications in condensed matter and atomic physics*. Cambridge University Press, 1998.
- [29] U von Barth. Basic density-functional theory—an overview. *Physica Scripta*, 2004(T109):9, 2004.
- [30] Anthony Zee. *Quantum field theory in a nutshell*. Princeton University Press, 2010.
- [31] John P. Perdew, Adrienn Ruzsinszky, Jianmin Tao, Viktor N. Staroverov, Gustavo E. Scuseria, and Gábor I. Csonka. Prescription for the design and selection of density functional approximations: More constraint satisfaction with fewer fits. *The Journal of Chemical Physics*, 123(6):062201, 2005.
- [32] Axel D. Becke. A new mixing of Hartree-Fock and local density-functional theories. *The Journal of Chemical Physics*, 98(2):1372, 1993.

-
- [33] P.H. Dederichs, T. Hoshino, B. Drittler, K. Abraham, and R. Zeller. Total-energy calculations for point defects in metals. *Physica B: Condensed Matter*, 172(1):203–209, 1991.
- [34] Paul Soven. Coherent-potential model of substitutional disordered alloys. *Phys. Rev.*, 156:809–813, Apr 1967.
- [35] B. L. Gyorffy. Electronic states in liquid metals: A generalization of the coherent-potential approximation for a system with short-range order. *Phys. Rev. B*, 1:3290–3299, Apr 1970.
- [36] G. M. Stocks, R. W. Williams, and J. S. Faulkner. Densities of states of paramagnetic Cu-Ni alloys. *Phys. Rev. B*, 4:4390–4405, Dec 1971.
- [37] D. D. Johnson, D. M. Nicholson, F. J. Pinski, B. L. Gyorffy, and G. M. Stocks. Density-functional theory for random alloys: Total energy within the coherent-potential approximation. *Phys. Rev. Lett.*, 56:2088–2091, May 1986.
- [38] D. D. Johnson, D. M. Nicholson, F. J. Pinski, B. L. Györffy, and G. M. Stocks. Total-energy and pressure calculations for random substitutional alloys. *Phys. Rev. B*, 41:9701–9716, May 1990.
- [39] B L Gyorffy, A J Pindor, J Staunton, G M Stocks, and H Winter. A first-principles theory of ferromagnetic phase transitions in metals. *Journal of Physics F: Metal Physics*, 15(6):1337, 1985.
- [40] A. Ernst and M. Lüders. *3. Methods for Band Structure Calculations in Solids*. Springer Berlin Heidelberg, Berlin, Heidelberg, 2004.
- [41] J. Minár, L. Chioncel, A. Perlov, H. Ebert, M. I. Katsnelson, and A. I. Lichtenstein. Multiple-scattering formalism for correlated systems: A KKR-DMFT approach. *Phys. Rev. B*, 72:045125, Jul 2005.
- [42] Yang Wang, G. M. Stocks, W. A. Shelton, D. M. C. Nicholson, Z. Szotek, and W. M. Temmerman. Order-N multiple scattering approach to electronic structure calculations. *Phys. Rev. Lett.*, 75:2867–2870, Oct 1995.
- [43] Markus Eisenbach, Jeff Larkin, Justin Lutjens, Steven Rennich, and James H. Rogers. GPU acceleration of the locally selfconsistent multiple scattering code

- for first principles calculation of the ground state and statistical physics of materials. *Computer Physics Communications*, 211:2 – 7, 2017. High Performance Computing for Advanced Modeling and Simulation of Materials.
- [44] J. S. Faulkner and G. M. Stocks. Calculating properties with the coherent-potential approximation. *Phys. Rev. B*, 21:3222–3244, Apr 1980.
- [45] J. S. Faulkner and T. P. Beaulac. Multiple-scattering approach to band theory. ii. fast band theory. *Phys. Rev. B*, 26:1597–1607, Aug 1982.
- [46] W. Kohn. Density functional and density matrix method scaling linearly with the number of atoms. *Phys. Rev. Lett.*, 76:3168–3171, Apr 1996.
- [47] A.J Freeman, Ruqian Wu, Miyoung Kim, and V.I Gavrilenko. Magnetism, magneto-crystalline anisotropy, magnetostriction and MOKE at surfaces and interfaces. *Journal of Magnetism and Magnetic Materials*, 203(1):1 – 5, 1999.
- [48] S. V. Beiden, W. M. Temmerman, Z. Szotek, G. A. Gehring, G. M. Stocks, Yang Wang, D. M. C. Nicholson, W. A. Shelton, and H. Ebert. Real-space approach to the calculation of magnetocrystalline anisotropy in metals. *Phys. Rev. B*, 57:14247–14253, Jun 1998.
- [49] Markus Eisenbach, Balazs L. Györffy, G. Malcolm Stocks, and Balazs Újfalussy. Magnetic anisotropy of monoatomic iron chains embedded in copper. *Phys. Rev. B*, 65:144424, Mar 2002.
- [50] H Ebert, D Ködderitzsch, and J Minár. Calculating condensed matter properties using the KKR-Green’s function method—recent developments and applications. *Reports on Progress in Physics*, 74(9):096501, 2011.
- [51] Rudolf Zeller. Large scale supercell calculations for forces around substitutional defects in NiTi. *physica status solidi (b)*, 251(10):2048–2054, 2014.
- [52] R. Feder, F. Rosicky, and B. Ackermann. Relativistic multiple scattering theory of electrons by ferromagnets. *Zeitschrift für Physik B Condensed Matter*, 52(1):31–36, Mar 1983.
- [53] P Strange, J Staunton, and B L Gyorffy. Relativistic spin-polarised scattering theory-solution of the single-site problem. *Journal of Physics C: Solid State Physics*, 17(19):3355, 1984.

-
- [54] P Strange, H Ebert, J B Staunton, and B L Gyorffy. A relativistic spin-polarised multiple-scattering theory, with applications to the calculation of the electronic structure of condensed matter. *Journal of Physics: Condensed Matter*, 1(18):2959, 1989.
- [55] A C Jenkins and P Strange. Relativistic spin-polarized single-site scattering theory. *Journal of Physics: Condensed Matter*, 6(19):3499, 1994.
- [56] S. Bei der Kellen and A. J. Freeman. Self-consistent relativistic full-potential korringa-kohn-rostoker total-energy method and applications. *Phys. Rev. B*, 54:11187–11198, Oct 1996.
- [57] A. Rusanu, G. M. Stocks, Y. Wang, and J. S. Faulkner. Green’s functions in full-potential multiple-scattering theory. *Phys. Rev. B*, 84:035102, Jul 2011.
- [58] F. Calogero. *Variable Phase Approach to Potential Scattering*. Academic Press, New York, 1967.
- [59] A R Williams and J van W Morgan. Multiple scattering by non-muffin-tin potentials: general formulation. *Journal of Physics C: Solid State Physics*, 7(1):37, 1974.
- [60] A H MacDonald and S H Vosko. A relativistic density functional formalism. *Journal of Physics C: Solid State Physics*, 12(15):2977, 1979.
- [61] M. G. Krein. *Matem. Sborn.*, 33:597, 1953.
- [62] J S Faulkner. Scattering theory and cluster calculations. *Journal of Physics C: Solid State Physics*, 10(23):4661, 1977.
- [63] Yang Wang, G Malcolm Stocks, and J S Faulkner. The single-site Green’s function and Krein’s theorem. *Journal of Physics: Condensed Matter*, 26(27):274208, 2014.
- [64] M. L. Birman and M. G. Krein. *Sov. Math. -Dokl.*, 3:740, 1962.
- [65] L.G. Suttorp and A.J. van Wonderen. Quantized media with absorptive scatterers and modified atomic emission rates. *Optics Communications*, 284(12):2943 – 2948, 2011.

- [66] B. L. Gyorffy, J.B. Staunton, H. Ebert, P. Strange, and B. Ginatempo. *The Effects of Relativity in Atoms, Molecules and the Solid State*. Plenum Press, 1991.
- [67] V M Burke and I P Grant. The effect of relativity on atomic wave functions. *Proceedings of the Physical Society*, 90(2):297, 1967.
- [68] M Ogura and H Akai. The full potential Korringa-Kohn-Rostoker method and its application in electric field gradient calculations. *Journal of Physics: Condensed Matter*, 17(37):5741, 2005.
- [69] Vladimir I. Anisimov, Jan Zaanen, and Ole K. Andersen. Band theory and mott insulators: Hubbard U instead of Stoner I. *Phys. Rev. B*, 44:943–954, Jul 1991.
- [70] M. Lüders, A. Ernst, M. Däne, Z. Szotek, A. Svane, D. Ködderitzsch, W. Hergert, B. L. Györffy, and W. M. Temmerman. Self-interaction correction in multiple scattering theory. *Phys. Rev. B*, 71:205109, May 2005.
- [71] R. Zeller, J. Deutz, and P.H. Dederichs. Application of complex energy integration to selfconsistent electronic structure calculations. *Solid State Communications*, 44(7):993 – 997, 1982.
- [72] J. S. Faulkner, Eva A. Horvath, and D. M. Nicholson. Multiple-scattering theory and the quadratic Korringa-Kohn-Rostoker method. *Phys. Rev. B*, 44:8467–8472, Oct 1991.
- [73] S. A. Rakityansky, S. A. Sofianos, and K. Amos. A method for calculating the Jost function for analytic potentials. *Il Nuovo Cimento B (1971-1996)*, 111(3):363–378, 1996.
- [74] Mao-sheng Miao. Caesium in high oxidation states and as a p-block element. *Nature Chemistry*, 5(10):846–852, Sep 2013.
- [75] Hadrian Djohari, Frederick Milstein, and Dimitrios Maroudas. Stability of simple cubic crystals. *Applied Physics Letters*, 90(16):161910, 2007.
- [76] B. I. Min, J. H. Shim, Min Sik Park, Kyoo Kim, S. K. Kwon, and S. J. Youn. Origin of the stabilized simple-cubic structure in polonium: Spin-orbit interaction versus peierls instability. *Phys. Rev. B*, 73:132102, Apr 2006.

-
- [77] William H. Beamer and Charles R. Maxwell. The crystal structure of polonium. *The Journal of Chemical Physics*, 14(9):569–569, 1946.
- [78] R.J. DeSando and R.C. Lange. The structures of polonium and its compounds- α and β polonium metal. *Journal of Inorganic and Nuclear Chemistry*, 28(9):1837 – 1846, 1966.
- [79] Robert E Kraig, David Roundy, and Marvin L Cohen. A study of the mechanical and structural properties of polonium. *Solid State Communications*, 129(6):411 – 413, 2004.
- [80] Kyoo Kim, Hong Chul Choi, and B. I. Min. Comment on “why is polonium simple cubic and so highly anisotropic?”. *Phys. Rev. Lett.*, 102:079701, Feb 2009.
- [81] Dominik Legut, Martin Friák, and Mojmír Šob. Phase stability, elasticity, and theoretical strength of polonium from first principles. *Phys. Rev. B*, 81:214118, Jun 2010.
- [82] Dominik Legut, Martin Friák, and Mojmír Šob. Why is polonium simple cubic and so highly anisotropic? *Phys. Rev. Lett.*, 99:016402, Jul 2007.
- [83] Chang-Jong Kang, Kyoo Kim, and B. I. Min. Phonon softening and superconductivity triggered by spin-orbit coupling in simple-cubic α -polonium crystals. *Phys. Rev. B*, 86:054115, Aug 2012.
- [84] M. Lach-hab, B. Akdim, D.A. Papaconstantopoulos, M.J. Mehl, and N. Bernstein. Application of the NRL tight-binding method to the heavy elements Pb and Po. *Journal of Physics and Chemistry of Solids*, 65(11):1837 – 1842, 2004.
- [85] A. Rubio-Ponce, J. Morales, and D. Olgúin. *Structural and Electronic Properties of Po under Hydrostatic Pressure*, pages 119–127. Springer Netherlands, Dordrecht, 2012.
- [86] N Papanikolaou, R Zeller, and P H Dederichs. Conceptual improvements of the KKR method. *Journal of Physics: Condensed Matter*, 14(11):2799, 2002.
- [87] A. H. MacDonald, J. M. Daams, S. H. Vosko, and D. D. Koelling. Non-muffin-tin and relativistic interaction effects on the electronic structure of noble metals. *Phys. Rev. B*, 25:713–725, Jan 1982.

- [88] G Panaccione, G Cautero, M Cautero, A Fondacaro, M Grioni, P Lacovig, G Monaco, F Offi, G Paolicelli, M Sacchi, N Stojić, G Stefani, R Tommasini, and P Torelli. High-energy photoemission in silver: resolving d and sp contributions in valence band spectra. *Journal of Physics: Condensed Matter*, 17(17):2671, 2005.
- [89] V. N. Strocov, R. Claessen, G. Nicolay, S. Hüfner, A. Kimura, A. Harasawa, S. Shin, A. Kakizaki, P. O. Nilsson, H. I. Starnberg, and P. Blaha. Absolute band mapping by combined angle-dependent very-low-energy electron diffraction and photoemission: Application to Cu. *Phys. Rev. Lett.*, 81:4943–4946, Nov 1998.
- [90] Andrea Marini, Giovanni Onida, and Rodolfo Del Sole. Quasiparticle electronic structure of copper in the *GW* approximation. *Phys. Rev. Lett.*, 88:016403, Dec 2001.
- [91] Rudolf Zeller. Towards a linear-scaling algorithm for electronic structure calculations with the tight-binding Korringa-Kohn-Rostoker Green function method. *Journal of Physics: Condensed Matter*, 20(29):294215, 2008.
- [92] S. Lounis, Ph. Mavropoulos, P. H. Dederichs, and S. Blügel. Noncollinear Korringa-Kohn-Rostoker Green function method: Application to 3d nanostructures on Ni(001). *Phys. Rev. B*, 72:224437, Dec 2005.
- [93] F. G. Eich and E. K. U. Gross. Transverse spin-gradient functional for noncollinear spin-density-functional theory. *Phys. Rev. Lett.*, 111:156401, Oct 2013.
- [94] U von Barth and L Hedin. A local exchange-correlation potential for the spin polarized case. i. *Journal of Physics C: Solid State Physics*, 5(13):1629, 1972.
- [95] R. Zeller and P. H. Dederichs. Electronic structure of impurities in Cu, calculated self-consistently by Korringa-Kohn-Rostoker Green’s-function method. *Phys. Rev. Lett.*, 42:1713–1716, Jun 1979.
- [96] K. Sato, L. Bergqvist, J. Kudrnovský, P. H. Dederichs, O. Eriksson, I. Turek, B. Sanyal, G. Bouzerar, H. Katayama-Yoshida, V. A. Dinh, T. Fukushima, H. Kizaki, and R. Zeller. First-principles theory of dilute magnetic semiconductors. *Rev. Mod. Phys.*, 82:1633–1690, May 2010.

-
- [97] A.I. Liechtenstein, M.I. Katsnelson, V.P. Antropov, and V.A. Gubanov. Local spin density functional approach to the theory of exchange interactions in ferromagnetic metals and alloys. *Journal of Magnetism and Magnetic Materials*, 67(1):65 – 74, 1987.
- [98] S. Polesya, S. Mankovsky, D. Ködderitzsch, W. Bensch, and H. Ebert. Dzyaloshinskii–Moriya interactions and magnetic texture in Fe films deposited on transition-metal dichalcogenides. *physica status solidi (RRL) – Rapid Research Letters*, 10(3):218–221, 2016.
- [99] W. H. Butler, X.-G. Zhang, T. C. Schulthess, and J. M. MacLaren. Spin-dependent tunneling conductance of Fe|MgO|Fe sandwiches. *Phys. Rev. B*, 63:054416, Jan 2001.
- [100] S. Lowitzer, D. Ködderitzsch, and H. Ebert. Spin projection and spin current density within relativistic electronic-transport calculations. *Phys. Rev. B*, 82:140402, Oct 2010.
- [101] H. Ebert, S. Mankovsky, D. Ködderitzsch, and P. J. Kelly. Ab initio calculation of the Gilbert damping parameter via the linear response formalism. *Phys. Rev. Lett.*, 107:066603, Aug 2011.
- [102] A. Vernes, B. L. Györffy, and P. Weinberger. Spin currents, spin-transfer torque, and spin-Hall effects in relativistic quantum mechanics. *Phys. Rev. B*, 76:012408, Jul 2007.
- [103] H. Ebert and M. Battocletti. *Spin-orbit Induced Electric Field Gradients in Magnetic Solids*, pages 25–28. Springer Berlin Heidelberg, Berlin, Heidelberg, 2005.
- [104] Ding-sheng Wang, Ruqian Wu, and A. J. Freeman. State-tracking first-principles determination of magnetocrystalline anisotropy. *Phys. Rev. Lett.*, 70:869–872, Feb 1993.
- [105] Xindong Wang, Ruqian Wu, Ding-sheng Wang, and A. J. Freeman. Torque method for the theoretical determination of magnetocrystalline anisotropy. *Phys. Rev. B*, 54:61–64, Jul 1996.
- [106] S. V. Beiden, W. M. Temmerman, Z. Szotek, G. A. Gehring, G. M. Stocks, Yang Wang, D. M. C. Nicholson, W. A. Shelton, and H. Ebert. Real-space approach

- to the calculation of magnetocrystalline anisotropy in metals. *Phys. Rev. B*, 57:14247–14253, Jun 1998.
- [107] Markus Eisenbach, Balazs L. Györffy, G. Malcolm Stocks, and Balazs Újfalussy. Magnetic anisotropy of monoatomic iron chains embedded in copper. *Phys. Rev. B*, 65:144424, Mar 2002.
- [108] P. Gambardella, S. Rusponi, M. Veronese, S. S. Dhesi, C. Grazioli, A. Dallmeyer, I. Cabria, R. Zeller, P. H. Dederichs, K. Kern, C. Carbone, and H. Brune. Giant magnetic anisotropy of single cobalt atoms and nanoparticles. *Science*, 300(5622):1130–1133, 2003.
- [109] S Ikeda, K Miura, H Yamamoto, K Mizunuma, HD Gan, M Endo, SI Kanai, J Hayakawa, F Matsukura, and H Ohno. A perpendicular-anisotropy CoFeB–MgO magnetic tunnel junction. *Nature materials*, 9(9):721–724, 2010.
- [110] Jaivardhan Sinha, Masamitsu Hayashi, Andrew J. Kellock, Shunsuke Fukami, Michihiko Yamanouchi, Hideo Sato, Shoji Ikeda, Seiji Mitani, See hun Yang, Stuart S. P. Parkin, and Hideo Ohno. Enhanced interface perpendicular magnetic anisotropy in Ta|CoFeB|MgO using nitrogen doped Ta underlayers. *Applied Physics Letters*, 102(24):242405, 2013.
- [111] Piotr Błoński and Jürgen Hafner. Density-functional theory of the magnetic anisotropy of nanostructures: an assessment of different approximations. *Journal of Physics: Condensed Matter*, 21(42):426001, 2009.
- [112] O. Šipr, S. Bornemann, J. Minár, and H. Ebert. Magnetic anisotropy of Fe and Co adatoms and monolayers: Need for a proper treatment of the substrate. *Phys. Rev. B*, 82:174414, Nov 2010.
- [113] Jiong Zhao, Qingming Deng, Alicja Bachmatiuk, Gorantla Sandeep, Alexey Popov, Jürgen Eckert, and Mark H. Rümmeli. Free-standing single-atom-thick iron membranes suspended in graphene pores. *Science*, 343(6176):1228–1232, 2014.
- [114] H. X. Yang, M. Chshiev, B. Dieny, J. H. Lee, A. Manchon, and K. H. Shin. First-principles investigation of the very large perpendicular magnetic anisotropy at Fe|MgO and Co|MgO interfaces. *Phys. Rev. B*, 84:054401, Aug 2011.

-
- [115] Jia Zhang, Christian Franz, Michael Czerner, and Christian Heiliger. Perpendicular magnetic anisotropy in CoFe/MgO/CoFe magnetic tunnel junctions by first-principles calculations. *Phys. Rev. B*, 90:184409, Nov 2014.
- [116] Thomas Bose, Ramon Cuadrado, Richard F L Evans, Roman V Chepulskii, Dmytro Apalkov, and Roy W Chantrell. First-principles study of the Fe|MgO(0 0 1) interface: magnetic anisotropy. *Journal of Physics: Condensed Matter*, 28(15):156003, 2016.